

UNIVERSITY OF OKLAHOMA
GRADUATE COLLEGE

MULTISCALE NATURAL FRACTURE CHARACTERIZATION WORKFLOW FOR
UNCONVENTIONAL SHALE, WOODFORD AND BARNETT SHALES AS EXAMPLES

A DISSERTATION
SUBMITTED TO THE GRADUATE FACULTY
in partial fulfillment of the requirements for the
Degree of
DOCTOR OF PHILOSOPHY

By
JING ZHANG
Norman, Oklahoma
2019

MULTISCALE NATURAL FRACTURE CHARACTERIZATION WORKFLOW FOR
UNCONVENTIONAL SHALE, WOODFORD AND BARNETT SHALES AS EXAMPLES

A DISSERTATION APPROVED FOR THE
SCHOOL OF GEOLOGY AND GEOPHYSICS

BY THE COMMITTEE CONSISTING OF

Dr. Roger M. Slatt, Chair

Dr. Ahmad Ghassemi

Dr. Kurt Marfurt

Dr. Shankar Mitra

Dr. Zeev Reches

Dedicated to dear Dr. Statt

Acknowledgements

Last five years of my Master and Ph.D. study at OU, I received a tremendous amount of help and encouragements which make me grow into a better person and accomplished the work I love. I wish to acknowledge those people deeply with my sincere gratitude.

I would like to send my special gratitude to my advisor Dr. Roger Slatt. During the past five years I have gained my professional experience and academic achievement because of his generous help. His inspiring ideas and professional guidance supported me to reach academic excellence; his caring encouragement and thoughtful advice carried me throughout this time.

Unique and sincere appreciation also included in here for my amazing committee members who supported me for years: Dr. Ahmad Ghassemi, Dr. Kurt Marfurt, Dr. Shankar Mitra, and Dr. Zeev Reches. This great team of professors broadened my background and strengthened my understanding on my research. Your consistent support and patience always encourage me to pursue higher accomplishments during my Ph.D. study.

Here I also wish to express my deep gratitude to my family, my mom Xiaoduo Wang and dad Yumin Zhang, grandparents who played a strong backup in my life, I wouldn't be able to make it without all your love, support and encouragement.

Earnest appreciation to all the friends and colleagues I met, worked and spend joyful time with at OU. Special thanks to my dear friends Andreina Liborius, Lennon Infante, Carolina Maryoga, Ifunanya (Naya) Ekwunife, Emilio Torres, David Duarte, Francis Oyebanji, Jianjun Li, Jie Qi, Fuge Zou, Delcio Teixeira, Nancy Leonard, and Sofia Caylor. I feel so lucky to have you all as my friends in my life.

Table of Contents

ACKNOWLEDGEMENTS	V
LIST OF TABLES	IX
LIST OF FIGURES	X
CHAPTER I	1
INTRODUCTION.....	1
CHAPTER II	3
INTRODUCTION OF NATURAL FRACTURE CHARACTERIZATION METHODS FOR UNCONVENTIONAL SHALES	3
CHAPTER II REFERENCES	11
CHAPTER III.....	17
OUTCROP AND CORE BASED MULTISCALE BED BOUNDED NATURAL FRACTURE CHARACTERIZATION AND FRACTURE DENSITY CONTROLLING FACTOR STATISTICAL ANALYSIS: WOODFORD EXAMPLE.....	17
ABSTRACT	17
INTRODUCTION.....	18
<i>INVESTIGATION TARGETS</i>	19
METHODOLOGY	25
<i>FRACTURE CHARACTERIZATION</i>	25
<i>DATA PREPARATION</i>	29
<i>DATA ANALYSIS</i>	30
RESULTS.....	32
DISCUSSION AND CONCLUSIONS	39
CHAPTER III REFERENCES	40
CHAPTER IV	46

QUANTITATIVE ANALYSIS OF LAYERING EFFECT ON FRACTURE OCCURRENCE AND DISTRIBUTION PATTERN.....	46
ABSTRACT	46
INTRODUCTION.....	47
METHODOLOGY	50
<i>MATERIAL DESCRIPTION</i>	50
<i>EXPERIMENTAL SETUP</i>	52
<i>OBSERVATION METHODS</i>	54
RESULTS.....	57
<i>FRACTURE DEVELOPMENT</i>	57
<i>FRACTURE INTENSITY TRENDS</i>	62
<i>LAYERING ANISOTROPY INDEX</i>	68
DISCUSSION AND CONCLUSIONS	68
CHAPTER IV REFERENCES.....	70
CHAPTER V.....	77
AZIMUTHAL SEISMIC ANISOTROPY ANALYSIS APPLIED TO NATURALLY FRACTURED UNCONVENTIONAL RESERVOIRS: BARNETT SHALE EXAMPLE.....	77
ABSTRACT	77
INTRODUCTION.....	78
<i>GEOLOGIC BACKGROUND</i>	80
<i>BASIN STRUCTURAL SETTINGS AND FRACTURES</i>	82
<i>REGIONAL STRUCTURAL ANALYSIS</i>	83
METHODOLOGY	85
<i>ATTRIBUTES FOR ANISOTROPY ANALYSIS</i>	90
RESULTS.....	95
<i>AMPLITUDE VARIATION WITH AZIMUTH</i>	95
<i>ENVELOPE ATTRIBUTE ANISOTROPY ANALYSIS</i>	98

<i>SPECTRAL PEAK FREQUENCY ATTRIBUTE ANISOTROPY ANALYSIS</i>	99
<i>PRESTACK P-IMPEDANCE ANISOTROPY ANALYSIS</i>	100
<i>RESULT VERIFICATION WITH PRODUCTION MAP</i>	103
DISCUSSION.....	104
CONCLUSIONS	105
CHAPTER V REFERENCES	106
CHAPTER VI	114
DISCUSSION AND SUMMARY OF CHAPTERS	114
APPENDIX A	118

List of Tables

Table 1: the Pearson Correlation coefficient matrix of controlling factors and 2D fracture area density for both I-35 outcrop and Hall 2B core. High positive correlation between the fracture area density and bed frequency is observed from both. There is also high positive correlation between hard bed ratio and hardness since they both represent rock mechanical properties.

..... 32

Table 2: Factor loading summary table for both outcrop and core. The F1 factor loading is higher on the outcrop case than on the core case..... 36

Table 3: Strike measurement on Fault A and B from the Base Barnett strata slice of coherence and most positive curvature attributes. 85

List of Figures

Figure 2.1: Sample failure in compression regime, note a shear failure plane formed with an angle β between the fault normal σ_n and maximum compressive stress σ_1 (Zoback, 2010).

..... 3

Figure 2.2: Series of compressional triaxial strength tests delineate a Mohr failure envelope, which indicates confining pressure's relationship with rock strength. The unconfined compressive strength (UCS) when confining pressure is 0 is highlighted in figure as UCS (C_0) (Zoback, 2010).

..... 4

Figure 2.3: Schematic diagram of various types of fractures with respect to the different stress regimes. Mode I is when the deformation is shallow where the vertical stress is not significant compared to the horizontal stresses; b is the same mode as a normal fault when the maximum horizontal stress is less than the vertical stress and parallel to the fracture plane; c is the same mode as strike and slip fault regime and conjugate sets form laterally instead of vertically; d is the same mode as a reverse fault and conjugate sets are expected to dip about 60° and the strike parallel to the maximum horizontal stress (Zoback, 2010).

..... 5

Figure 2.4: Fracture density definition chart, the descriptive term of fracture density, intensity, and porosity are summarized in one, two and three dimensional spaces. Modified from Dershowitz and Herda (1992).

..... 9

Figure 3.1: Location and overview of the I-35 Outcrop. (a) Oklahoma geological provinces and cross-section A-A' in red line across the Ardmore Basin and Arbuckle Uplift [Modified from Cardott (2012), originally from Campbell and Northcutt (1998)]. (b) closer display of the I-35 outcrop location (Becerra et al., 2018). (c) tectonic cross section highlighted in (a) as A-A'; approximate location of the study area is highlighted as a red star, the Woodford Shale (the gray

strata in cross section) is dipping towards the southwest into the Ardmore Basin [Modified from Galvis-Portilla et al. (2016), originally from Ham and Amsden (1969)]. (d) Aerial photograph of the I35 outcrop showing the exposure of the Upper and Lower Woodford members, the Middle Woodford member was eroded into a valley due to its high clay content. Fracture characterization is mainly located in the section highlighted with the orange box which composed of 80 feet of the Upper Woodford member. (e) The Upper Woodford member photo mosaic has beds striking N65°W and dipping 48° towards the southwest. The outcrop gamma ray profile is projected on the corresponding measurement spots [modified from Becerra (2017)].

..... 20

Figure 3.2: Interbedded chert and siliceous organic-clay shale on the I-35 outcrop. Red lines outline the siliceous and clay/organic rich shale that is weathered to light gray on the outcrop; green lines outline the chert beds that are massive and brittle. Note that most of the fractures are bed-bounded in the cherty beds but not extend to the siliceous shale, and density varies on these two different facies (Becerra, 2017). 22

Figure 3.3: (a) the Woodford Shale structural and thickness map in western Oklahoma. The cross-section A-A' as outlined in the red dashed line is close to the Hall 2B core highlighted as a red dot. I-35 outcrop location is shown as the red star about 60 miles southeast of the core location [modified from EIA (2011)]. (b) cross-section A-A' shows Mississippian, Devonian, and Silurian strata which are represented by the “MDS” section in light purple color. The Woodford Shale section was uplifted by a series of reverse faults during the Wichita uplift and formed a larger burial depth contrast than the neighboring Woodford Shale section in the Anadarko Basin [Modified from Johnson and Luza (2008)]. 24

Figure 3.4: Hall 2B core beds are mainly steeply dipping with well-developed bed bounded fractures in the brittle cherty beds but not in the siliceous beds. Cherty beds are usually a light gray color and siliceous shale beds are dark brown. The bed thickness is thinner than the beds at the I-35 outcrop. (a) the lower part of the core is dominated by sealed fractures which are subvertical to vertical to the beds, the fractures are sealed by carbonate and siliceous cement. (b) opened dissolution fractures in the upper part of the core, the fractures are subvertical to vertical to the beds. 25

Figure 3.5: Demonstration of fracture density 2D measurement method for both core and outcrop. Scanning window is highlighted in black lines, bed bounded fractures in ductile clay-rich (siliceous shale) beds are outlined by red lines. Bed-bounded fractures in the brittle cherty beds are highlighted by green lines. (a) the measurement window in the Hall 2B core is selected where the fractures and bed boundaries are clear enough to identify. The size of the parallelogram shaped measurement window is not exactly the same, but the true thickness is controlled close to 3 inches to keep a general area consistency. (b) the outcrop measurement window keeps a 1 square foot area in the rectangular shape. Fractures within each window are counted. 27

Figure 3.6: Schematic diagram of hardness measurement by the Equotip Picolo 2 hardness tester. The internal structure of the impact body is spring mounted with a 3mm diameter ball in the base. The hardness value is the ratio between the rebound and impact velocities multiplied by 1000 (Becerra, 2017). 28

Figure 3.7: The data analysis flowchart and expected outcome from each step. The first step is to have a preview of variable correlation by calculating the Pearson correlation coefficient. The second step is to conduct the Principal Component Analysis to qualify the relationship between

variables and calculate the factor loading. The third step is to construct a Partial Least Squares Regression model and obtain a quantified relationship between hardness, hard bed ratio, bed frequency and area fracture density then ultimately identify the contribution of variation from each independent variable. 31

Figure 3.8: The correlation chart between variables, the fracture area density is shown in a logarithm scale to reveal the differences between outcrop and core fracture density caused by bed thickness magnitude difference. (a) Interval hardness vs fracture area density shows poor correlation for both outcrop and core. (b) Hard bed ratio and fracture area density are poorly correlated for both investigation targets. (c) Bed frequency has a very good correlation with fracture area density with a projectable trend from the outcrop scale to the core scale, the core scale correlation with fracture density is lower than the coefficient in the outcrop mainly due to the change in bed thickness along the lateral measuring section. (d) Hardness and hard bed ratio are well correlated with a projectable trend from the outcrop scale to the core scale.... 34

Figure 3.9: Factor variability and eigenvalue diagram for both outcrop and core cases. The column chart uses the primary vertical axis on the left representing the eigenvalue of each factor, the F1 has the highest eigenvalue which means it represents higher variability than the other factors and outcrop has a higher value than the core. The line chart uses the secondary vertical axis on the right to represent the cumulative variability for each factor. Until variable factor 2, more than 80 % of the variability can be represented, thus factors 1 and 2 together are sufficient to present the dataset as new variables. 35

Figure 3.10: Variable circle for the I-35 outcrop (left) and Hall 2B core (right). The vectors of variables are all close to the edge of circles meaning that F1 and F2 space is sufficient to represent most variability in the original dataset. Hardness and hard bed ratio are tightly paired,

and fracture area densities are tightly paired with bed frequency which means they are highly positively correlated. But two pairs are almost orthogonal which indicates that they are less well correlated. All the variables are on the positive axis of F1 which means the F1 factor is positively correlated to all the variables. Hardness and hard bed ratio are projected to the positive axis of F2 which means they are positively correlated to F2. The same relationship is negative with bed frequency and fracture area density..... 36

Figure 3.11: The PLS regression model result for both core (left) and outcrop (right). The horizontal axis is the modeled result compared with the actual measurement from the sample as the vertical axis. The regression coefficient is higher in the outcrop model due to higher correlation between controlling factors and more data points available. 38

Figure 3.12: The VIP value comparison chart for the outcrop and core. VIP value is highest in bed frequency for both cases than the other two independent variables (hardness and hard bed ratio). This indicates that bed frequency plays a key role in controlling frac fracture density in both surface and subsurface conditions. Hard bed ratio’s contribution is about the same for both cases, but the hardness contribution is less in the core case, which indicates hardness plays a less important role under the relatively high confining pressure..... 38

Figure 4.1: Schematic diagram of anisotropy types of shale reservoirs..... 48

Figure 4.2: Damage behavior stages in stress and strain profile of brittle rock (Cai et al., 2004). 50

Figure 4.3: Dimension settings for different layer models..... 53

Figure 4.4: Uniaxial compression test applied to a 1cm layer clay model. The model was compressed with slowly under uniaxial stress (2 cm axial strain). 54

Figure 4.5: Demonstration model for fracture forming under uniaxial compressional stress and lateral radial strain. The left model indicates interbeds with high stiffness layers in gray and low stiffness layers in yellow. Under unconfined conditions the strain is not just axial but also radial. The right diagram illustrates shear fractures developed under compressional regime in the “brittle” layers which do not extend into the “ductile” layers. Aperture of the fracture is mainly caused by radial strain. 55

Figure 4.6: (a) The 0.5 cm thickness layer model after deformation. (b) Black lines indicate layers boundaries. Red lines indicate fractures. 56

Figure 4.7: Eight Fracture types observed from the layer cake model experiment. (a) vertical fracture, (b) simple shear fracture, (c) simple half conjugate type a, (d) simple half conjugate type b, (e) simple conjugate, (f) complex conjugate, (g) En Echelon fractures, (h) opened fracture, and (i) compressed opened fracture. 58

Figure 4.8: Fracture pattern deformation stages in the layering model. Stage 1 is the initiation of deformation with pinpointed tearing fractures. Stage 2 is the growing stage of the shear fractures that tries to connect the top and bottom initiation point in the same brittle layer. Stage 3 forms a connected pattern of shear or conjugate set of fracture planes within each brittle layers. Stage 4 starts to form the deformation initiation points in the ductile layers from the top and bottom part of the shear planes. Stage 5 starts to form En Echelon failures in the ductile layers and those failures get interconnected in stage 6 which also connect the shear fracture plane with same dipping trends in the neighboring brittle layers. Once all the deformation pattern formed, the aperture starts to increase in the previous planes. Selected observations from the actual model for each stage are listed below. 61

Figure 4.9: Layer clay model with 1cm thickness, the measured areas are outlined by red lines and the fractures are delineated by red thin lines. 64

Figure 4.10: Layer clay model with 0.75cm thickness, the measured areas are outlined by red lines and the fractures are delineated by red thin lines..... 65

Figure 4.11: Layer clay model with 0.5cm thickness, the measured areas are outlined by red lines and the fractures are delineated by red thin lines. 66

Figure 4.12: Fracture intensity's relationship with layer thickness. There is an increasing trend in the shear deformation stage which means the intensity increases with layer frequency. However, after the layer thickness reaches a certain lower limit, the aperture deformation stage starts to dominate and shows a decrease in fracture intensity but increase in fracture aperture.. 67

Figure 5.1: Seismic wave amplitude and velocity attenuation when penetrates perpendicular to the fracture strike direction..... 80

Figure 5.2: Major structural features of the Fort Worth Basin and production type distribution (Pollastro et al., 2007). The location of the case study area is highlighted with the blue dot. 81

Figure 5.3: Stress map of Texas showing the maximum horizontal stress orientation (Lund Snee and Zoback, 2016). The study area is highlighted in the blue circle, the FWB represents the Fort Worth Basin and indicates that the current day maximum horizontal stress is trending northeast-southwest, the colors indicate that the study area locates within a strike slip fault and normal fault transition regime..... 83

Figure 5.4: Strata slice (Base Barnett) through (a) coherence, and (b) most positive and negative curvature co-render maps. Two major normal faults (Fault A, Fault B) are delineated by the

orange dashed lines, both of which are subparallel to the Mineral Wells Fault (not included in the survey). 84

Figure 5.5: The regional stress field interpretation is based on observed structures and the regional fault. The maximum horizontal stress follows orientation parallel to the strike of Faults A and B. The local stress field and structure cannot be simply represented by the regional stress field. 86

Figure 5.6: Eight different azimuthal bins covering the full azimuth range with 22.5° increment using the method proposed by (Perez and Marfurt, 2007) 87

Figure 5.7: Workflow for azimuthal anisotropy analysis and interpretation. Data should be preprocessed and then the target horizons are interpreted manually for each azimuthal volume in order to compensate for the velocity anisotropy effect. Extracted attributes along key horizons were input for anisotropy analysis respectively. The output includes three key parameters of anisotropy: intensity, azimuth and confidence. 88

Figure 5.8: Four key formation top horizons picked in the seismic survey. (a) Inline view showing the thickness relationship of the Upper Barnett, Lower Barnett and Forestburg Lime. (b) Four interpreted horizons in 3D view. For each azimuthal volume, the horizons were picked separately. 88

Figure 5.9: azimuthal seismic volumes comparison from the cross section obtained from the northwest part of the study area. The color code represents magnitude of amplitude. Note that amplitude varies by azimuthal volume and the arrival time of four key horizons that are highlighted in green are different after manually interpreting the horizons. The interpretation uses 2D seed picking for each volume and QC manually afterward to avoid any manually picking error. 89

Figure 5.10: Seismic impedance calculation and well tie procedure. Because of anisotropy and acquisition parameters, the effective seismic wavelet for each azimuthal sector is slightly different. We therefore generated well ties for each volume. Note that the Forestburg Lime can be easily identified from the low gamma ray log as well as the density contrast which leads to an increase in impedance and velocity within the Forestburg. The seismic section is the well intersected inline and the gray filled trace is the specific intersected trace. The diagram shows the result after well tie and matched wells with velocity profile and interpreted seismic horizons.

..... 93

Figure 5.11: P wave impedance results from model and log cross plot shows a reliable correlation of the calculation result on each azimuth, confirming the reliability for further anisotropy calculations. 94

Figure 5.12: Azimuth 1 derived vertical slice through P-wave impedance with phantom horizons for the top upper Barnett and top lower Barnett that are highlighted on the left side of the impedance volume with the white arrows, regular horizons that are highlighted on the right with the black arrows. Note that the impedance value at the regular horizons have sharp changes and cannot be used to represent the interval property. 95

Figure 5.13: Co-rendered map of coherence attribute and anisotropy intensity, the coherence map located in the Base Barnett strata slice and set for transparent for the low coherence value area. The anisotropy intensity map is generated from the Top Barnett (TB) amplitude anisotropy analysis. Four high anisotropy intensity zones are identified as A, B, C, and D. High intensity zones correspond to low coherence areas (lighter transparent area) which indicates the discontinuity is below the resolution of a typical seismic attribute. 96

Figure 5.14: Amplitude anisotropy analysis results along the four key horizons shows intensity, azimuth and confidence of anisotropy. The anisotropy intensity decreases geologically downward, and the Upper Barnett generally has higher intensity at all four anisotropy zones than the Lower Barnett Shale. The azimuth of Zones A and D (location indicated in Figure 13) is generally consistent with a northeast-southwest trend. Zones B and C have slightly different azimuths, but locations are consistent throughout the formation. 97

Figure 5.15: Envelope attribute anisotropy analysis result. The intensity result is similar to the amplitude result and azimuth shows a more consistent northeast-southwest trend for Zones A, B and D; zone C has a different north-south trending azimuth. Confidence at high intensity zones is high, making the result reliable for further interpretation. 99

Figure 5.16: Spectral peak frequency attribute anisotropy analysis result, location of the high anisotropy zone is the same with previous results on the Base Barnett surface. The azimuth of the high anisotropy zones shows an orthogonal relationship with amplitude-based attributes. 100

Figure 5.17: Prestack P impedance anisotropy analysis result from two phantom horizons. Zone A, B and C are obvious to locate, but zone D is hard to locate on both surfaces, which generally have lower intensity of anisotropy than the Upper Barnett Shale. 101

Figure 5.18: Attribute anisotropy intensity map of the Base Upper Barnett co-rendered with a regional gas production map. Note that the production distribution has an inverse relationship with high anisotropy distribution..... 104

Figure 6.1: Comprehensive Natural Fracture Characterization Workflow for the unconventional shale reservoir..... 117

CHAPTER I

INTRODUCTION

This research presents an integrated methodology and workflow to characterize, interpret and predict natural fracture occurrence in different scales for unconventional shales using the Devonian-Mississippian Woodford and Barnett Shales in the midcontinent, United States as examples. The research projects are presented separately in the five chapters exhibiting different scales and objectives.

Chapter II is an introduction that summarizes basic knowledge, current understanding, general methodologies of characterization, and existing theories based on previous studies of natural fractures in unconventional shale reservoirs. This chapter will discuss conventional workflows, observation methods, and the advantages and disadvantages of alternative fracture characterization methods. Also review geomechanical analysis of unconventional reservoirs at different fracture scales.

Chapter III begins with a characterization of natural fractures seen in drilling core and outcrop of the Woodford Shale in southern Oklahoma. The core, located in a fault block in Caddo County, Oklahoma, falls within the Southern Oklahoma Aulacogen (SOA) depocenter near the northern rim of the Wichita Uplift. The outcrop is located on the northern rim of the Ardmore Basin and southern flank of the Arbuckle anticline in Carter County with an exposure of 81 feet of the Upper Woodford member and 10 feet of the Lower Woodford member. In addition to proximity, the core and outcrop Woodford Shale locations underwent similar intense tectonic deformation processes during development of the Southern Oklahoma Aulacogen (SOA) and such that the observed are similar and well developed. After characterizing hardness, bed thickness, and fracture density, I examine that I correlate to fracture occurrence/density. These analysis well show

that the layering effect is the most dominant controlling factor of natural fracture density in these rocks.

Chapter IV is an extended study to quantify further how the layering effect can affect natural fracture density. A lab-based clay cake experiment was designed to mimic the brittle-ductile couplets feature, common to marine shales such as the Woodford Shale. The uniaxial compressional test was applied to the cylindrical shape mud layer model to create compressional fractures and simulate small-scale deformational scenarios in nature. Different groups of layer numbers with various thickness combinations were compared and quantified to explain how interbeds can control the distribution and density of natural fractures.

Chapter V examines the subject to reservoir scale fracture characterization using 3D seismic data. Centimeter-scale fractures characterized in the previous chapters might not be able to provide a significant contribution to the full field production flow. Thus, when considering larger-scale features, seismic data is more representative, consistent and reliable than core and logs with a limited area of coverage. Chapter V uses the Barnett Shale in North Texas, Fort Worth Basin as an example and presents an azimuthal anisotropy analysis on a wide azimuth, time migrated 3D seismic survey to correlate seismic anisotropy with natural fracture distribution. The new interpretation workflow is proposed to integrate and compare the different amplitude and velocity related seismic attributes anisotropy effect and how the interpretation can be used as an indicator for fracture network visualization.

Chapter VI is a summary chapter of the previous chapters. The integrated results are tied to reveal a bigger picture of natural fracture characterization for unconventional shales on different scales. A standardized characterization workflow is summarized to incorporate fracture characterization methods at all scales, which can be used for other shales.

CHAPTER II

INTRODUCTION OF NATURAL FRACTURE CHARACTERIZATION

METHODS FOR UNCONVENTIONAL SHALE

Fracture, as a type of material failure, occurs on a rock when the stress on the rock exceeds the rock strength, which makes the rock lose cohesion along the failure plane. (Brace et al., 1966; Nelson, 2001; Park, 2013). Failure of rock in a compressional regime is the most common case and presented here as an example. The compressional deformation process was initiated with microscopic failures as tensile cracks and frictional sliding on grain boundaries and then coalescence of these microscopic failures to form a shear failure plane as a catastrophic event in a brittle rock (Figure 2.1) (Lockner et al., 1991; Zoback, 2010). Mohr circle is a classic way to illustrate how the failure occurs when stress overcomes the rock Mohr-Coulomb failure envelope. This envelope allows evaluation of shear stress and effective normal stress on fault/fractures that form under effective principal stresses σ_1 and σ_3 (Figure 2.2). The rock strength varies based on mineral cohesion, pore pressure, confining pressure, internal anisotropy, and temperature (Jaeger et al., 2009; Zoback, 2010)

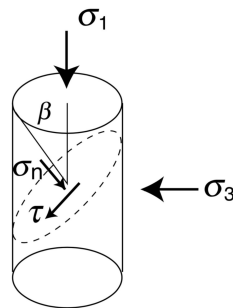


Figure 2.1: Sample failure in compression regime, note a shear failure plane formed with an angle β between the fault normal σ_n and maximum compressive stress σ_1 (Zoback, 2010).

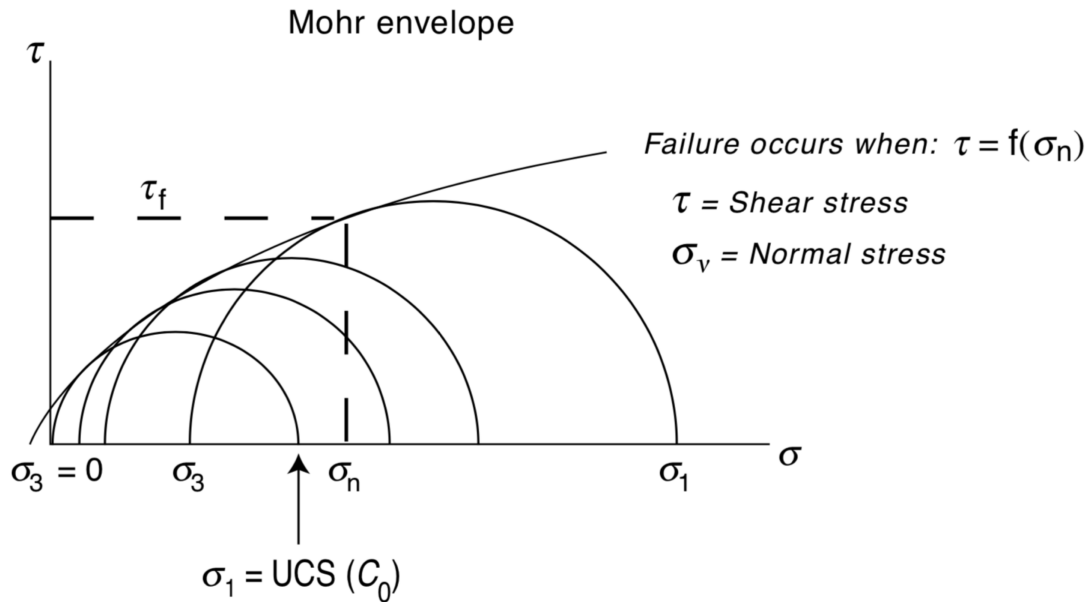


Figure 2.2: Series of compressional triaxial strength tests delineate a Mohr failure envelope, which indicates confining pressure's relationship with rock strength. The unconfined compressive strength (UCS) when confining pressure is 0 is highlighted in figure as UCS (C_0) (Zoback, 2010).

Natural fractures can be classified based on their stress field at failure or triggering forces. According to Handin and Hager Jr (1957) and Stearns and Friedman (1972), fractures can be classified by laboratory experiment and failure mechanism (generic classification) as three types: (1) Shear fractures (2) Extension fractures (3) Tensile fractures (Nelson, 2001). Figure 2.3 shows these types of fractures and their associated stress regimes. Shear fractures form at an acute angle to the maximum compressive principal stress σ_1 and obtuse angle to the minimum compressive stress σ_3 . Shear fracture is the most common case when principle stresses are all compressive. The angle of the fracture plane with stresses depends on the properties of the material and absolute and relative magnitude of stresses. Extensional fractures usually form associated with shear fractures in the lab and displacement moves perpendicular to the fracture plane. The difference between a tension fracture and an extension fracture is that at least one of the effective principal stresses must

be tensile for the tension fracture, and rock has much lower fracture strength in the tension regime (Nelson, 2001).

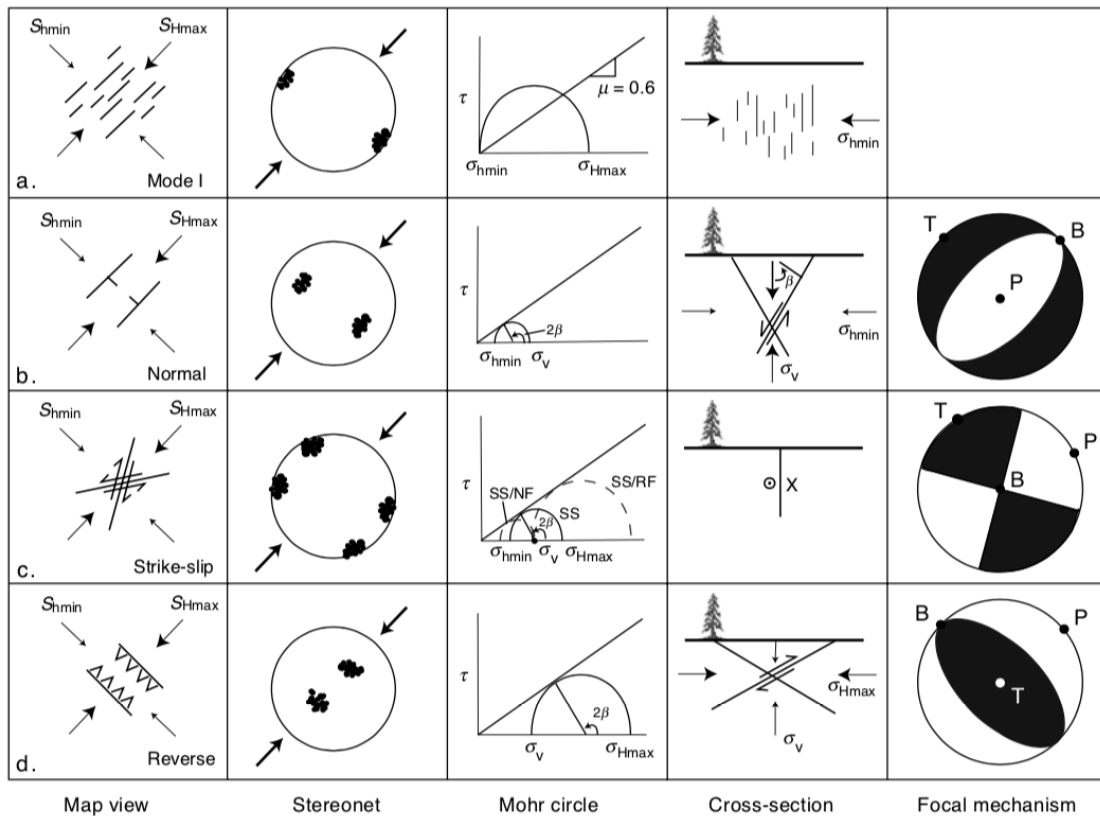


Figure 2.3: Schematic diagram of various types of fractures with respect to the different stress regimes. Mode I is when the deformation is shallow where the vertical stress is not significant compared to the horizontal stresses; b is the same mode as a normal fault when the maximum horizontal stress is less than the vertical stress and parallel to the fracture plane; c is the same mode as strike and slip fault regime and conjugate sets form laterally instead of vertically; d is the same mode as a reverse fault and conjugate sets are expected to dip about 60° and the strike parallel to the maximum horizontal stress (Zoback, 2010).

Stearns and Friedman (1972) proposed a geologic classification of natural fractures in multiple scales. They can be categorized into (1) tectonic fractures (due to surface forces), (2) regional fractures (due to surface or body forces), (3) contractional fractures (due to body forces), and (4) surface-related fractures (due to body forces). Tectonic fractures can be observed at all scales due to a consistent and nonnegligible stress field that is related to local tectonic events such

as a fault related fracture system (Stearns, 1964; Skehan, 1968; Stearns, 1968; Friedman and Logan, 1970; Stearns and Friedman, 1972; Ghosh, 2017; Milad et al., 2018) and fold related fracture system (Stearns, 1964, 1968; Cosgrove and Ameen, 1999; Bergbauer and Pollard, 2004). Regional fractures are developed over large areas by earth crustal stresses. Compared to tectonic fractures, regional fractures more likely occur in a consistent and simple geometry, with large spacing and crosscutting local structures which are also called “systematic joints” (Price, 1959; Hodgson, 1961) or “regional joints” (Babcock, 1973; Engelder, 1982). They commonly develop in orthogonal sets which implies a loading and unloading history of the rock (Price, 1959). Contractional fractures are a collection of tension or extension fractures as a result of desiccation, syneresis, thermal gradients and mineral phase changes (Peacock and Sanderson, 1995; Nelson, 2001). Surface related fractures are the fractures formed during unloading, free surface creation, and weathering. They develop under body forces and commonly are observed in quarries and drilling cores with a dish shape or cusp shape; these fractures are typically irregular in shale (Price, 1966; Nelson, 2001)

Natural fracture occurrence in unconventional shale reservoirs has received considerable attention because of its potential impact on reservoir quality characterization and shows a significant impact on reservoir fluid flow either positively or negatively, interacts with hydraulic fractures and generates reservoir anisotropy. Numerous studies have been conducted based on outcrop, core and subsurface data to understand the origin, preferential distribution pattern and impact factors on fracture occurrence in reservoir rocks (Nelson, 2001; Curtis, 2002; Helbig and Thomsen, 2005; Gale et al., 2007; Olson and Taleghani, 2009; Gale and Holder, 2010; Cho et al., 2013)

Due to the limited access to subsurface data, outcrop field fracture characterization is commonly used as an analog (Hennings et al., 2000; Nelson, 2001; Olson and Taleghani, 2009;

Milad et al., 2018). Compared to outcrop analogue characterization, fractures seen in drilling core or downhole image provide more direct ways to quantify fractures under reservoir conditions. These observations method provide only a local, 1D knowledge of the subsurface which may be difficult to extrapolate to 3D (Narr and Lerche, 1984; Lorenz and Hill, 1992; Narr, 1996; Nelson, 2001; Fernández-Ibáñez et al., 2018).

A more promising workflow for fracture analysis on a larger scale is to tie the relatively qualitative but dense 3D seismic response to the more quantitative sparse well control. Seismic fracture characterization can be used to predict both natural fractures and to map the induced hydraulic fractures (Tsvankin and Grechka, 2011; Liu, 2013). However, seismic fracture characterization with a wavelength of about 50 meters has limited resolution to show fracture spacing on the order of less than 10 meters for the most common surveys. Even though there are indications of scattering form of fractured zones, details on the orientation and density of the fracture system are still hard to verify (Liu, 2013). Neves et al. (2004), Chopra and Marfurt (2007) and Guo et al. (2010) found correlations between fracture distribution and seismic attributes such as coherence and curvature. Outcrop analysis and finite element models show a good correlation of fractures to the proximity of faults and the curvature of folds, which in turn can be mapped by seismic attributes such as coherence and curvature (Buseti et al., 2012). The presence of such fractures is “inferred” using a deformation model. In contrast, AVAz provides a direct measure of the presence of natural fractures and stress direction (Liu, 2013).

Natural fractures’ origin and characteristics need to be carefully studied ahead of reservoir development. As summarized above, there are various techniques available to qualify and quantify natural fractures on different scales and objects such as outcrop, drilling core, subsurface image logs and even seismic. For qualification purposes, fracture shape, filling, orientation and its

relationship to the regional stress field need to be understood to decipher the deformation history and mechanism. For quantitative purposes, fracture length, and fracture density are the most important indicators of its contribution to reservoir complexity and fluid flow (Nelson, 2001; Gale et al., 2014).

There are multiple methods to quantify fracture density in 1D, 2D or even 3D. In the case of roadcut outcrops or drilling core fracture characterization, fractures are most likely exposed on a 2D surface. Thus, 1D scanline and 2D area characterization are commonly used to count either the number or accumulated length of fractures in the selected area (Narr and Lerche, 1984; Mauldon and Dershowitz, 2000; Nelson, 2001; Babadagli, 2002; Ortega et al., 2006; Sagy and Reches, 2006). Fracture density, a parameter used to describe the intensity of deformation, has various ways to represent and describe the fractures at different scales and objects. According to Dershowitz and Herda (1992), a class of fracture density measured in one, two and three dimensions is defined and can be used to represent fractures for different purposes of characterization. These definitions are illustrated in Figure 2.4. The 1D scanline method has been widely applied on vertical/sub-vertical fracture quantification and revealed a general correlation between fracture density and single bed thickness on various types of the reservoirs (Ladeira and Price, 1981; Gross et al., 1995; Nelson, 2001; Wang and Gale, 2009). However, for a larger scale characterization especially when the reservoir is highly interbedded, it becomes challenging and unrealistic to apply the relationship from one single bed to an interbedded interval, particularly from core.

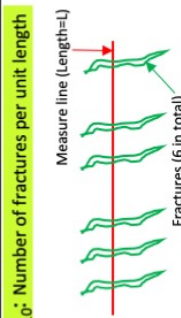
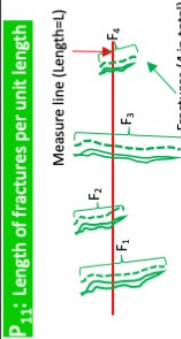
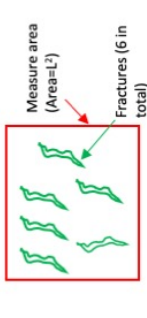
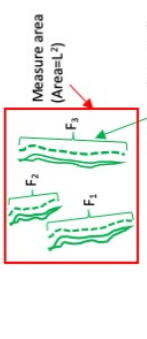
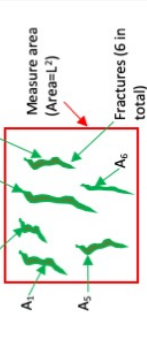
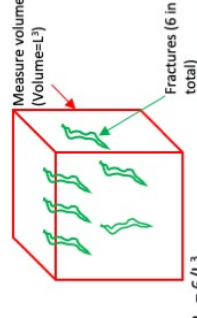

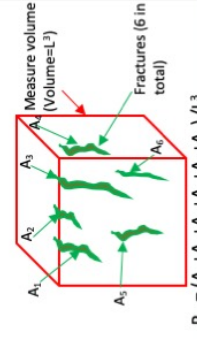
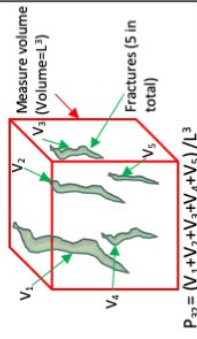
Dimension of Sample		Dimension of Measurement			Measurement type		
		0	1	2		3	
1	2	<p>P₁₀: Number of fractures per unit length</p>  <p>$P_{10} = 6/L$</p>	<p>P₁₁: Length of fractures per unit length</p>  <p>$P_{10} = (F_1 + F_2 + F_3 + F_4) / L$</p>	<p>P₂₀: Number of fractures per unit area</p>  <p>$P_{20} = 6/L^2$</p>	<p>P₂₁: Length of fractures per unit area</p>  <p>$P_{21} = (F_1 + F_2 + F_3) / L^2$</p>	<p>P₂₂: Area of fractures per unit area</p>  <p>$P_{22} = (A_1 + A_2 + A_3 + A_4 + A_5 + A_6) / L^2$</p>	Linear Measure
		<p>P₃₀: Number of fractures per unit volume</p>  <p>$P_{30} = 6/L^3$</p>	<p>P₃₁: Volume of fractures per unit volume</p>  <p>$P_{32} = (V_1 + V_2 + V_3 + V_4 + V_5) / L^3$</p>	<p>P₃₂: Area of fractures per unit volume</p>  <p>$P_{32} = (A_1 + A_2 + A_3 + A_4 + A_5 + A_6) / L^3$</p>	<p>P₃₃: Volume of fractures per unit volume</p>  <p>$P_{32} = (V_1 + V_2 + V_3 + V_4 + V_5) / L^3$</p>	Volumetric Measure	
		Nomenclature		Fracture Density	Fracture Intensity	Fracture Porosity	

Figure 2.4: Fracture density definition chart, the descriptive term of fracture density, intensity, and porosity are summarized in one, two and three dimensional spaces. Modified from Dershowitz and Herda (1992).

The occurrence and density of fractures are controlled by many factors, but can be generally summarized into two categories: the mechanical properties of the rock itself and the paleo stress field when the deformation occurred. The mechanical properties of rocks are a combined result of rock composition, grain size and fabric, porosity, pore structure, pore fluid, and bed thickness (Hugman III and Friedman, 1979; Sinclair, 1980; Gross et al., 1995; Nelson, 2001; Chang et al., 2006; Erguler and Ulusay, 2009; Aoudia et al., 2010; Török and Vásárhelyi, 2010; Sone and Zoback, 2013). For shale reservoirs distinguished in small grain size, low porosity and permeability, rock composition stands out as a dominant factor of the rock strength. Wang and Gale (2009) introduced the brittleness index equation of shale based on mineralogy and total organic matter (TOC) weight percentage. The higher the brittle mineral (quartz and dolomite) weight percentages are, the higher the brittleness of shales, which could lead to higher fracture density under the same stress field. Bed thickness are commonly accepted to have a reverse relationship with fracture density (Ladeira and Price, 1981; Narr and Suppe, 1991; Gross et al., 1995; Narr, 1996; Bai and Pollard, 2000; Nelson, 2001; Ghosh, 2017), and this relationship can be used for extrapolating fracture density on outcrops and subsurface when the other factors are constant. Some of the factors, such as distance to the fault plane, deformational history, initial burial depth, the extent of strain (displacement and curvature), and burial depth (confining pressure) can also affect the fracture density (Hanks et al., 1997; Bai and Pollard, 2000; Nelson, 2001; Galvis-Portilla et al., 2016; Ghosh, 2017).

Characterizing natural fractures is a very important aspect of unconventional reservoir studies. A standardized multidisciplinary workflow is necessary to deliver a comprehensive and quantitative understanding of their contribution to fluid flow and well failure in the subsurface. This dissertation uses two target shales: the Woodford Shale in Oklahoma and Barnett Shale in

Texas to illustrate how the proposed new workflow can benefit the fracture characterization for shale exclusively.

CHAPTER II REFERENCES

- Aoudia, K., J. L. Miskimins, N. B. Harris, and C. A. Mnich, 2010, Statistical analysis of the effects of mineralogy on rock mechanical properties of the Woodford shale and the associated impacts for hydraulic fracture treatment design: 44th US Rock Mechanics Symposium and 5th US-Canada Rock Mechanics Symposium.
- Babadagli, T., 2002, Scanline method to determine the fractal nature of 2-D fracture networks: *Mathematical geology*, v. 34, p. 647-670.
- Babcock, E. A., 1973, Regional jointing in southern Alberta: *Canadian Journal of Earth Sciences*, v. 10, p. 1769-1781.
- Bai, T., and D. D. Pollard, 2000, Fracture spacing in layered rocks: a new explanation based on the stress transition: *Journal of Structural Geology*, v. 22, p. 43-57.
- Bergbauer, S., and D. D. Pollard, 2004, A new conceptual fold-fracture model including pre-folding joints, based on the Emigrant Gap anticline, Wyoming: *Geological Society of America Bulletin*, v. 116, p. 294-307.
- Brace, W., B. Paulding Jr, and C. Scholz, 1966, Dilatancy in the fracture of crystalline rocks: *Journal of Geophysical Research*, v. 71, p. 3939-3953.
- Busetti, S., K. Mish, and Z. e. Reches, 2012, Damage and plastic deformation of reservoir rocks: Part 1. Damage fracturing: *AAPG bulletin*, v. 96, p. 1687-1709.
- Chang, C., M. D. Zoback, and A. Khaksar, 2006, Empirical relations between rock strength and physical properties in sedimentary rocks: *Journal of Petroleum Science and Engineering*, v. 51, p. 223-237.

- Cho, Y., E. Ozkan, and O. G. Apaydin, 2013, Pressure-dependent natural-fracture permeability in shale and its effect on shale-gas well production: SPE Reservoir Evaluation & Engineering, v. 16, p. 216-228.
- Chopra, S., and K. J. Marfurt, 2007, Seismic attributes for prospect identification and reservoir characterization, v. 11, Society of Exploration Geophysicists Tulsa, Oklahoma.
- Cosgrove, J., and M. Ameen, 1999, A comparison of the geometry, spatial organization and fracture patterns associated with forced folds and buckle folds: Geological Society, London, Special Publications, v. 169, p. 7-21.
- Curtis, J. B., 2002, Fractured shale-gas systems: AAPG bulletin, v. 86, p. 1921-1938.
- Engelder, T., 1982, Is there a genetic relationship between selected regional joints and contemporary stress within the lithosphere of North America?: Tectonics, v. 1, p. 161-177.
- Erguler, Z., and R. Ulusay, 2009, Water-induced variations in mechanical properties of clay-bearing rocks: International Journal of Rock Mechanics and Mining Sciences, v. 46, p. 355-370.
- Fernández-Ibáñez, F., J. DeGraff, and F. Ibrayev, 2018, Integrating borehole image logs with core: A method to enhance subsurface fracture characterization: AAPG Bulletin, v. 102, p. 1067-1090.
- Friedman, M., and J. M. Logan, 1970, Microscopic feather fractures: Geological Society of America Bulletin, v. 81, p. 3417-3420.
- Gale, J. F., S. E. Laubach, J. E. Olson, P. Eichhubl, and A. Fall, 2014, Natural fractures in shale: A review and new observations Natural Fractures in Shale: A Review and New Observations: AAPG bulletin, v. 98, p. 2165-2216.

- Gale, J. F., R. M. Reed, and J. Holder, 2007, Natural fractures in the Barnett Shale and their importance for hydraulic fracture treatments: AAPG bulletin, v. 91, p. 603-622.
- Gale, J. F. W., and J. Holder, 2010, Natural fractures in some US shales and their importance for gas production: Geological Society, London, Petroleum Geology Conference Series, p. 1131-1140.
- Galvis-Portilla, H., D. Becerra-Rondon, D. Duarte, and R. Slatt, 2016, PS Rock and Fracture Characterization of the Woodford Shale along the I-35 Outcrop.
- Ghosh, S., 2017, Integrated studies on Woodford Shale natural fracture attributes, origin, and their relation to hydraulic fracturing, University of Oklahoma.
- Gross, M. R., M. P. Fischer, T. Engelder, and R. J. Greenfield, 1995, Factors controlling joint spacing in interbedded sedimentary rocks: integrating numerical models with field observations from the Monterey Formation, USA: Geological Society, London, Special Publications, v. 92, p. 215-233.
- Guo, Y., K. Zhang, and K. J. Marfurt, 2010, Seismic attribute illumination of Woodford Shale faults and fractures, Arkoma Basin, OK, SEG Technical Program Expanded Abstracts 2010, Society of Exploration Geophysicists, p. 1372-1376.
- Handin, J., and R. V. Hager Jr, 1957, Experimental deformation of sedimentary rocks under confining pressure: Tests at room temperature on dry samples: AAPG Bulletin, v. 41, p. 1-50.
- Hanks, C. L., J. Lorenz, L. Teufel, and A. P. Krumhardt, 1997, Lithologic and structural controls on natural fracture distribution and behavior within the Lisburne Group, northeastern Brooks Range and North Slope subsurface, Alaska: AAPG bulletin, v. 81, p. 1700-1720.

- Helbig, K., and L. Thomsen, 2005, 75-plus years of anisotropy in exploration and reservoir seismics: A historical review of concepts and methods: *Geophysics*, v. 70, p. 9-23.
- Hennings, P. H., J. E. Olson, and L. B. Thompson, 2000, Combining outcrop data and three-dimensional structural models to characterize fractured reservoirs: An example from Wyoming: *AAPG bulletin*, v. 84, p. 830-849.
- Hodgson, R. A., 1961, Classification of structures on joint surfaces: *American journal of science*, v. 259, p. 493-502.
- Hugman III, R., and M. Friedman, 1979, Effects of texture and composition on mechanical behavior of experimentally deformed carbonate rocks: *AAPG Bulletin*, v. 63, p. 1478-1489.
- Jaeger, J. C., N. G. Cook, and R. Zimmerman, 2009, *Fundamentals of rock mechanics*, John Wiley & Sons.
- Ladeira, F., and N. Price, 1981, Relationship between fracture spacing and bed thickness: *Journal of Structural Geology*, v. 3, p. 179-183.
- Liu, E., 2013, *Seismic fracture characterization: Concepts and practical applications*, Academic Press.
- Lockner, D., J. Byerlee, V. Kuksenko, A. Ponomarev, and A. Sidorin, 1991, Quasi-static fault growth and shear fracture energy in granite: *Nature*, v. 350, p. 39.
- Lorenz, J. C., and R. E. Hill, 1992, Measurement and analysis of fractures in core.
- Mauldon, M., and W. Dershowitz, 2000, A multi-dimensional system of fracture abundance measures: *Geological Society of America Abstracts with Programs*, p. A474.

- Milad, B., S. Ghosh, and R. M. Slatt, 2018, Comparison of rock and natural fracture attributes in karsted and non-karsted Hunton Group Limestone: Ada and Fittstown area, Oklahoma: *The Shale Shaker*, v. 69, p. 70-86.
- Narr, W., 1996, Estimating average fracture spacing in subsurface rock: *AAPG bulletin*, v. 80, p. 1565-1585.
- Narr, W., and I. Lerche, 1984, A method for estimating subsurface fracture density in core: *AAPG Bulletin*, v. 68, p. 637-648.
- Narr, W., and J. Suppe, 1991, Joint spacing in sedimentary rocks: *Journal of Structural Geology*, v. 13, p. 1037-1048.
- Nelson, R., 2001, *Geologic analysis of naturally fractured reservoirs*, Gulf Professional Publishing.
- Neves, F. A., M. S. Zahrani, and S. W. Bremkamp, 2004, Detection of potential fractures and small faults using seismic attributes: *The Leading Edge*, v. 23, p. 903-906.
- Olson, J. E., and A. D. Taleghani, 2009, Modeling simultaneous growth of multiple hydraulic fractures and their interaction with natural fractures: *SPE hydraulic fracturing technology conference*.
- Ortega, O. J., R. A. Marrett, and S. E. Laubach, 2006, A scale-independent approach to fracture intensity and average spacing measurement: *AAPG bulletin*, v. 90, p. 193-208.
- Park, R. G., 2013, *Foundation of structural geology*, Routledge.
- Peacock, D., and D. Sanderson, 1995, Pull-aparts, shear fractures and pressure solution: *Tectonophysics*, v. 241, p. 1-13.
- Price, N. J., 1959, Mechanics of jointing in rocks: *Geological Magazine*, v. 96, p. 149-167.
- Price, N. J., 1966, *Fault and joint development: in brittle and semi-brittle rock*: London, Pergamon Press.

- Sagy, A., and Z. e. Reches, 2006, Joint intensity in layered rocks: The unsaturated, saturated, supersaturated, and clustered classes: *Israel Journal of Earth Sciences*, v. 55.
- Sinclair, S. W., 1980, Analysis of macroscopic fractures on Teton anticline, northwestern Montana, Texas A&M University.
- Skehan, J. W., 1968, Fracture tectonics of southeastern New England as illustrated by the Wachusett-Marlborough tunnel, east-central Massachusetts: *Studies of Appalachian geology—Northern and maritime*: New York, Interscience Pubs, p. 281-290.
- Sone, H., and M. D. Zoback, 2013, Mechanical properties of shale-gas reservoir rocks—Part 1: Static and dynamic elastic properties and anisotropy: *Geophysics*, v. 78, p. D381-D392.
- Stearns, D., 1964, Macrofracture patterns on Teton anticline, northwest Montana: *Transactions of the American Geophysical Union*, v. 45, p. 107-108.
- Stearns, D., 1968, Certain Aspects of Fracture in Naturally Deformed Rock: *Nat. Sci. Foundation Advanced Science Seminar in Rock Mechanics*, p. 97-118.
- Stearns, D. W., and M. Friedman, 1972, Reservoirs in fractured rock: *Geologic exploration methods*.
- Török, Á., and B. Vásárhelyi, 2010, The influence of fabric and water content on selected rock mechanical parameters of travertine, examples from Hungary: *Engineering Geology*, v. 115, p. 237-245.
- Tsvankin, I., and V. Grechka, 2011, Seismology of azimuthally anisotropic media and seismic fracture characterization, Society of Exploration Geophysicists Tulsa, OK.
- Wang, F. P., and J. F. Gale, 2009, Screening criteria for shale-gas systems.
- Zoback, M. D., 2010, *Reservoir geomechanics*, Cambridge University Press.

CHAPTER III

**OUTCROP AND CORE BASED MULTISCALE BED BOUNDED
NATURAL FRACTURE CHARACTERIZATION AND FRACTURE
DENSITY CONTROLLING FACTOR STATISTICAL ANALYSIS:
WOODFORD EXAMPLE**

*This manuscript has been submitted to Marine and Petroleum Geology

ABSTRACT

The controlling factors of natural fracture distribution and density in the Woodford Shale are quantified in this study. The Upper Woodford Shale member in southern Oklahoma is exceptionally brittle due to the abundance of recrystallized radiolaria (chert) facies that is interbedded with clay-organic-rich shale facies. Bed-bounded fractures are well developed in the structurally active area. Two geologically related objects are characterized and compared to represent low confining pressure shallow surface condition (a Woodford Outcrop, named “I-35 roadcut” on the edge of the Ardmore Basin) and high confining pressure subsurface condition (a Woodford core, named “Hall 2B” near the Wichita Mountain front area) respectively. A statistical analysis workflow consisting of Principal Component Analysis (PCA) and Partial Least Square Regression (PLS) was proposed to quantify the controlling factors’ relationship and their Variable Importance for Projection (VIP) which reveals the contribution of each controlling factor to the fracture density. It has been discovered that natural fractures’ occurrence in shale reservoirs is impacted by three controlling factors: hardness, hard bed ratio (thickness percentage of hard beds within a unit interval), and bed frequency (number of beds within a unit thickness interval). The contributions among these controlling factors vary under different pressure conditions. Bed frequency (layering anisotropy) is the dominant controlling factor that contributes on average three

times more than the hard bed ratio and hardness to fracture density. Hardness's contribution to fracture density in the core is lower by 22% than the outcrop due to the increase in confining pressure. The analytical results highlight the importance of the layering effect on fracture density, which has often been overlooked or underplayed when estimating causes of fracturing in the subsurface. A new concept of Fracture Density Index (FDI) is defined and can be further applied to predict fracture density in other unconventional reservoirs.

INTRODUCTION

Natural fracture density is the key index that helps predicting fluid flow in unconventional reservoirs, and the controlling factors of fracture density has been introduced in Chapter II. Fracture density, a parameter used to describe the intensity of deformation, has various ways to represent and describe the fractures on different scales and objects (Figure 2.4). For this study, P_{20} , which is the number of fractures within a unit area, is used to represent fracture density on a Woodford outcrop and core.

Even though the correlations between these controlling factors and fracture density are well studied in different cases, most of the analysis is focused on a single controlling factor's effect which has some limitations. Firstly, it is barely possible to evaluate one controlling factor's impact on natural fracture density while keeping the other controlling factors constant. For example, in the same outcrop, even if the lithology and thickness along one bed are constant, the other controlling factors such as curvature or distance to the fault might still vary dramatically, which could make the fracture density different along the same bed. Secondly, fracture density is an outcome impacted by all the controlling factors simultaneously, thus the correlation coefficient of individual controlling factors will be diminished by the other controlling factors. Thirdly, even if the fracture density relationships with these controlling factors are well investigated, they only

represent the fracture density on a single bed, which does not directly reflect the fracture density in an interbedded case.

The goal of this chapter is to investigate the interaction of the three controlling factors and quantify the contribution of each to fracture density in both the shallow surface and subsurface conditions by studying natural fractures on the selected Woodford Shale outcrop and core. An integrated statistical analysis workflow is proposed to evaluate fracture density's correlations with the controlling factors which can be further applied to other fracture models.

INVESTIGATION TARGETS

WOODFORD I-35 OUTCROP

The I-35 Woodford Shale outcrop is located on the northern rim of the Ardmore Basin and southern flank of the Arbuckle anticline in Carter County, Oklahoma (Figure 3.1-a, b). There is an exposure of 81 feet of the Upper Woodford and 10 feet of the Lower Woodford member on the outcrop (Becerra et al., 2018) (Figure 3.1-d). The Woodford shale at the I-35 outcrop was originally deposited during late Devonian and early Mississippian time in the Ardmore Basin when the Southern Oklahoma Aulacogen (SOA) formed an NW-SE graben. The Arbuckle Orogeny took place at the end of the Pennsylvanian, which uplifted and folded the Woodford Shale strata at the northeast rim of the Ardmore Basin (Hoffman et al., 1974; Allen, 2000; Abouelresh and Slatt, 2012; Carlucci et al., 2014; Galvis, 2017) (Figure 3.1-c). This study mainly focuses on the 81 feet section of the Upper Woodford Shale for the reason of well-developed, bed bounded fractures in a brittle and ductile bed couplet structure (Slatt et al., 2012) (Figure 3.1-e).

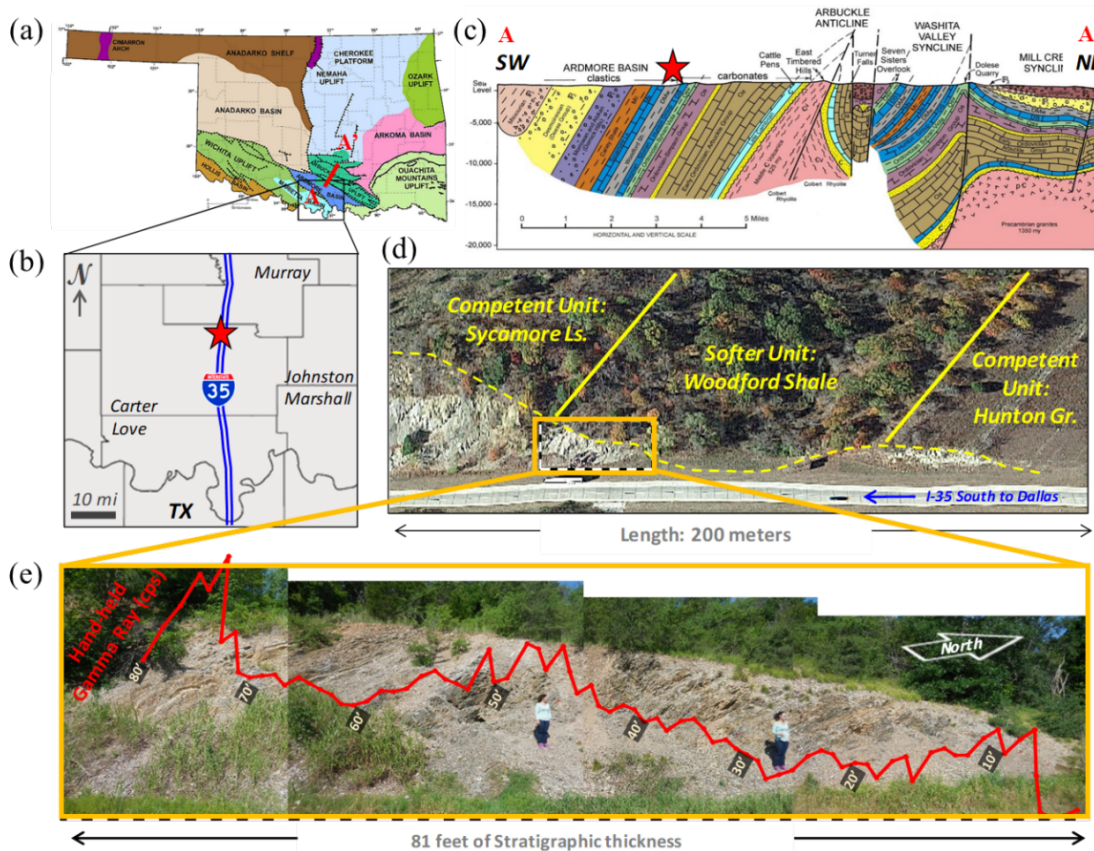


Figure 3.1: Location and overview of the I-35 Outcrop. (a) Oklahoma geological provinces and cross-section A-A' in red line across the Ardmore Basin and Arbuckle Uplift [Modified from Cardott (2012), originally from Campbell and Northcutt (1998)]. (b) closer display of the I-35 outcrop location (Becerra et al., 2018). (c) tectonic cross section highlighted in (a) as A-A'; approximate location of the study area is highlighted as a red star, the Woodford Shale (the gray strata in cross section) is dipping towards the southwest into the Ardmore Basin [Modified from Galvis-Portilla et al. (2016), originally from Ham and Amsden (1969)]. (d) Aerial photograph of the I35 outcrop showing the exposure of the Upper and Lower Woodford members, the Middle Woodford member was eroded into a valley due to its high clay content. Fracture characterization is mainly located in the section highlighted with the orange box which composed of 80 feet of the Upper Woodford member. (e) The Upper Woodford member photo mosaic has beds striking N65°W and dipping 48° towards the southwest. The outcrop gamma ray profile is projected on the corresponding measurement spots [modified from Becerra (2017)].

The Upper Woodford Shale on the I-35 outcrop is composed of interbedded chert and siliceous shale beds with an average bed thickness of 1.6 inches. The chert beds are blocky, dark gray to black, have fewer clay mineral compositions and are dominated by 94-98% of quartz with a high abundance of well-preserved radiolarians (Galvis-Portilla et al., 2016; Becerra, 2017;

Becerra et al., 2018). The siliceous organic-clay shale beds are dark brown with well-developed fissile laminations due to outcrop weathering. The mineral composition is high in organic matter and with scattered pyrite compared to the chert beds. Quartz in the siliceous shale beds is mainly the microcrystalline authigenic quartz that replaces the flattened *Tasmannites*; it ranges from 55% to 89% weight percentage. Illite is the main clay mineral that ranges from 10%-40% weight percentage (Becerra, 2017; Becerra et al., 2018). The strike orientation of the Woodford Shale is N65°E with a dip of 48° southwest, Becerra (2017) identified two groups of conjugate fractures striking N13°W and N52°W respectively and nearly vertical or sub-vertical to beds, which corresponds to Type 2 fractures on a fold (Stearns, 1968). The fractures on the I35 outcrop are mostly bed-bounded and generally well developed in the chert beds and less well developed in the siliceous organic-clay shale beds (Figure 3.2). The interbedded feature is a result of the periodic depositional environment and climate change or diagenetic processes (Davis, 1918; Chester and Aston, 1976; McBride and Folk, 1979; Murray et al., 1992; Hori et al., 1993). Interbedding has been well documented as a common feature of other marine shale deposits of a highstand systems tract (Bein and Amit, 1982; Beukes, 1991; Murray et al., 1992; Roberts et al., 1992; Hori et al., 1993; Chough et al., 1996; Johnson et al., 2001; Ikeda and Tada, 2013).



Figure 3.2: Interbedded chert and siliceous organic-clay shale on the I-35 outcrop. Red lines outline the siliceous and clay/organic rich shale that is weathered to light gray on the outcrop; green lines outline the chert beds that are massive and brittle. Note that most of the fractures are bed-bounded in the cherty beds but not extend to the siliceous shale, and density varies on these two different facies (Becerra, 2017).

WOODFORD HALL 2B CORE

To compare the fracture distribution pattern in the subsurface and shallower (outcrop) conditions, one drilling core that includes the Upper Woodford Shale named Hall 2B was selected. The Hall 2B core (API: 350152025) is located in a fault block in Caddo County, Oklahoma. It locates geologically within the Southern Oklahoma Aulacogen (SOA) depocenter and the northern rim of the Wichita Uplift (Figure 3.3a). The Woodford Shale in this area was uplifted dramatically during the Pennsylvanian Wichita Orogeny right after lithification of the Woodford Shale (Figure 3.3b) (Brewer et al., 1983; Granath, 1989; Keller and Baldrige, 2006).

The Hall 2B core is 122 feet long, which ranges from 6,156 feet to 6,278 feet measured depth. The core includes the upper part of the Middle Woodford member and the entire Upper Woodford member. Similar to the Woodford Shale in the I-35 outcrop, the Upper Woodford Shale

in the Hall 2B core is characterized by high frequency of interbedded chert and siliceous organic-clay rich shale. Fractures are bed-bounded in the brittle cherty beds and are subvertical to vertical or in conjugate sets, which both indicate that the maximum compressional stress during deformation age was perpendicular to the beds. Only a negligible number of fractures occur in the siliceous shale beds. The fracture sets correspond to a Type 3 fracture on the fold (Stearns, 1968) (Figure 3.4). Unlike the outcrop, the Woodford core section has a thinner average bed thickness of 0.5 inches and 45° average bed dip (Figure 3.4). Some of the fractures are sealed by siliceous and carbonate cement in the lower part of the core (Callner, 2014), the upper part of the core is mainly composed of opened, dissolution fractures. Most of the fractures in the core show a compressed geometry which means the fractures formed at a very early age within the strata and then underwent severe compaction. The filled fractures in the lower part of the core might form earlier than the open fractures in the middle and upper part of the core (Core description shown in Appendix A). The open fractures are rare to observe in subsurface conditions, there are two main interpretations of mechanisms that preserve the aperture of the fracture proposed for this case: 1. The open fracture was formed during the rapid uplifting stage of the strata, the rapid decrease in pore pressure acts as a supporting force to maintain the opened fracture geometry and probably even increase the aperture during the uplift. 2. The hydrothermal fluid in the subsurface promote the diagenesis and dissolution process along the previous failure plane so that the shear fracture plane in the upper and middle part of the core was dissolved and “washed” by the fluid, and ultimately turn out as opened fracture with large apertures.

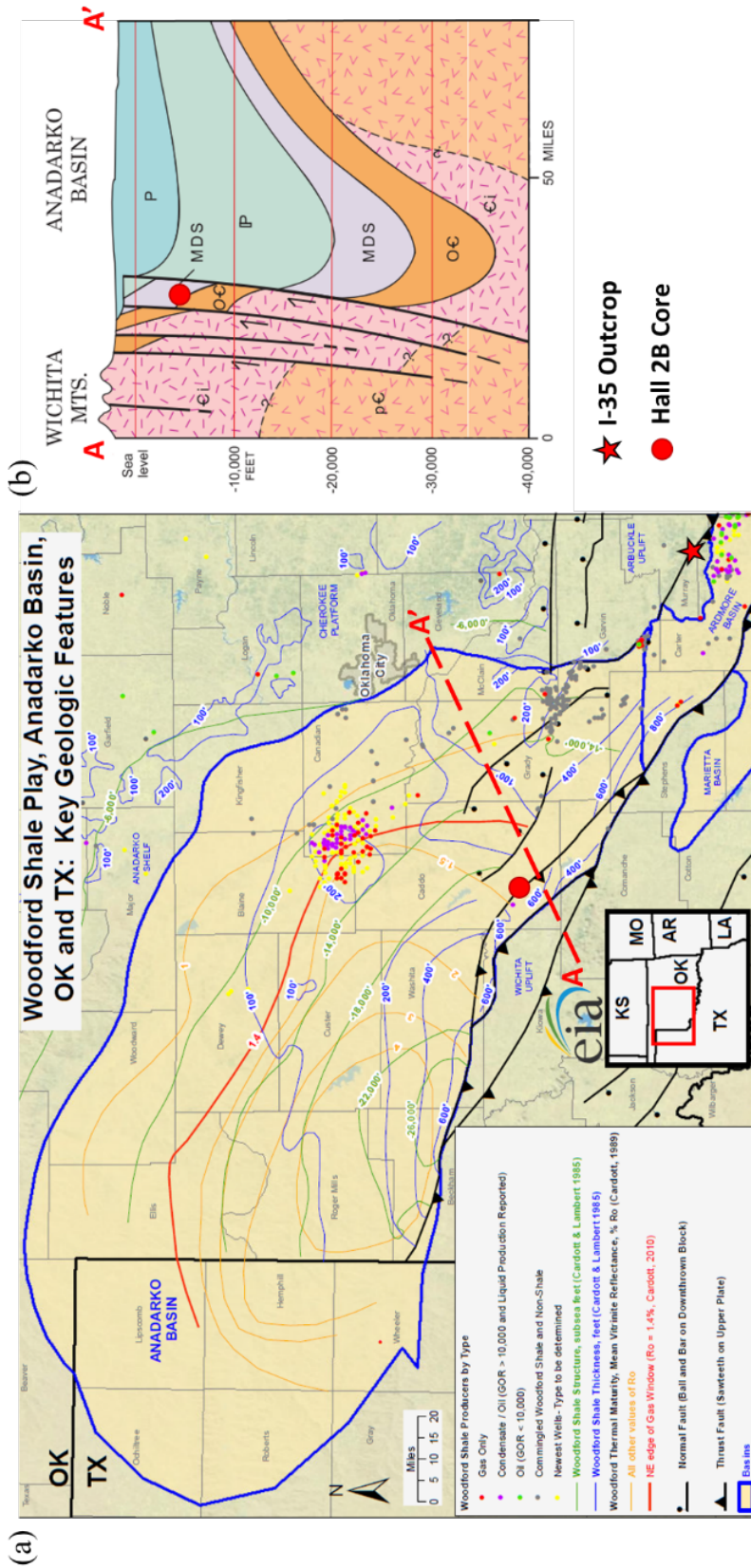


Figure 3.3: (a) the Woodford Shale structural and thickness map in western Oklahoma. The cross-section A-A' as outlined in the red dashed line is close to the Hall 2B core highlighted as a red dot. I-35 outcrop location is shown as the red star about 60 miles southeast of the core location [modified from EIA (2011)]. (b) cross-section A-A' shows Mississippian, Devonian, and Silurian strata which are represented by the "MDS" section in light purple color. The Woodford Shale section was uplifted by a series of reverse faults during the Wichita uplift and formed a larger burial depth contrast than the neighboring Woodford Shale section in the Anadarko Basin [Modified from Johnson and Luza (2008)].

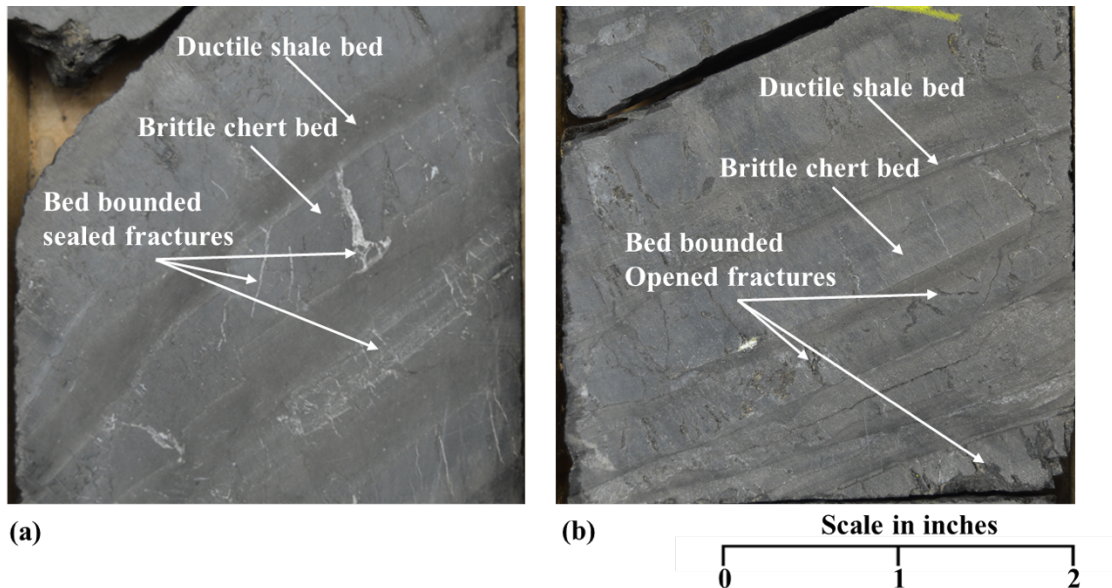


Figure 3.4: Hall 2B core beds are mainly steeply dipping with well-developed bed bounded fractures in the brittle cherty beds but not in the siliceous beds. Cherty beds are usually a light gray color and siliceous shale beds are dark brown. The bed thickness is thinner than the beds at the I-35 outcrop. (a) the lower part of the core is dominated by sealed fractures which are subvertical to vertical to the beds, the fractures are sealed by carbonate and siliceous cement. (b) opened dissolution fractures in the upper part of the core, the fractures are subvertical to vertical to the beds.

METHODOLOGY

FRACTURE CHARACTERIZATION

To incorporate the variability introduced by the interbed effect with the other known controlling factors for a larger scale fracture characterization, 2D fracture areal density, P_{20} , is recommended to represent interval fracture density. For this case study, 2D measurement windows for the I-35 outcrop and Hall 2B core are adjusted differently based on bed orientation and size of the measurable areas. Since the I-35 outcrop beds are dipping towards the southwest and fractures are mostly vertical to the beds, the 2D measurement window for the outcrop is defined as 1*1 foot square shape parallel to the beds (Figure 3.5b), the measurement windows are located through the entire Upper Woodford outcrop section. In the Hall 2B core, since the width of the core is constant

and the beds are dipping with a high angle, the 2D measurement windows for the core are designed as a parallelogram shape with edges parallel to the bed dip orientation, the size of the measurement windows for the core are roughly 3*3 inches to keep a consistent window area. Measured areas are converted into square feet unit so that can be comparable with the outcrop measurement window (Figure 3.5a). The Hall 2B core is highly segmented and some of the fractures are not ideal to be quantified due to severe deformation of the beds. Intervals with qualified conditions which has undisturbed bedding and obvious bed bounded fractures feature were selected for characterization. The actual area of each core measurement window was measured using the “ImageJ” image processing tool. The total number of the fractures were counted within each measuring window for both outcrop and core. The density of fractures was then calculated by the total number of fractures divided by the area of the measurement window. Eighty one fracture density measurement windows from the I-35 outcrop and thirty three fracture density measurement windows from the Hall 2B core were finalized for analysis and interpretation.

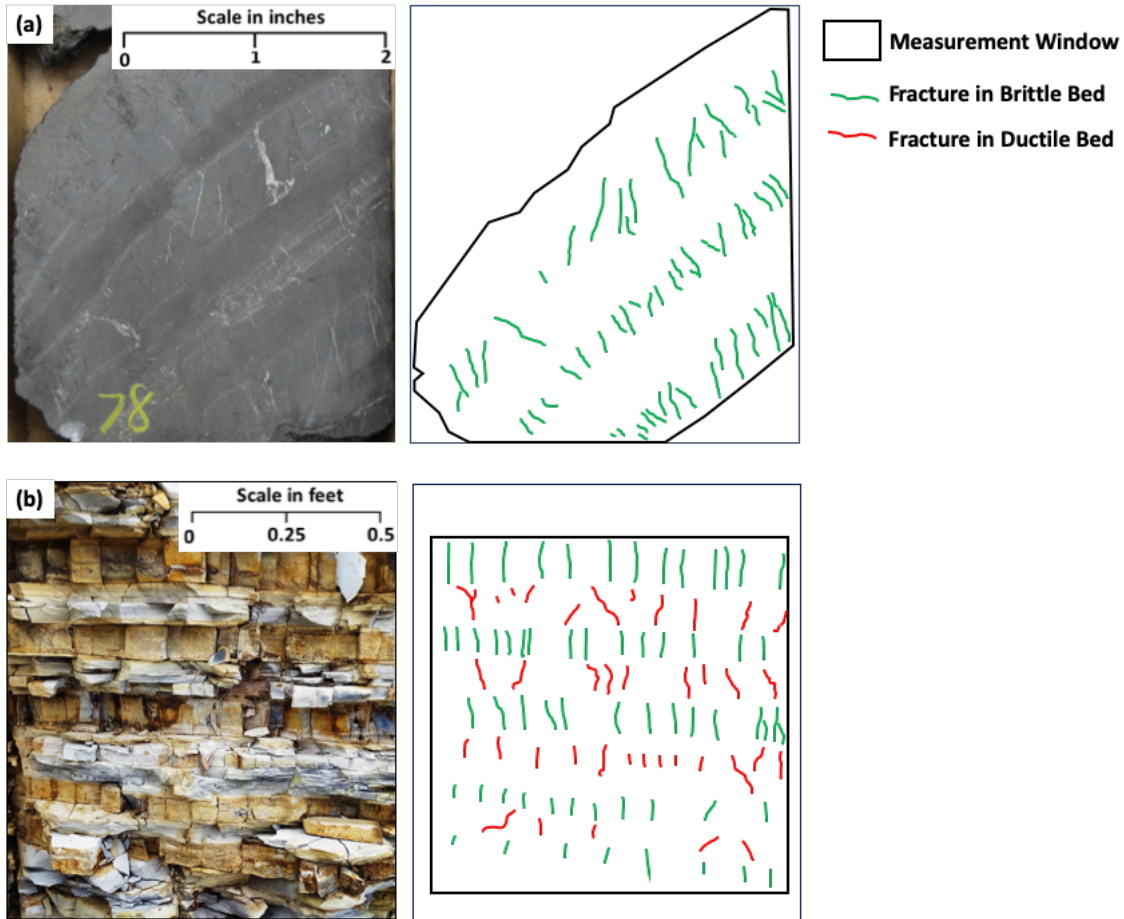


Figure 3.5: Demonstration of fracture density 2D measurement method for both core and outcrop. Scanning window is highlighted in black lines, bed bounded fractures in ductile clay-rich (siliceous shale) beds are outlined by red lines. Bed-bounded fractures in the brittle cherty beds are highlighted by green lines. (a) the measurement window in the Hall 2B core is selected where the fractures and bed boundaries are clear enough to identify. The size of the parallelogram shaped measurement window is not exactly the same, but the true thickness is controlled close to 3 inches to keep a general area consistency. (b) the outcrop measurement window keeps a 1 square foot area in the rectangular shape. Fractures within each window are counted.

The relative hardness of the rock samples was measured using the handheld Equotip Picolo 2TM hardness tester. The tester consists of an impact body using spring force to release a tungsten carbide ball against a flat, smooth contact surface of the sample. The ratio of the rebound velocity (V_r) to the release velocity (V_i) is used as the relative hardness as shown in Equation 3.1 (Leeb, 1979; Aoki and Matsukura, 2008; Ritz et al., 2014) (Figure 3.6). The fractured rock from the I-35

outcrop was collected and polished into a smooth surface with a rock saw; then the samples were placed on a stable level surface for relative hardness measurements. The core samples were already slabbed and polished thus did not require further sample preparation for relative hardness measurements. When measuring the hardness, five measurements along the same bed were conducted in the central part of the sample and average hardness was calculated to ensure result reliability and consistency.

$$\text{Hardness (LH)} = \frac{\text{Rebound velocity (Vr)}}{\text{Impact velocity (Vi)}} * 1000 \quad (3.1)$$

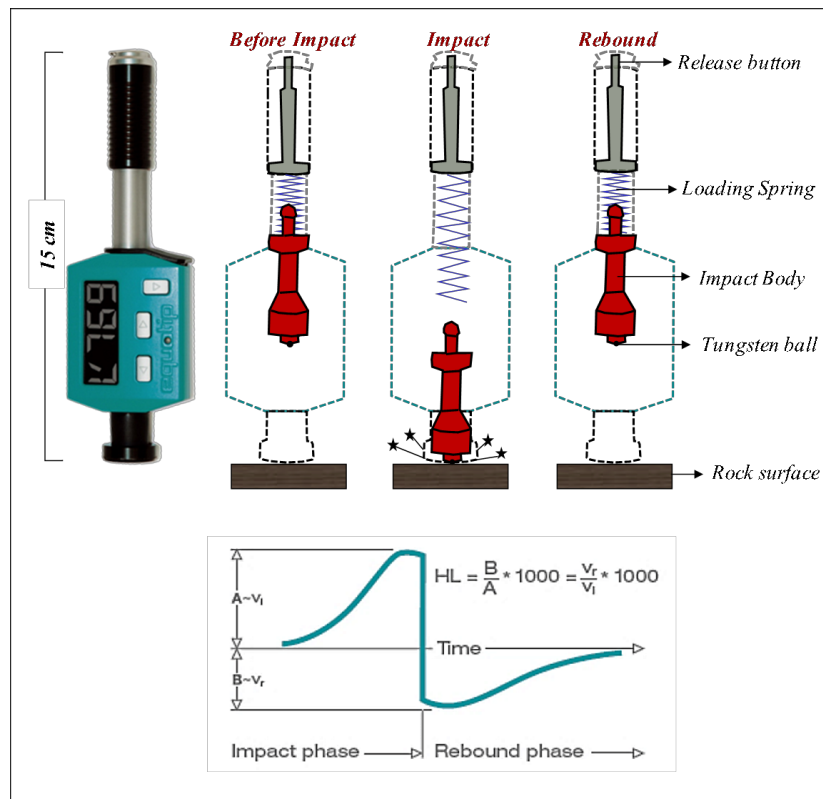


Figure 3.6: Schematic diagram of hardness measurement by the Equotip Pico 2 hardness tester. The internal structure of the impact body is spring mounted with a 3mm diameter ball in the base. The hardness value is the ratio between the rebound and impact velocities multiplied by 1000 (Becerra, 2017).

DATA PREPARATION

Once the fractures were counted, 2D fracture area density was calculated by the number of fractures in each measurement window divided by the area of the scanning windows in square feet units for both core and outcrop. 2D fracture area density P_{20} is able to incorporate the interbed effect and can be considered as upscaling of interval fracture density.

Since the fracture density is processed in a 2D scale. In order to maintain the consistency of the data during interpretation and analysis, the other controlling factors that also need to be reprocessed into 2D scale in order to correspond with the area fracture density. The hardness also needs to be upscaled to represent area average hardness, which is the weight averaged hardness by bed thickness in the measurement window using equation 3.2. This calculation considers the contribution of hardness from each bed in a selected interval, so true thickness needs to be used for the calculation.

$$H_I = \frac{\sum_{i=1}^n H_i * T_i}{\sum_{i=1}^n T_i} \quad (3.2)$$

H_I : Interval hardness.

H_i : Hardness measured on a single bed.

T_i : Thickness for the single bed which H_i is measured (feet).

The bed thickness effect on fracture density in a 2D scale can be represented by a proposed controlling factor named bed frequency. The bed frequency in this work is defined as the number of beds in a 1-foot thick interval for both core and outcrop which is equivalent to average bed thickness within the measured interval. The bed frequency can also be used as an indicator of vertical transverse isotropy (VTI) intensity. On top of the bed frequency, hard bed ratio, the accumulated net thickness of the cherty beds within a 1-foot thickness interval, is defined as another upscaled controlling factor in 2D space. There are studies indicating that quartz is a main

contributing mineral candidate of shale brittleness. Thus, cherty bed percentage in unconventional shales is supposed to affect the density of fracture occurrence (Narr and Suppe, 1991; Nelson, 2001; Wang and Gale, 2009; Guo et al., 2013; Becerra, 2017; Becerra et al., 2018).

DATA ANALYSIS

This study aims to integrate and quantify the proposed controlling factors' (brittleness, hard bed ratio, bed frequency) impact on 2D fracture area density. Since all the controlling factors interact and contribute to the fracture density, it is necessary to quantify and differentiate the contribution from each one of them.

Once data from the outcrop and core are properly prepared and standardized, each controlling factor's correlation and contribution to the 2D fracture area density was evaluated by the regression model. The evaluation workflow assumed the fracture density as a dependent variable related to a function that includes brittleness, hard bed ratio, and bed frequency as independent variables. The impact factor of each independent variable to the dependent variable and their correlations are obtained by the workflow demonstrated in Figure 3.7. The first step is to understand the correlation between each variable by comparing Pearson Correlation. Pearson Correlation can provide the overview of the relationship between independent variables and their correlation with dependent variables (here as fracture density). The higher the value indicates higher linear correlation between the compared variables (Pearson, 1901; Benesty et al., 2009). For the second step, the Principal Component Analysis (PCA) method is conducted on all the variables after data standardization. The PCA method can not only reduce the dimension of a large quantity and types of data but also can conduct a factorial analysis of the mixed dataset. It is used when there is a correlation between variables and finds the direction of maximum variance in the data as principal components (Wold et al., 1987; Abdi and Williams, 2010; Jolliffe, 2011). In order

to find a linear correlation of these variables, the principal components defined by eigenvalue and eigenvectors of the correlation matrix instead of the covariance matrix of variables is used (Jolliffe, 2011). Once the result of PCA is obtained, factor loading and factor accumulated variability are incorporated and compared between the outcrop and core data. The third step is to run a Partial Least Squares Regression (PLS), which is a commonly used projection method that generalizes the idea of Principal Component Analysis (PCA) and Ordinary Least Squares Regression (OLS). Since the variable of hardness and hard bed ratio is correlated, in order to overcome the error brought by multicollinearity in a typical multiple linear regression, PLS is a better option with higher calculation stability since it estimates the projection matrix for dependent variable and independent variables separately (Wold et al., 1984; Geladi and Kowalski, 1986; Wold et al., 1987; Myers and Myers, 1990; Garthwaite, 1994). Similar to PCA, part of the PLS result presents the correlation of controlling factors and dependent variables. It also provides the Variable Importance for the Projection (VIP) for each independent variable. The VIP is a quantitative parameter that best represents the contribution of each independent variable to the model (Mehmood et al., 2012).

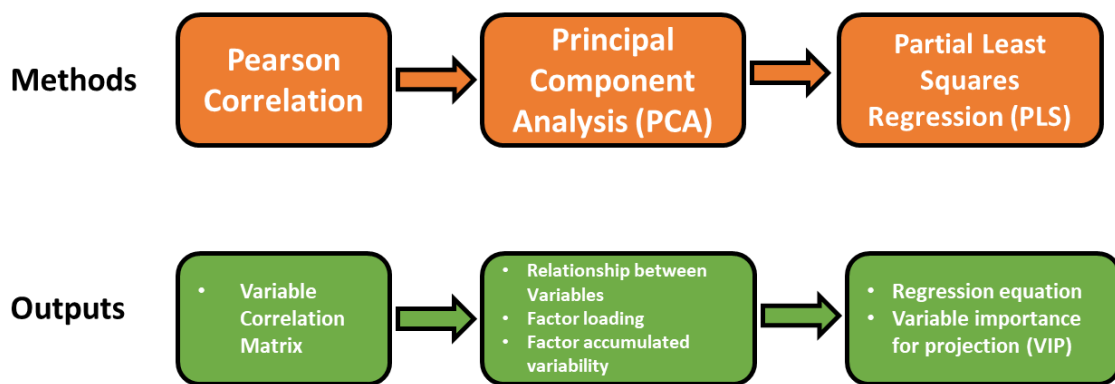


Figure 3.7: The data analysis flowchart and expected outcome from each step. The first step is to have a preview of variable correlation by calculating the Pearson correlation coefficient. The second step is to conduct the Principal Component Analysis to qualify the relationship between variables and calculate the factor loading. The third step is to construct a Partial Least Squares Regression model and obtain a quantified relationship between hardness, hard bed ratio, bed frequency and area fracture density then ultimately identify the contribution of variation from each independent variable.

RESULTS

From the Pearson Correlation result as shown in Table 3.1, the fracture area density are highly correlated with the bed frequency than the other two controlling factors for both outcrop and core. The correlation coefficient of the 2D fracture area density and bed frequency is even higher in the outcrop than core. The lower correlation coefficient from the core was interpreted to be due to the thickness change along the same bed by minor faults and folds, which occur throughout the core. When calculating bed frequency in the core measurement window, these deformations can introduce bias on bed thickness and fracture density. The beds in the outcrop are less disturbed by faults and maintain a constant thickness within the measurement window. Hard bed ratio and hardness are highly correlated in the outcrop and core since they both represent the rock mechanical property in different ways. The bed frequency for both outcrop and core are poorly correlated with hardness and hard bed ratio, which proves that bed frequency is an independent variable to hardness and hard bed ratio.

Table 1: the Pearson Correlation coefficient matrix of controlling factors and 2D fracture area density for both I-35 outcrop and Hall 2B core. High positive correlation between the fracture area density and bed frequency is observed from both. There is also high positive correlation between hard bed ratio and hardness since they both represent rock mechanical properties.

	Variables	Fracture Area Density	Hardness	Hard Bed Ratio	Bed Frequency
Outcrop	Fracture Area Density	1	0.230	0.299	0.905
	Hardness	0.230	1	0.784	0.296
	Hard Bed Ratio	0.299	0.784	1	0.314
	Bed Frequency	0.905	0.296	0.314	1
	Variables	Fracture Area Density	Hardness	Hard Bed Ratio	Bed Frequency
Core	Fracture Area Density	1	0.146	0.219	0.670
	Hardness	0.146	1	0.514	0.022
	Hard Bed Ratio	0.219	0.514	1	0.166
	Bed Frequency	0.670	0.022	0.166	1

The correlation between the dependent variable (fracture area density) and controlling factors/independent variables (hardness, hard bed ratio, bed frequency) are illustrated in Figure 3.8. The fracture density is set to a logarithm scale in Figure 3.8 and two separate scatter group

points stand out corresponding to core and outcrop fractures. The fracture area density between the outcrop and core shows a difference in magnitude: the fracture area density in the I-35 outcrop ranges from 0 to 242 (fracture/ft²) with an average of 84.07 (fracture/ft²). In the Hall 2B core case, the fracture area density ranges from 282.72 to 1575.6 (fracture/ft²) with an average of 645.83 (fracture/ft²). This magnitude difference is mainly caused by the difference in average bed thickness in these two cases. Even though the failure criterion increases with confining pressure under subsurface conditions, which indicates fracture intensity is supposed to decrease with depth for the same type of rock, the interbed effect surpasses the impact of confining pressure on fracture density in this case. Figure 3.8a-c show the correlation between fracture density to hardness, hard bed ratio and bed frequency. Only bed frequency shows a good correlation with the fracture density in both outcrop and core. The hardness from outcrop and core is generally different with higher value from core making it hard to define hard beds and soft beds from hardness values but can be differentiated better by lithofacies: cherty beds are hard beds and siliceous shale beds are softer beds. Figure 3.8d shows that the hardness and hard bed ratio are correlated, and the trend can be projected from the outcrop scale to the core scale.

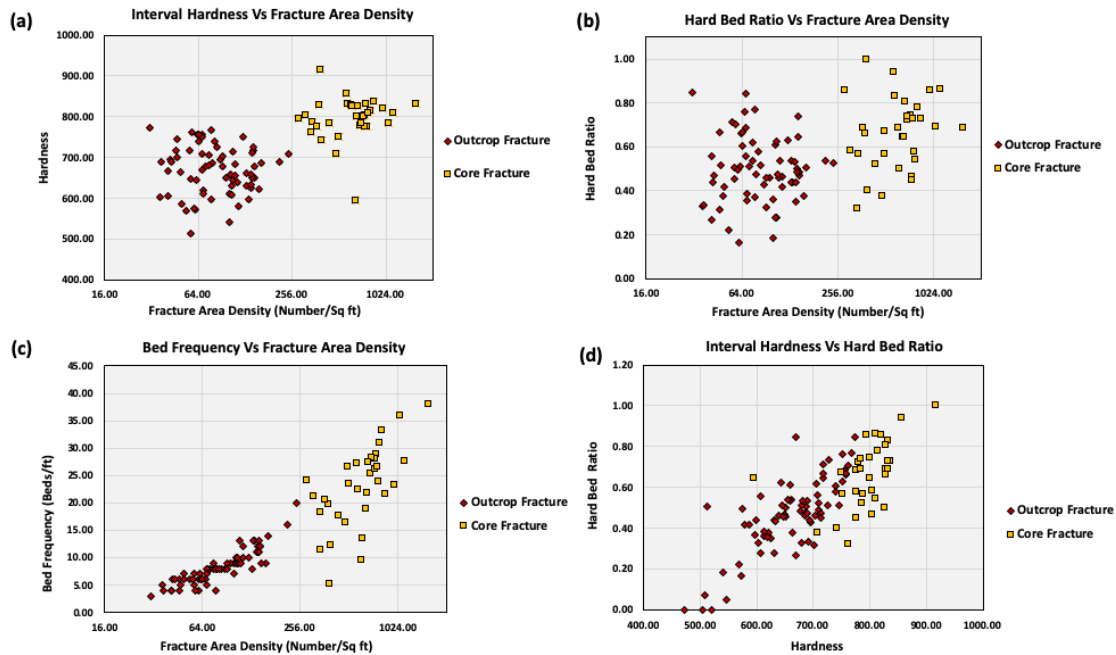


Figure 3.8: The correlation chart between variables, the fracture area density is shown in a logarithm scale to reveal the differences between outcrop and core fracture density caused by bed thickness magnitude difference. (a) Interval hardness vs fracture area density shows poor correlation for both outcrop and core. (b) Hard bed ratio and fracture area density are poorly correlated for both investigation targets. (c) Bed frequency has a very good correlation with fracture area density with a projectable trend from the outcrop scale to the core scale, the core scale correlation with fracture density is lower than the coefficient in the outcrop mainly due to the change in bed thickness along the lateral measuring section. (d) Hardness and hard bed ratio are well correlated with a projectable trend from the outcrop scale to the core scale.

The Principal Component Analysis (PCA) results show that two variable factors are sufficient to represent more than 80% of the variability of the dataset for both outcrop and core (Figure 3.9). For the first two variable factors, the corresponding eigenvalue is similar but higher in variable factor 1 on the outcrop case, which means that the outcrop dataset has higher correlation along variable factor 1 axis than the core dataset, the variable factor 3 and 4 will not be considered for data interpretation since they contribute negligible variability to the entire dataset. Table 3.2 shows the factor loading on each variable for both core and outcrop. Factor loading also called component loading, is the correlation coefficient between variables and factors which is similar to the Pearson Correlation coefficient. The higher the loading value the higher variance in the original

variable that is represented by the new factor. The variables have an acceptable loading range on variable factor 1 except for hardness in the core case. The hardness and hard bed ratio loading on variable factor 2 are higher which means that variable factor 2 represents more variability between these two variables. The variable correlations are shown clearly in Figure 3.10, the correlation circle is the projection of the initial variable in the variable factors space. The variables are plotted as vectors on the circle with two main variable factors as axes. The length of each vector on both diagrams is close to the boundary of the circle which means that two factors are sufficient to represent the original variables. Hardness and hard bed ratio vector are close to each other as a pair on both diagrams, but the core case has a relatively lower correlation than the outcrop case. Bed frequency and fracture density are highly correlated as another pair for both outcrop and core cases. Two pairs of variables are roughly orthogonal to each other which means the two pairs are barely correlated to each other.

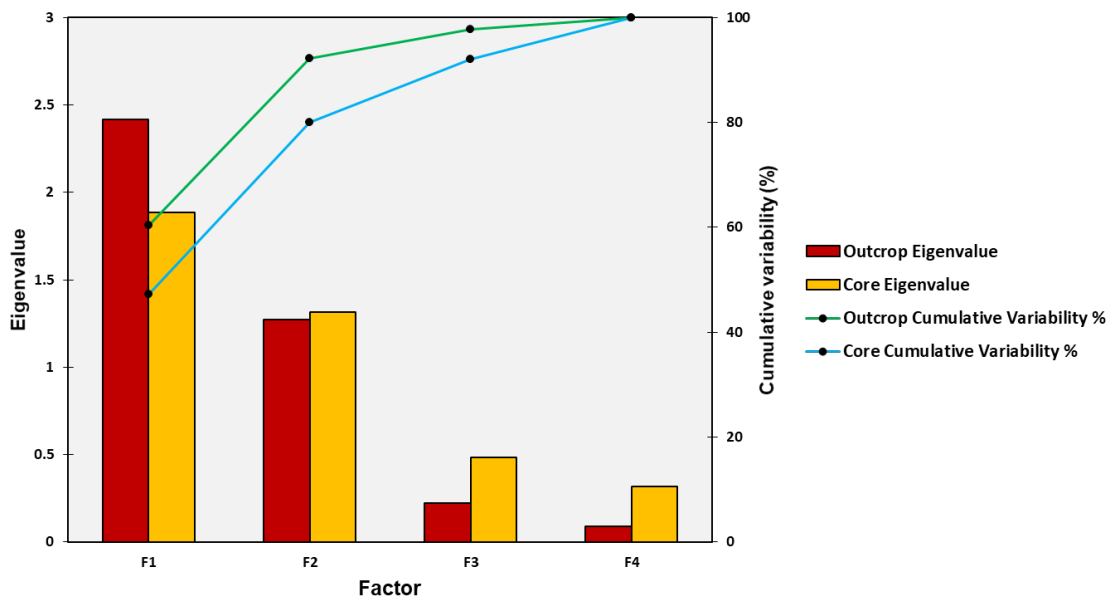


Figure 3.9: Factor variability and eigenvalue diagram for both outcrop and core cases. The column chart uses the primary vertical axis on the left representing the eigenvalue of each factor, the F1 has the highest eigenvalue which means it represents higher variability than the other factors and outcrop has a higher value than the core. The line chart uses the secondary vertical axis on the right to represent the cumulative variability for each factor.

Until variable factor 2, more than 80 % of the variability can be represented, thus factors 1 and 2 together are sufficient to present the dataset as new variables.

Table 2: Factor loading summary table for both outcrop and core. The F1 factor loading is higher on the outcrop case than on the core case.

		Factor loading	
Variable		F1	F2
Outcrop	Fracture Area Density	0.805	-0.554
	Hardness	0.719	0.615
	Hard Bed Ratio	0.751	0.570
	Bed Frequency	0.830	-0.512
Variables		F1	F2
Core	Fracture Area Density	0.806	-0.423
	Hardness	0.524	0.711
	Hard Bed Ratio	0.642	0.579
	Bed Frequency	0.742	-0.544

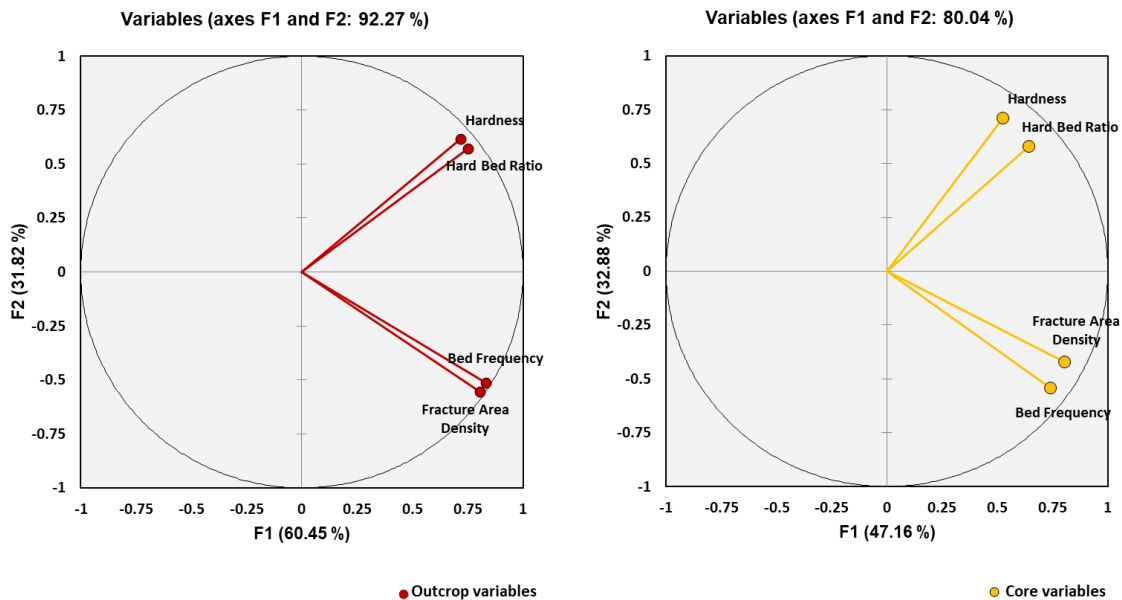


Figure 3.10: Variable circle for the I-35 outcrop (left) and Hall 2B core (right). The vectors of variables are all close to the edge of circles meaning that F1 and F2 space is sufficient to represent most variability in the original dataset. Hardness and hard bed ratio are tightly paired, and fracture area densities are tightly paired with bed frequency which means they are highly positively correlated. But two pairs are almost orthogonal which indicates that they are less well correlated. All the variables are on the positive axis of F1 which means the F1 factor is positively correlated to all the variables. Hardness and hard bed ratio are

projected to the positive axis of F2 which means they are positively correlated to F2. The same relationship is negative with bed frequency and fracture area density.

Partial Least Square Regression (PLS) conducted on the Hall 2B core and I-35 outcrop reveal two regression models with Variable Importance for the Projection (VIP). The regression model equations for both outcrop and core are shown below:

For the I-35 outcrop:

$$\text{Fracture area density} = 9.48 - 0.04 * \text{Hardness} + 10.94 * \text{Hard Bed Ratio} + 12.28 * \text{Bed Frequency}$$

For the Hall 2B core

$$\text{Fracture area density} = -259.51 + 0.32 * \text{Hardness} + 158.47 * \text{Hard Bed Ratio} + 24.12 * \text{Bed Frequency}$$

From the variable coefficients of both models we can conclude that all the controlling factors are positively correlated with the fracture area density (Figure 3.11). The outcrop PLS model has an ideal and trustable R^2 value of 0.8277. The R^2 value is relatively low for the core PLS model due to fewer data points and lower correlation between variables. The Variable Importance for Projection (VIP) is the most important outcome that directly quantifies the contribution of each independent variable to the dependent variable (model). The comparison diagram (Figure 3.12) shows the VIP results of the outcrop and core. The bed frequency shows about three times more importance than hard bed ratio and hardness in both core and outcrop cases. The difference between the outcrop and core bed frequency is not significant. The hard bed ratio has a similar lower VIP value for both outcrop and core. The hardness plays 22% less contribution in the core case, which is interpreted to be caused by an increase in confining pressure and failure envelope.

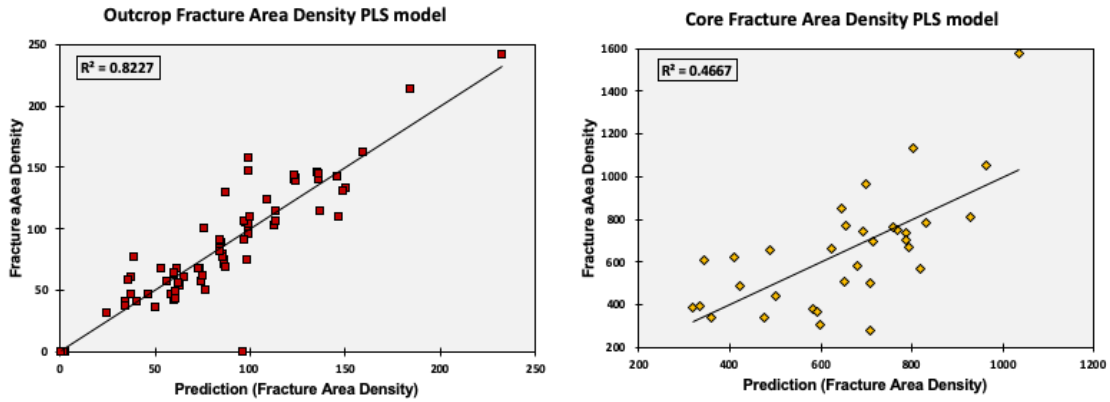


Figure 3.11: The PLS regression model result for both core (left) and outcrop (right). The horizontal axis is the modeled result compared with the actual measurement from the sample as the vertical axis. The regression coefficient is higher in the outcrop model due to higher correlation between controlling factors and more data points available.

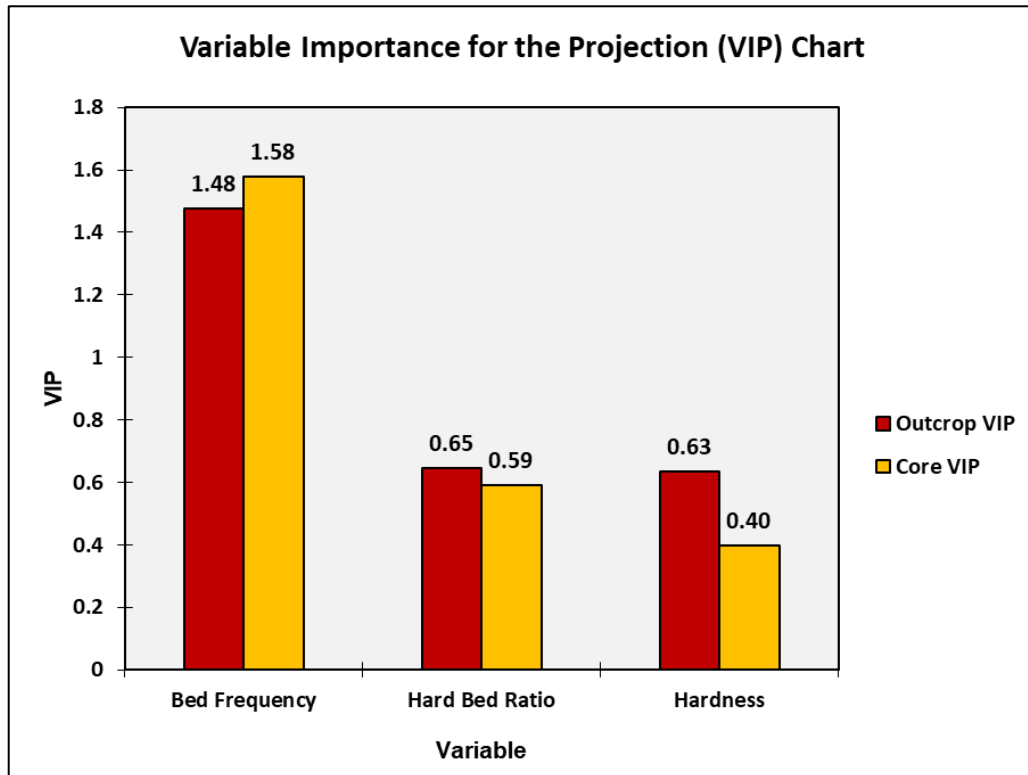


Figure 3.12: The VIP value comparison chart for the outcrop and core. VIP value is highest in bed frequency for both cases than the other two independent variables (hardness and hard bed ratio). This indicates that bed frequency plays a key role in controlling frac fracture density in both surface and subsurface conditions. Hard bed ratio's contribution is about the same for both cases, but the hardness contribution is less in the core case, which indicates hardness plays a less important role under the relatively high confining pressure.

Based on the PLS regression model and VIP interpretation result, a more general concept for area fracture density prediction is introduced as the Fracture Density Index (FDI) to evaluate a relative value of area fracture density (Equation 3.3). The VIP constants from the models are normalized and used as variable coefficients of the controlling factors for both subsurface and shallow surface scenarios to calculate FDI. The variables need to be normalized before calculating the Index in order to better emphasize the magnitude of contribution of each controlling factor.

(Outcrop Fracture Density Index) $FDI = 1.5 * Bed\ Frequency\ (Nom) + 0.7 * Hard\ Bed\ Ratio\ (Nom) + 0.6 * Hardness\ (Nom)$

(Core Fracture Density Index) $FDI = 1.6 * Bed\ Frequency\ (Nom) + 0.6 * Hard\ Bed\ Ratio\ (Nom) + 0.4 * Hardness\ (Nom)$ (3.3)

This index calculation method is extremely helpful when direct observation of natural fractures is not available, especially in the subsurface. Some of the fractures are not observable due to the limitation of the tool resolution. However, controlling factors can be estimated from the indirect measurement such as image log interpretation which provides the bed frequency reading. The other controlling factors such as hardness and hard bed ratio can be obtained as Young's modulus and Poisson's ratio calculated from a sonic log. Since the controlling factors quantification results are all normalized, data input type won't have an impact on FDI evaluation. The calculated FDI can then provide significant insight on fracture density and enhance a fluid flow model in the subsurface.

DISCUSSION AND CONCLUSIONS

From the statistics analysis results stated above, some conclusions on natural fracture density distribution can be reached as below

Single bed linear fracture density's relationship with bed thickness and hardness is difficult to be applied on a larger scale (for example the entire outcrop). 2D fracture area density is more suitable as an upscaled representative value of fracture density.

When interbed phenomena is well developed, which is common for this and other shale reservoirs, the relationship between hardness and fracture density is inferred and correlation is diminished after upscaling. Hardness will decrease the contribution to fracture density with an increase of burial depth due to the increase of confining pressure and failure envelope.

Bed thickness plays a more dominant role in fracture density in both shallow burial depth (outcrop) and the subsurface (core) than hardness and hard bed ratio. Higher frequency of interbeds within a vertical interval not only reduces the average bed thickness but also introduces anisotropy that contributes to fracability of the rock.

Fracture Density Index (FDI) can be used to estimate area fracture density for unconventional shales. Since the burial depths when the fractures occurred are not specific and clear in this study, future research can contribute further on empirical relationships between hardness VIP and depth relationships to quantify the effect of burial depth or confining pressure when deformation occurs and optimize the FDI equation.

The calculation method and relationship concluded in this research are specifically for bed-bounded fracture characterization. For the other cases when normal pressure is too high, the fracture can develop over the bed boundary and the relationship may be not applicable for this case fracture density prediction.

CHAPTER III REFERENCES

- Abdi, H., and L. J. Williams, 2010, Principal component analysis: Wiley interdisciplinary reviews: computational statistics, v. 2, p. 433-459.
- Abouelresh, M. O., and R. M. Slatt, 2012, Lithofacies and sequence stratigraphy of the Barnett Shale in east-central Fort Worth Basin, Texas Geohorizon: AAPG bulletin, v. 96, p. 1-22.

- Allen, R. W., 2000, Stratigraphy, mountain building and complex geological structures of the Ardmore Basin.
- Aoki, H., and Y. Matsukura, 2008, Estimating the unconfined compressive strength of intact rocks from Equotip hardness: *Bulletin of Engineering Geology and the Environment*, v. 67, p. 23-29.
- Becerra, D., 2017, Integrated geological characterization at the bed scale of the Woodford Shale at the I-35 outcrop: Southern Oklahoma: MS thesis, University of Oklahoma.
- Becerra, D., H. Galvis, and R. Slatt, 2018, Characterizing the two principal rock types comprising the Woodford Shale resource play: Application to shale geomechanics: Interpretation, v. 6, p. SC67-SC84.
- Bein, A., and O. Amit, 1982, Depositional environments of the Senonian chert, phosphorite and oil shale sequence in Israel as deduced from their organic matter composition: *Sedimentology*, v. 29, p. 81-90.
- Benesty, J., J. Chen, Y. Huang, and I. Cohen, 2009, Pearson correlation coefficient, Noise reduction in speech processing, Springer, p. 1-4.
- Beukes, B., 1991, A lithostratigraphic-sedimentological reference profile for the Late Archaean Mozaan Group, Pongola Sequence: application to sequence stratigraphy and correlation with the Witwatersrand Supergroup: *South African Journal of Geology*, v. 94, p. 44-69.
- Brewer, J., R. Good, J. Oliver, L. Brown, and S. Kaufman, 1983, COCORP profiling across the Southern Oklahoma aulacogen: Overthrusting of the Wichita Mountains and compression within the Anadarko Basin: *Geology*, v. 11, p. 109-114.

- Callner, S. A., 2014, An Integrated Approach to Understanding Sedimentary Structures and Depositional Processes in Devonian-Mississippian Black Shale: The Woodford Shale and Associated Strata in the Southern Midcontinent, Oklahoma State University.
- Campbell, J. A., and R. A. Northcutt, 1998, Geologic Provinces of Oklahoma, Basement Tectonics 12, Springer, p. 225-226.
- Cardott, B. J., 2012, Thermal maturity of Woodford Shale gas and oil plays, Oklahoma, USA: International Journal of Coal Geology, v. 103, p. 109-119.
- Carlucci, J. R., S. R. Westrop, C. E. Brett, and R. Burkhalter, 2014, Facies architecture and sequence stratigraphy of the Ordovician Bromide Formation (Oklahoma): a new perspective on a mixed carbonate-siliciclastic ramp: Facies, v. 60, p. 987-1012.
- Chester, R., and S. Aston, 1976, The geochemistry of deep-sea sediments, Chemical Oceanography (Second Edition), Elsevier, p. 281-390.
- Chough, S., S. Kim, and S. Chun, 1996, Sandstone/chert and laminated chert/black shale couplets, Cretaceous Uhangri Formation (southwest Korea): depositional events in alkaline lake environments: Sedimentary Geology, v. 104, p. 227-242.
- Davis, E. F., 1918, The radiolarian cherts of the Franciscan group, v. 11, University of California Press.
- Dershowitz, W. S., and H. H. Herda, 1992, Interpretation of fracture spacing and intensity: The 33th US Symposium on Rock Mechanics (USRMS).
- EIA, 2011, Woodford Shale play, Anadarko Basin, Oklahoma and Texas.
- Galvis, H., 2017, Detailed lithostratigraphic characterization and sequence stratigraphy of a complete Woodford Shale outcrop section in Southern Oklahoma, MS thesis, University of Oklahoma.

- Galvis-Portilla, H., D. Becerra-Rondon, D. Duarte, and R. Slatt, 2016, PS Rock and Fracture Characterization of the Woodford Shale along the I-35 Outcrop.
- Garthwaite, P. H., 1994, An interpretation of partial least squares: *Journal of the American Statistical Association*, v. 89, p. 122-127.
- Geladi, P., and B. R. Kowalski, 1986, Partial least-squares regression: a tutorial: *Analytica chimica acta*, v. 185, p. 1-17.
- Granath, J. W., 1989, Structural evolution of the Ardmore Basin, Oklahoma: Progressive deformation in the foreland of the Ouachita collision: *Tectonics*, v. 8, p. 1015-1036.
- Guo, Z., X.-Y. Li, C. Liu, X. Feng, and Y. Shen, 2013, A shale rock physics model for analysis of brittleness index, mineralogy and porosity in the Barnett Shale: *Journal of Geophysics and Engineering*, v. 10, p. 025006.
- Ham, W. E., and T. W. Amsden, 1969, Regional geology of the Arbuckle mountains, Oklahoma, v. 17, University of Oklahoma.
- Hoffman, P., J. F. Dewey, and K. Burke, 1974, Aulacogens and their genetic relation to geosynclines with a Proterozoic example from Great Slave Lake Canada.
- Hori, R. S., C.-F. Cho, and H. Umeda, 1993, Origin of cyclicity in Triassic-Jurassic radiolarian bedded cherts of the Mino accretionary complex from Japan: *Island Arc*, v. 2, p. 170-180.
- Ikeda, M., and R. Tada, 2013, Long period astronomical cycles from the Triassic to Jurassic bedded chert sequence (Inuyama, Japan); Geologic evidences for the chaotic behavior of solar planets: *Earth, Planets and Space*, v. 65, p. 351-360.
- Johnson, K. S., and K. V. Luza, 2008, Earth sciences and mineral resources of Oklahoma, Oklahoma Geological Survey.

- Johnson, S. D., S. Flint, D. Hinds, and H. D. V. Wickens, 2001, Anatomy, geometry and sequence stratigraphy of basin floor to slope turbidite systems, Tanqua Karoo, South Africa: *Sedimentology*, v. 48, p. 987-1023.
- Jolliffe, I., 2011, Principal component analysis, *International encyclopedia of statistical science*, Springer, p. 1094-1096.
- Keller, G., and W. Baldrige, 2006, The southern Oklahoma aulacogen, *Developments in Geotectonics*, v. 25, Elsevier, p. 427-436.
- Leeb, D., 1979, Dynamic hardness testing of metallic materials: *NDT International*, v. 12, p. 274-278.
- McBride, E. F., and R. L. Folk, 1979, Features and origin of Italian Jurassic radiolarites deposited on continental crust: *Journal of Sedimentary Research*, v. 49, p. 837-868.
- Mehmood, T., K. H. Liland, L. Snipen, and S. Sæbø, 2012, A review of variable selection methods in partial least squares regression: *Chemometrics and Intelligent Laboratory Systems*, v. 118, p. 62-69.
- Murray, R. W., D. L. Jones, and M. R. B. t. Brink, 1992, Diagenetic formation of bedded chert: Evidence from chemistry of the chert-shale couplet: *Geology*, v. 20, p. 271-274.
- Myers, R. H., and R. H. Myers, 1990, *Classical and modern regression with applications*, v. 2, Duxbury press Belmont, CA.
- Narr, W., and J. Suppe, 1991, Joint spacing in sedimentary rocks: *Journal of Structural Geology*, v. 13, p. 1037-1048.
- Nelson, R., 2001, *Geologic analysis of naturally fractured reservoirs*, Gulf Professional Publishing.

- Pearson, K., 1901, LIII. On lines and planes of closest fit to systems of points in space: The London, Edinburgh, and Dublin Philosophical Magazine and Journal of Science, v. 2, p. 559-572.
- Ritz, E., M. Honarpour, W. F. Dula, and J. P. Dvorkin, 2014, Core Hardness Testing and Data Integration for Unconventionals: Unconventional Resources Technology Conference, Denver, Colorado, 25-27 August 2014, p. 1128-1139.
- Roberts, C. T., R. Mitterer, K. Johnson, and B. Cardott, 1992, Laminated black shale-bedded chert cyclicity in the Woodford Formation, southern Oklahoma: Source Rocks in the Southern Midcontinent, Oklahoma Geological Survey, Circular, v. 93, p. 330-336.
- Slatt, R. M., N. Buckner, Y. Abousleiman, R. Sierra, P. R. Philp, A. Miceli-Romero, R. Portas, N. O'Brien, M. Tran, and R. Davis, 2012, Outcrop-behind outcrop (quarry): Multiscale characterization of the Woodford gas shale, Oklahoma.
- Stearns, D., 1968, Certain Aspects of Fracture in Naturally Deformed Rock: Nat. Sci. Foundation Advanced Science Seminar in Rock Mechanics, p. 97-118.
- Wang, F. P., and J. F. Gale, 2009, Screening criteria for shale-gas systems.
- Wold, S., K. Esbensen, and P. Geladi, 1987, Principal component analysis: Chemometrics and intelligent laboratory systems, v. 2, p. 37-52.
- Wold, S., A. Ruhe, H. Wold, and I. Dunn, WJ, 1984, The collinearity problem in linear regression. The partial least squares (PLS) approach to generalized inverses: SIAM Journal on Scientific and Statistical Computing, v. 5, p. 735-743.

CHAPTER IV

QUANTITATIVE ANALYSIS OF LAYERING EFFECT ON FRACTURE OCCURRENCE AND DISTRIBUTION PATTERN

*This manuscript has been submitted to Marine and Petroleum Geology

ABSTRACT

This chapter presents an experimental study that aims to quantify the layering effect and its impact on natural fracture distribution under a simple compressional regime. The layering anisotropy effect, has been recognized as the main source of vertical transverse isotropy in the Woodford Shale, USA, which can play an important role in natural fracture distribution, especially for the interbeds in shale with two mechanically different lithofacies. A compressional experiment on a clay model was designed specifically for simulating the brittle and ductile interbeds that are commonly observed in the Woodford and other unconventional shales. Brittle layers were represented by the air-dried modeling clay alternating with more ductile layers represented by plasticine. With the same accumulated model thickness, 1 cm, 0.75 cm, and 0.5 cm single layer thicknesses with 6, 8 and 12 number of layers respectively were made and compared under the same unconfined uniaxial compressional test. Fracture patterns were recorded and described during and after the tests. Nine types of fractures and seven stages of deformation were observed based on the fracture geometry and development sequence. Fracture intensity (P_{21}) was measured based on all the final test results, the comparison results indicate that there is an increase in simple shear fracture intensity from the 1 cm group to the 0.75 cm group. The fracture intensity decreases on the 0.5 cm group, which switches the deformation to dilating fractures instead of simple shear fractures. The overall results reveal the significance of the layering effect on fracture distribution in the Woodford and probably other shales: the layering effect is the primary factor in small scale

fracture distribution, which means the more the layers in the geobody, the higher the layering anisotropy intensity, and ultimately a higher deformation extent (larger aperture) under the same deformational process and stress regime.

INTRODUCTION

Since the shale boom, anisotropy has become a focused parameter when characterizing unconventional shale due to its nonnegligible impact on reservoir behavior. Historically, it was commonly accepted that marine shales, deposited in a relatively stagnant deep water environment contained reservoir properties that were evenly distributed both vertically and laterally when compared to conventional sand and carbonate reservoirs (Tariq et al., 1989; Johnston and Christensen, 1995; Higgins et al., 2008; Zhang et al., 2017; Zhang et al., 2019). Anisotropy in a reservoir was first mentioned by Dr. Maurice Rudzki in the 19th century as elastic wave parameter anisotropy. After that, reservoir anisotropy studies were conducted to further understand the mechanisms and quantify the variations using seismic data (Johnston and Christensen, 1995; Vernik and Liu, 1997; Wang, 2002; Sayers, 2005), subsurface logs (Esmersoy et al., 1994; Hatchell et al., 1995; Beckham, 1996) and hand samples (Jones and Wang, 1981; Sierra et al., 2010; Sone and Zoback, 2013). An anisotropic medium can be generally simplified and categorized into two types of transverse isotropy: Horizontal Transverse Isotropy (HTI) and Vertical Transverse Isotropy (VTI). The HTI medium is mainly contributed by vertical fractures and the VTI medium is contributed by layering (Dewhurst and Siggins, 2006; Sayers, 2013; Convers, 2017). In practical cases, these two types of anisotropy commonly occur simultaneously (Figure 4.1) (Helbig and Thomsen, 2005). For the shale reservoirs, usually the VTI medium forms first as original depositional interbed structures and also contributed by the stacking pattern of the

clay minerals at the microscale. The HTI medium is contributed by vertical or subvertical fractures that occur later and can be affected inevitably by the previous depositional structures.

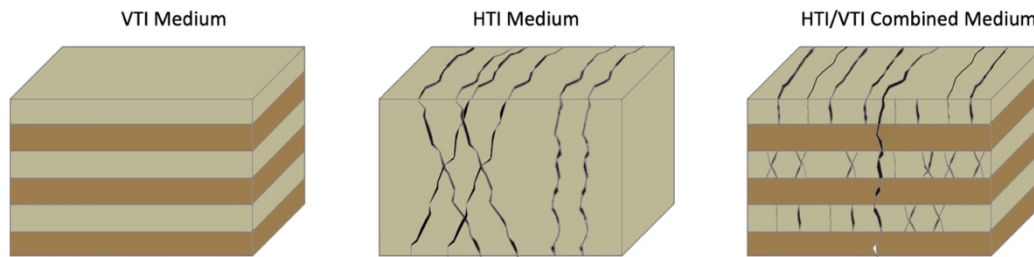


Figure 4.1: Schematic diagram of anisotropy types of shale reservoirs.

Where the interbed effect is observed and well-developed, there is commonly a relationship between interbeds and the distribution of natural fractures. The fractures are prone to develop as bed bounded forms in brittle layers which stop growing when hitting an adjacent geomechanically more ductile bed boundary (Ladeira and Price, 1981; Peacock and Sanderson, 1992; Gross et al., 1995; Varacchi, 2011; Gale et al., 2014; Becerra et al., 2018) (Figure 3.2). As described in Chapter III, the Woodford Shale reservoir interval is characterized by its interbeds of siliceous organic-clay shale beds (“ductile”) and cherty beds (“brittle”). Fractures mainly grow within the more brittle cherty beds and stop growing when they hit a bed boundary which acts as a micro fracture barrier surface.

According to Chapter III, the interbed effect has a deterministic impact on fracture density and geometry under the same deformational history and lithology for both surface and subsurface conditions, thus further quantifying the interbed’s impact on natural fracture distribution and fracture density is very important for prediction purposes in future characterization.

When characterizing fractures in the field, fracture distribution is affected by multiple factors at the same time such that it is difficult to analyze one factor exclusively on the fractures that have

already deformed. In order to have a simplified, manipulatable, and standardized regime for fracture characterization, a lab-based fracture simulation test is helpful.

High stiffness samples such as regular drilling core plugs are usually tested in a confined triaxial compressional setting which simulates the subsurface conditions and deformation process more realistically. Instead, low stiffness sample such as soil are tested by the uniaxial unconfined test to measure the shear strength. During the uniaxial unconfined test, a cylindrical sample is placed in a loading frame/chamber on a metal plate, and the axial strain and radial strain are measured during the test until the sample collapses. Stress and strain profiles are plotted to determine the sample strength and other mechanical properties. The profiles may vary for different rock types due to the different cohesion and internal friction. The deformation profile can be defined as four deformational behavior phases for brittle rocks: a crack closure phase, a crack initiation phase, a stable crack growth phase and a macro shear failure phase (Figure 4.2). For a material with high plasticity, the phases are hard to distinguish from the overall smooth curved profile (Cai et al., 2004; Zoback, 2010; Amann et al., 2011; Fakhimi and Hemami, 2017). Sahouryeh et al. (2002) conducted a series of biaxial compression tests on different materials (sandstone, concrete, and resin) to simulate fracture growth under different stress settings. Bobet and Einstein (1998) observed fracture coalescence under uniaxial and biaxial compression tests on different rock types. More specifically, Amann et al. (2011) conducted an unconfined uniaxial compression test on shale samples to study brittle behavior and concluded that the crack initiation threshold and damage threshold of the test samples. In their experimental setting, different than most of the previous studies that used relatively homogeneous small specimens, the Amann et al. (2011) study utilized a shale sample with interbedded sandstones and silts layers. However, there is barely any experimental focus on the interbed effect specifically during compressional tests in

order to restore and emphasize the layering effect observed from most of the marine shales (Cant, 1980; Pratt et al., 1986; Wheeler et al., 1990; Pasley et al., 1991; Ingall et al., 1993).

This study is designed as a specific experiment to determine the effect layering anisotropic has on natural fracture distribution patterns.

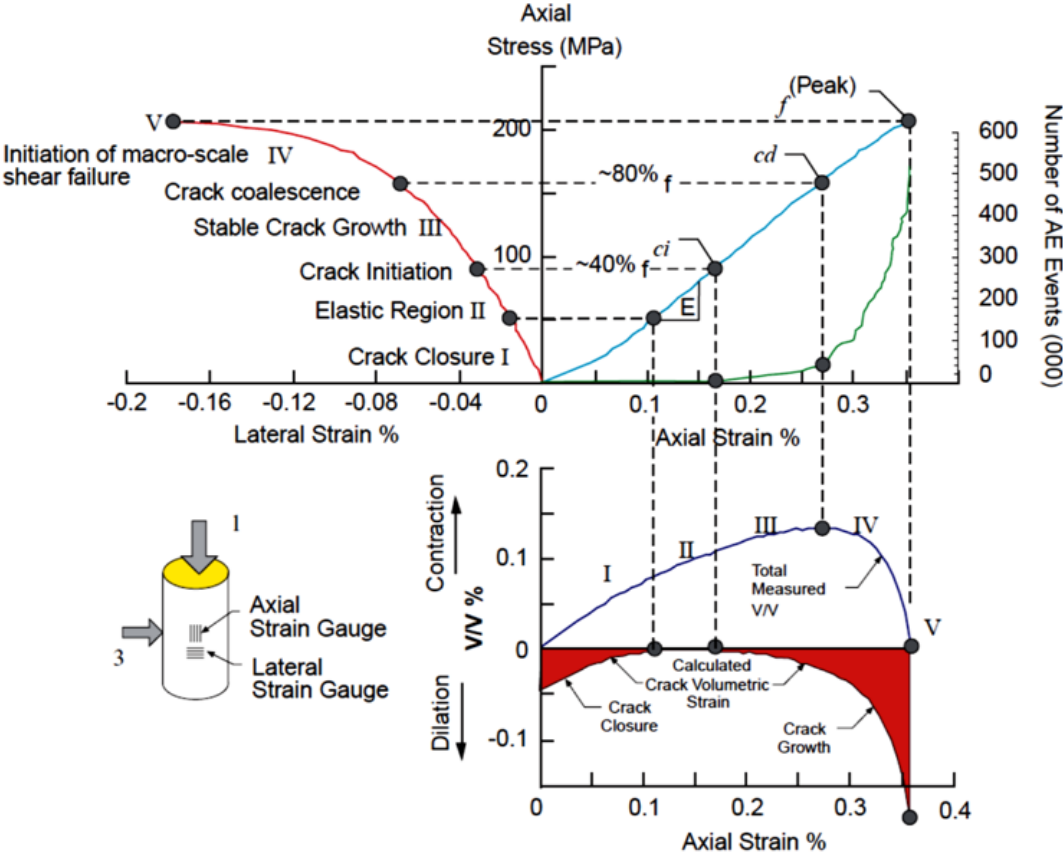


Figure 4.2: Damage behavior stages in stress and strain profile of brittle rock (Cai et al., 2004).

METHODOLOGY

MATERIAL DESCRIPTION

Unlike the traditional compressional tests that typically use the actual cylindrical shape brittle rock plugs, I used the air-dried modeling clay and plasticine as testing materials for the following reasons: (1) The natural rock sample is hard to have a perfect interbed depositional

structure in the measurable size; (2) Even though the layering can be captured as laminae in the selected brittle rocks, samples with controlled and idealized bed thickness are hard to obtain for comparison purposes; (3) naturally layered shale samples collected from the field can barely sustain their form during the regular compressional test and preferably break along the beds, which makes the compressional test challenging to achieve the expected deformational pattern, and (4) The manipulated materials help exclude the other potential disturbing factors that might introduce bias on the fracturing process such as different mineral composition and organic matter percentage between samples and preexisted micro failure plane within the samples.

The air-dried modeling clay (or sometimes called putty-clay) has been commonly used for structural pattern development analog models especially for extensional and shear structures such as a strike slip fault system (Lowell, 1972; Courtillot et al., 1974; Sylvester and Smith, 1976; Hempton and Neher, 1986; Reches, 1987; Reches, 1988; McClay and Dooley, 1995; Reches and Eidelman, 1995; Withjack et al., 1995; Withjack et al., 2007; Dooley and Schreurs, 2012). For compressional structures, the analog clay model was applied to fault bend folding and fault propagation folding mechanism but barely on fracture related studies since it is hard to fail the wet clay with high plasticity (Lowell, 1972; Jamison, 1991; Mitra and Islam, 1994; Withjack and Schlische, 2006). After the shaping and drying process, the air-dried modeling clay for this case study is relatively brittle compared to the plasticine, which never dries and maintains high plasticity. These two materials can be used together to form an analog of the brittle and ductile couplets observed from the outcrop. The brittle and ductile couplet concept was first introduced by Slatt and Abousleiman (2011) for the two most distinguishable lithofacies in the Woodford Shale: siliceous clay-organic rich shale and cherty shale which are interbedded and have sharp contrast in mechanical properties. This contrast in composition and mechanical properties leads to

differential deformation under the same stress regime and forms unique patterns of bed bounded natural fracture networks. Natural fractures usually develop better when these two facies are interbedded and equally distributed in percentage and thickness (Becerra et al., 2018).

EXPERIMENTAL SETUP

Similar to the typical kinematic clay model, the design of this scaled experiment tried to restore the fracture mechanism in a simple, conceptual and consistent setting that emphasizes the layering effect on fracture distribution under the compressional regime. Layered plasticine (ductile) and modeling air-dried modeling clay (brittle) were stacked to simulate the interbedded shale. Before setting up the experiment, both materials were flattened into sheets with three different thickness settings: 0.5 cm, 0.75 cm, and 1cm. The sheets then were cut into a circular shape with a diameter of 6.3 cm. The plasticine and air-dried modeling clay with the same thickness were stacked together after shaping to form a cylindrical clay cake model with an accumulated thickness of 6 cm. Three different stacking patterns were generated as 12, 8, and 6, cylinder layers respectively (Figure 4.3). The stacked models then underwent the drying process at room temperature for 1 hour to allow the modeling air-dried modeling clay layer to increase in brittleness while drying.

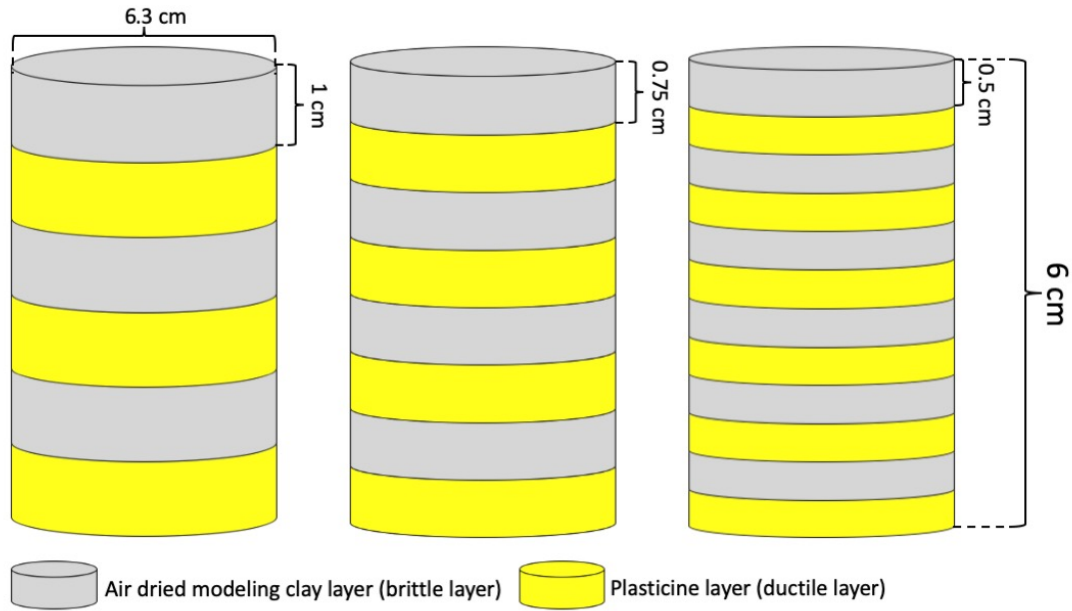


Figure 4.3: Dimension settings for different layer models.

Once the drying process was complete, the clay models were placed on a compressing stage, the top and base surface were firmly in contact with the loading plate, a vertical uniaxial compressive loading which is vertical to layers was applied with a negligible speed of 1 mm/min till the axial strain was 2 cm (the model became 4 cm tall). This vertical strain was chosen since it provided a sufficient number of fractures for observation and analysis. Further strain was avoided to avoid overly deformed samples and reality of the restoration process compared to the real-life situation (Figure 4.4). The process was repeated twice on each of the three models. The fracture intensity (P_{21}) was measured on the final result of compression and compared between different settings.

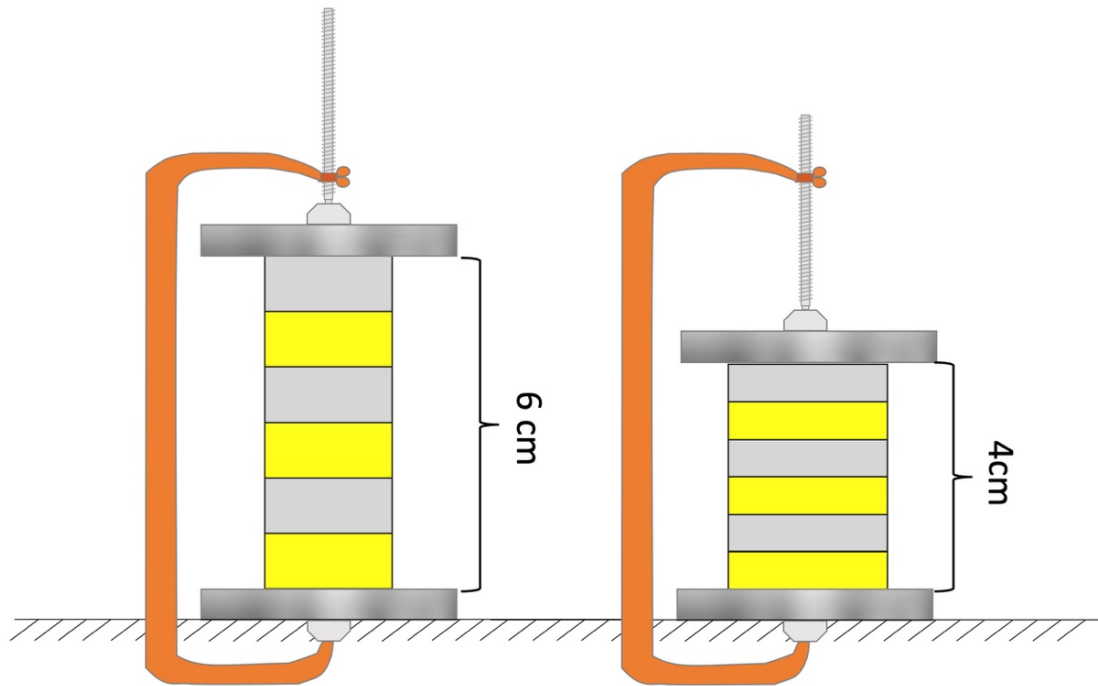


Figure 4.4: Uniaxial compression test applied to a 1cm layer clay model. The model was compressed with slowly under uniaxial stress (2 cm axial strain).

OBSERVATION METHODS

The fracture growth patterns were recorded during the compression tests and the final fracture pattern after the test was camera-scanned for further quantification of fracture distribution and density. The schematic diagram of the deformation model is demonstrated in Figure 4.5. During the test, the clay models underwent consistent vertical compressional stress that is perpendicular to the layers. Layers all showed high radial and axial strain due to high plasticity and unconfined condition. The fractures that occurred during the test were opened and shear. The aperture of the fractures is contributed by the large radial strain and the shear fracture patterns are due to the vertical axial strain. The photo mosaic of a cylindric clay model was made from the photos taken every 20 degrees angle of rotation. Since there are few fractures penetrating the entire model, P_{21} areal fracture intensity (Dershowitz and Herda, 1992), which is the accumulated length

of the fracture planes per unit area, was measured and used to better represent the extent of deformation on the final compressed clay models (Figure 4.6).

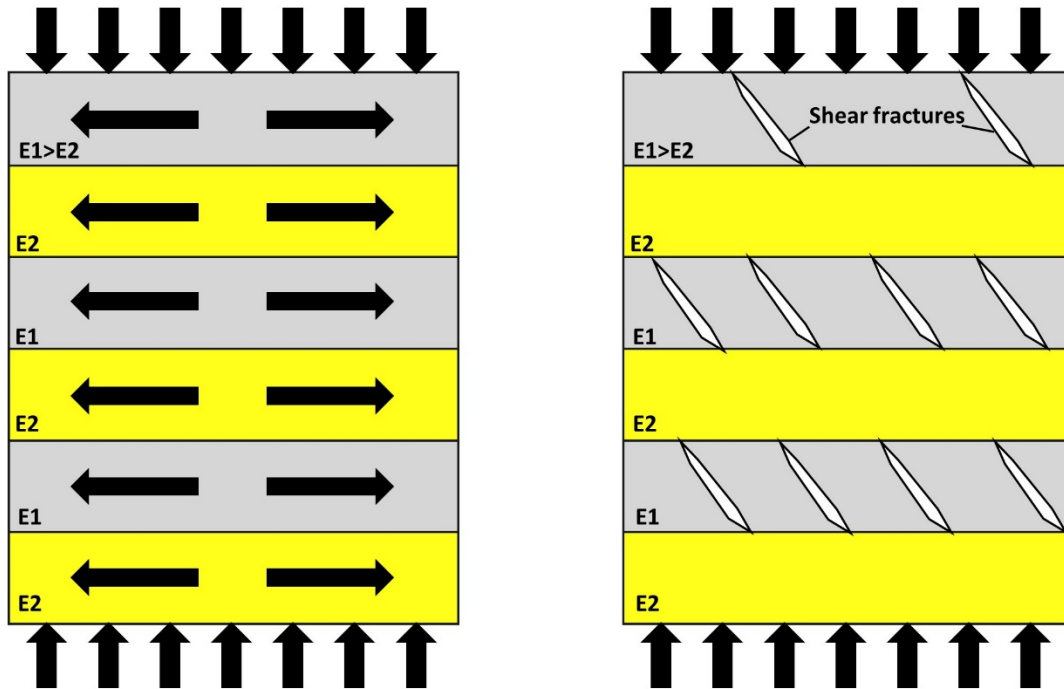


Figure 4.5: Demonstration model for fracture forming under uniaxial compressional stress and lateral radial strain. The left model indicates interbeds with high stiffness layers in gray and low stiffness layers in yellow. Under unconfined conditions the strain is not just axial but also radial. The right diagram illustrates shear fractures developed under compressional regime in the “brittle” layers which do not extend into the “ductile” layers. Aperture of the fracture is mainly caused by radial strain.

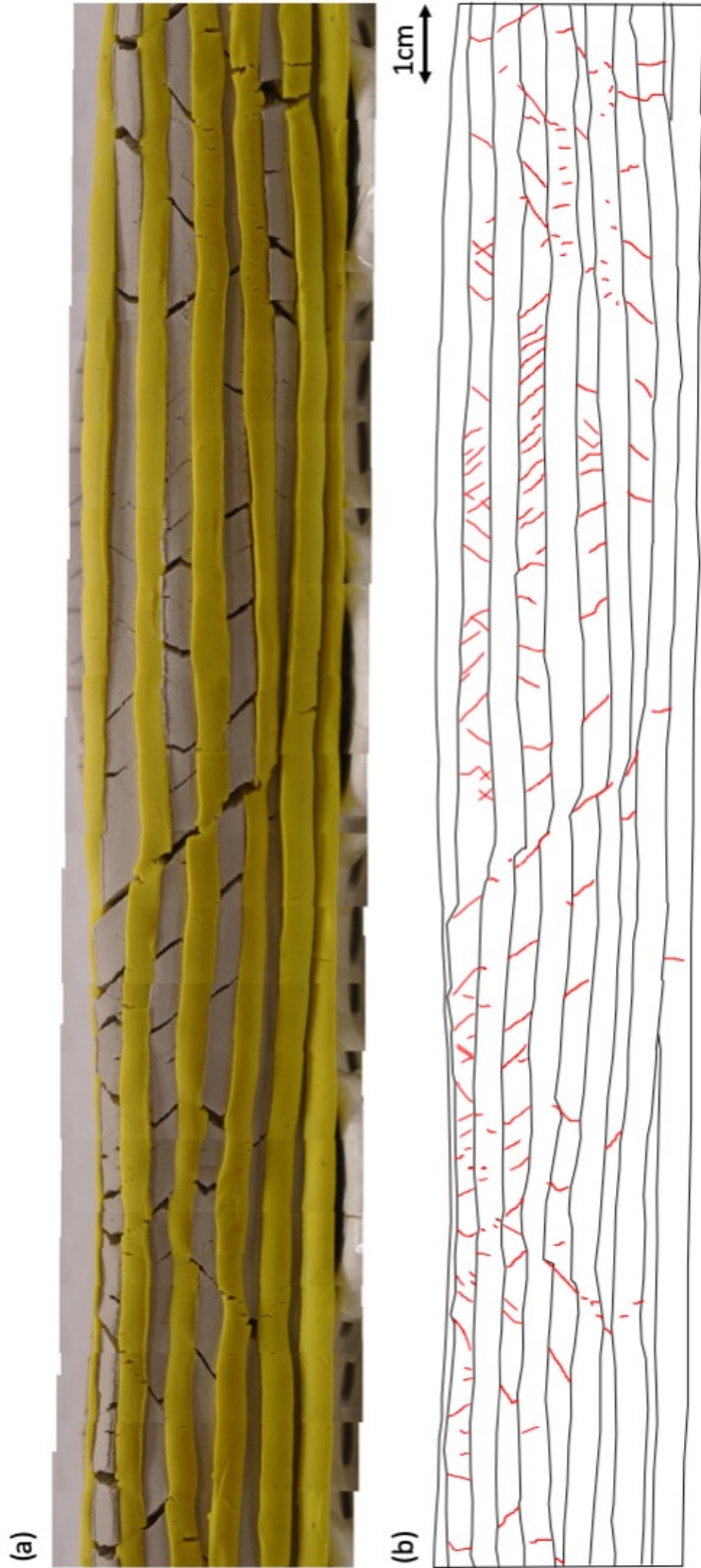


Figure 4.6: (a) The 0.5 cm thickness layer model after deformation. (b) Black lines indicate layers boundaries. Red lines indicate fractures.

RESULTS

FRACTURE DEVELOPMENT

Six experiments with three different initial layers thicknesses show a consistent pattern and geometry of fracture development. For all three different settings, the fractures only grow in the outer surface of the clay model due to the plasticity of the clay and radial strain on the surface. Fractures all start to grow in the brittle layers that distribute in the central layers of the clay model. The fractures are mostly shear/conjugate form with few vertical fractures. Nine types of bed-bounded fractures were distinguished based on geometry (Figure 4.7). Vertical fractures (Figure 4.7a), simple shear fractures (Figure 4.7b), simple half conjugate type a and b (Figure 4.7c-d), simple conjugate (Figure 4.7e), complex conjugates (Figure 4.7f), En Echelon fractures (Figure 4.7g), opened fracture (Figure 4.7h) and compressed opened fractures (Figure 4.7i). The simple shear and simple conjugate are the most common types in the brittle layers, subvertical to vertical tensile and En Echelon fractures are the most common types in the ductile layers.

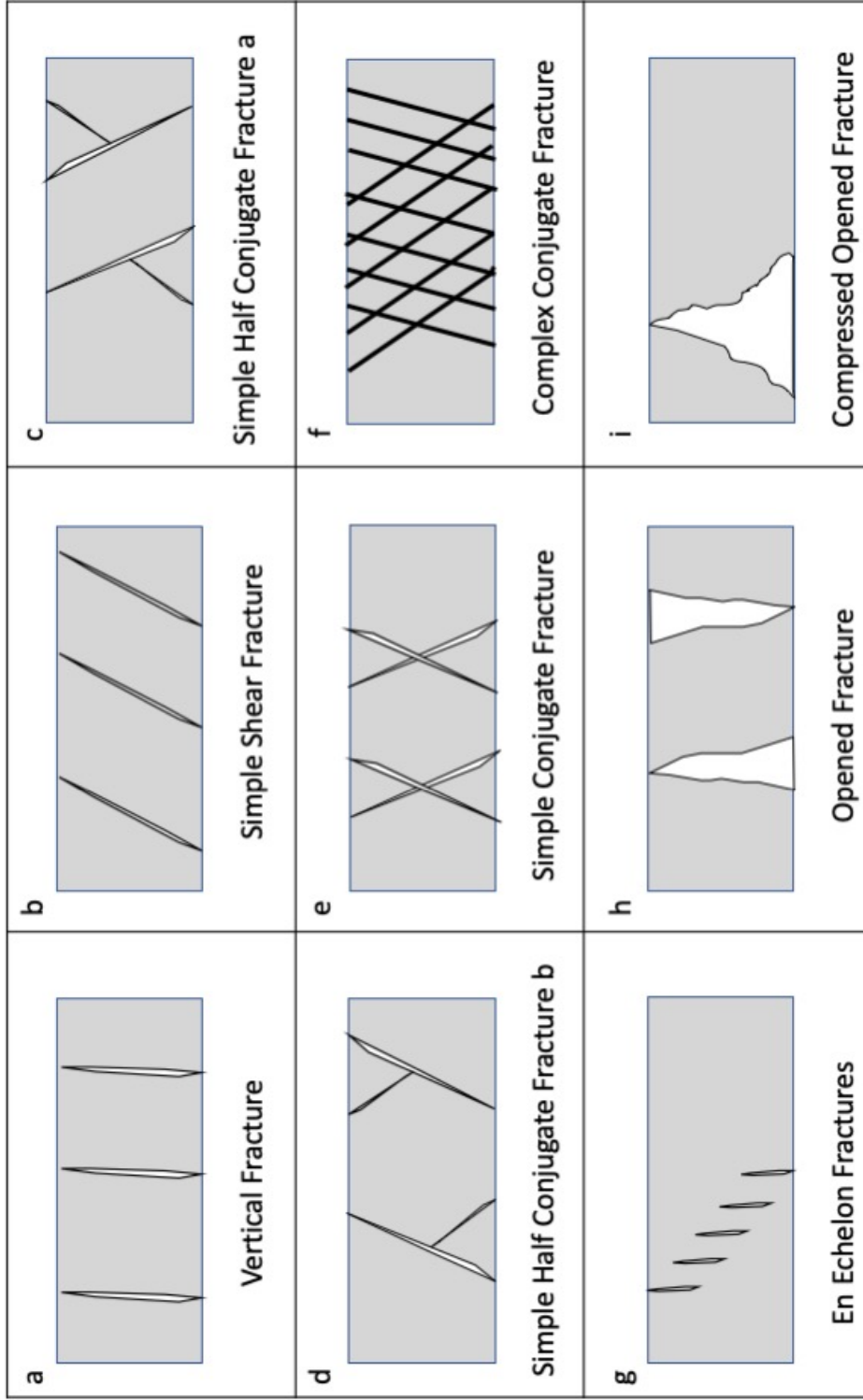


Figure 4.7: Eight Fracture types observed from the layer cake model experiment. (a) vertical fracture, (b) simple shear fracture, (c) simple half conjugate type a, (d) simple half conjugate type b, (e) simple conjugate, (f) complex conjugate, (g) En Echelon fractures, (h) opened fracture, and (i) compressed opened fracture.

During the experiment, fractures mainly developed in the brittle air-dried modeling clay layers with limited development in the ductile plasticine layers. The spacing between fractures remained relatively constant in all the fractured layers but was different for different layer thickness settings. The fracture development stage can be distinguished and described as seven stages in sequence (Figure 4.8): (1) in each brittle fractured layer, the fractures tend to initiate at the bottom and top boundary of the layer as pairs, the position of these top and bottom boundary fracture pairs are oblique which ultimately line up and forms a shear fracture; (2) when compression keeps increasing, the two initiation failure pairs start to grow and tend to connect from the top and bottom failure point; (3) when the growth continues, a complete shear or conjugate failure plane will form. This deformation process starts from the middle brittle layer and then starts to repeat the failure plane forming process in its neighboring brittle layers, the shear/conjugate planes in the neighboring brittle layers show a continuing dipping angle trend; (4) After most of the brittle layers are deformed with fractures, fracture aperture starts to increase from the oldest deformation plane and starts to form small triangle shape deformation initiation points from the top and bottom of the shear fractures in the ductile layers; (5) the en echelon failures start to form in the ductile layer as deformation continues; (6) the en echelon failures connect up and form a Riedel shear plan (R plane) which connect the previously deformed shear plane from the neighboring brittle layers that share the same dipping trend; and (7) The fractures start to connect between brittle and ductile layers and forms a penetration deformation plane; aperture of fractures starts to increase for all the deformation planes. All seven stages are observed for the 0.5 cm thickness setting layer cake model; the stage 1-4 most commonly occurring for 0.75 cm and 1 cm layer setting models, which means deformation in ductile layers is barely observed for those two

settings. The fractures that grow in the same layer might experience different stages at the same time based on the time of initiation.

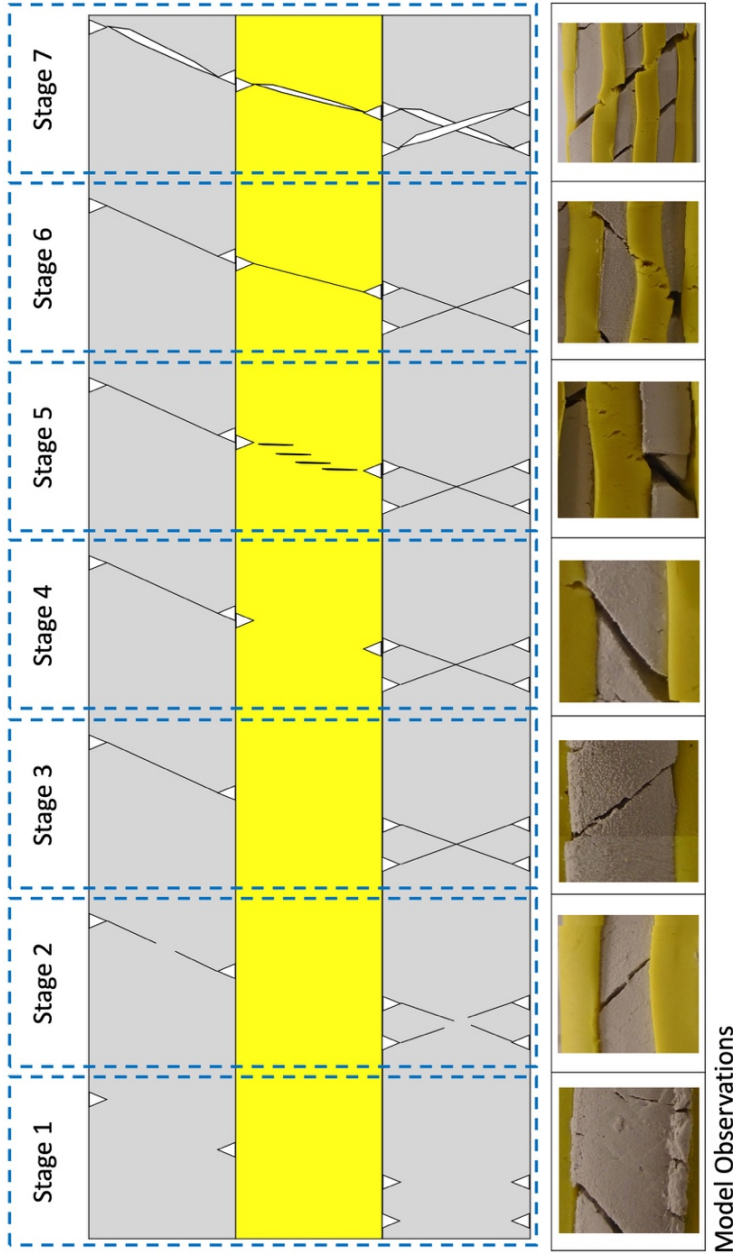


Figure 4.8: Fracture pattern deformation stages in the layering model. Stage 1 is the initiation of deformation with pinpointed tearing fractures. Stage 2 is the growing stage of the shear fractures that tries to connect the top and bottom initiation point in the same brittle layer. Stage 3 forms a connected pattern of shear or conjugate set of fracture planes within each brittle layers. Stage 4 starts to form the deformation initiation points in the ductile layers from the top and bottom part of the shear planes. Stage 5 starts to form an echelon failures in the ductile layers and those failures get interconnected in stage 6 which also connect the shear fracture plane with same dipping trends in the neighboring brittle layers. Once all the deformation pattern formed, the aperture starts to increase in the previous planes. Selected observations from the actual model for each stage are listed below.

FRACTURE INTENSITY TRENDS

Fracture intensities P_{21} are measured for all six experiments respectively and revealed a consistent trend of distribution. For the 1cm thick layer group, the fractures are mainly shear fractures and distributed in the middle two brittle layers; no fracture occurred in the ductile layer, and very few fractures show aperture (Figure 4.9). The fracture intensity is very low because low deformation occurred in the top and bottom layer with the same axial strain compared with the other two settings. The P_{21} values for the two repeated 1cm thick layer models are 0.83 and 0.79 respectively. For the 0.75 cm thick layer group, the fractures are mainly in shear and conjugate form with obvious higher fracture intensity in all brittle air-dried modeling clay layers; the top and bottom clay layers have fewer fractures. Very few fractures occurred in the ductile layers but some fractures in the brittle layer can be categorized as dilated fractures (Figure 4.7h). Shear deformation planes share a general uniform dipping angle and can be extrapolated from the neighboring brittle layers. The P_{21} values for the two repeated 0.75cm thick layer models are 1.04 and 1.25 respectively. For the 0.5cm thick layer group, the fractures are dominated by the dilated fractures (Figure 4.11). Some brittle layers are even imbedded by the overly deformed ductile layers with larger radial strain. Stage 6 and 7 deformation starts to develop and penetrates the entire model to form a bigger potential fluid highway. Vertical fractures (Figure 4.7a) and En Echelon fractures (Figure 4.7g) are commonly observed in this group. The P_{21} values for the two repeated 0.5cm thick layer models decrease towards 0.94 and 0.58 respectively, which is much lower than the 0.75 cm layer thickness group. Different from the other two settings, the deformation process for the 0.5 cm group has a transition from the pure shear deformation to the dilating deformational process. Once the fracture reached a saturation intensity, instead of developing the oversaturated shear fractures, it tends to open the current deformations and form higher aperture with bigger

stress shadow and ultimately lead to lower fracture intensity but higher aperture. The high aperture in this experiment is mainly contributed by its unconfined setting, thus for the fractures that form in the subsurface, the aperture is not expected as much as we observed from this experiment.



Figure 4.9: Layer clay model with 1cm thickness, the measured areas are outlined by red lines and the fractures are delineated by red thin lines.



Figure 4.10: Layer clay model with 0.75cm thickness, the measured areas are outlined by red lines and the fractures are delineated by red thin lines.



Figure 4.11: Layer clay model with 0.5cm thickness, the measured areas are outlined by red lines and the fractures are delineated by red thin lines.

Comparing the intensity between the three different settings, an increase in fracture intensity with the increase in layer frequency (number of layers in the model) can be observed from the 1cm layer thickness group to the 0.75cm layer thickness group. Then the trend starts to decrease when the layer thickness increases to 0.5cm due to the dilation of the fracture and bigger stress shadow (Figure 4.12). This decrease in intensity does not necessarily mean the extent of deformation decrease since P_{21} cannot properly represent aperture deformation of the fractures. Instead, the deformation extent increases with higher fracture porosity developed with higher layer frequency in the 0.5cm layer thickness model.

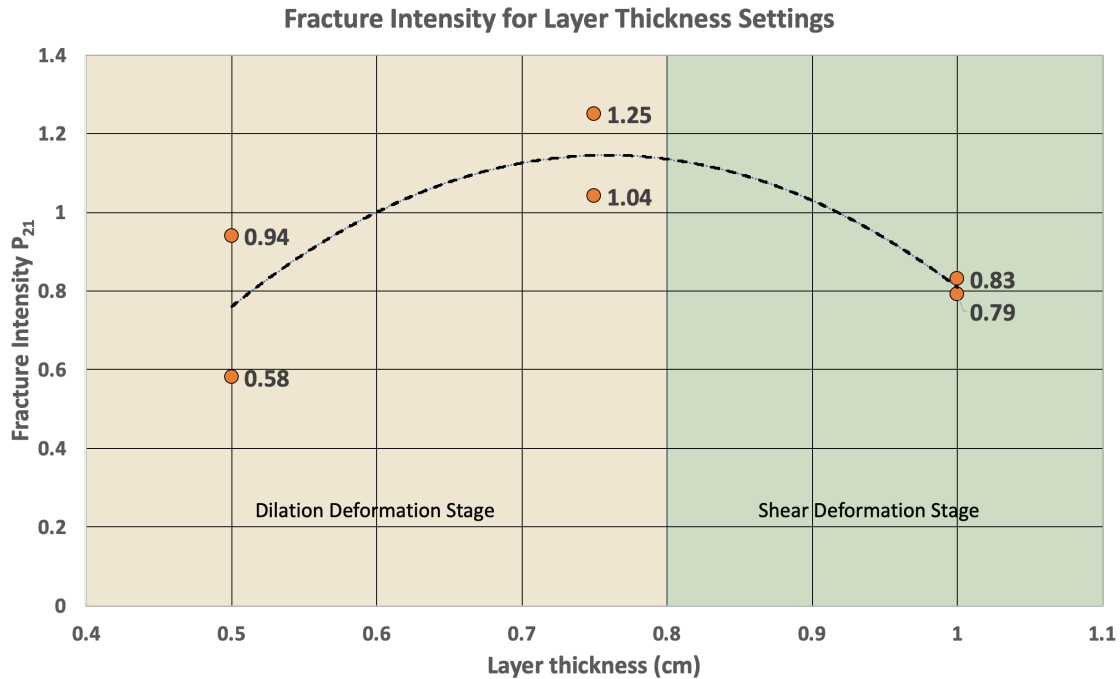


Figure 4.12: Fracture intensity's relationship with layer thickness. There is an increasing trend in the shear deformation stage which means the intensity increases with layer frequency. However, after the layer thickness reaches a certain lower limit, the aperture deformation stage starts to dominate and shows a decrease in fracture intensity but increase in fracture aperture.

LAYERING ANISOTROPY INDEX

From the observation of fracture deformation processes and fracture intensity's relationship with layer thickness settings, the layering effect obviously has an impact on fracture distribution and density of occurrence. The thickness of layers here in this experiment can be summarized as a representative of intensity of the layering effect, which can be considered as another index of layering anisotropy. Since layering anisotropy was well documented to have an impact on reservoir mechanical properties (Ladeira and Price, 1981; Dershowitz and Herda, 1992; Gross et al., 1995; Narr, 1996; Bai and Pollard, 2000; Slatt and Abousleiman, 2011; Gale et al., 2014), the index that can represent and quantify the layering effect and anisotropy is necessary. The Layering Anisotropy Index (LAI) is proposed here to emphasize the layering effect's contribution on medium anisotropy and can be expressed as:

$$\text{Layering Anisotropy Index (LAX)} = \frac{1m}{\text{number of layers per 1 meter true vertical thickness interval}}$$

The more layers in the interval the lower the anisotropy index is, the layers can be mechanically and mineralogically different as brittle and ductile couplets, but also can have similar properties, which is either all brittle or all ductile. For this case specifically, when the brittle and ductile couplets are combined as 50% from each type of layers the fractures are mostly bed bounded and behave differently in each type of layer (Becerra, 2017). This is believed to be best for shale reservoir development which seeks to reach a balance between fracturing efficiency and organic richness at the same time (Becerra, 2017).

DISCUSSION AND CONCLUSIONS

From the observations and quantification results, it is clear to conclude that the layering effect, which occurs normally in shale reservoirs has a significant impact on fractures. The interbed feature, which is inherently caused by lithofacies alteration during deposition and burial diagenesis, bring a mechanical property contrast between each cherty and organic rich clay-siliceous

stratigraphic layer. This not only causes layering anisotropy but also mechanical properties anisotropy within reservoirs and ultimately affects distribution patterns, density/intensity, and extent of deformation of fractures.

During the designed experiments, the shear and conjugate fractures are the most dominant type which is expected from the previous models. Beyond that, nine subtypes of fractures are defined to better illustrate the geometry, extent of deformation and deformation mechanism. This subcategory can be used as further reference of permeability prediction and fluid flow simulation since each can make a differential contribution to fluid flow in the subsurface. Seven deformation stages also are summarized to standardize the deformation procedure that was observed from all the tests. This helps determine the relative time of deformation and what to expect by sequences when simulating the growth of fractures/faults in a interbedded geobody.

Increasing in layers can directly increase the overall layering anisotropy and ultimately lead to higher extent of deformation and perhaps artificial fracturing. However, the fracture intensity in this case study has limited capability to fully represent the extent of deformation but is still able to capture an increasing trend of fracture intensity along with layering at small scale (0.75 and 1 cm groups). With a further increase in layer numbers, the deformation mechanism transfers from simple shear deformation towards opening deformation with fewer fracture planes but larger horizontal displacement.

In shale reservoirs, the main focus is to reach the maximum balance between efficiency of hydraulic fracturing and organic richness. For this consideration, the best scenario is to have the brittle and ductile layers combined with the same percentage of high frequency interbeds (Becerra et al., 2018). The equal distribution (50%:50%) of brittle and ductile layers can help reach a maximum of organic richness from the ductile clay rich layers but also maximize the fracability by

the same number of brittle layers at the same time. High frequency of layering, as proposed in this study is represented by a Layering Anisotropy Index (LAI), which can be observed and quantified from the image logs and cores to further enhance the efficiency of hydraulic fracturing. This phenomenon is considered as another key index when locating the fracturing sweet spots for the unconventional reservoirs.

There are some limitations of these experiments which don't represent the subsurface condition: the unconfined uniaxial setting is not perfect to simulate the situation in the confined subsurface. The materials selected in this study all have high plasticity to make it compressible with observable axial strain which is exaggerated more than normal in the diagenesis and deformation stages of the real rock; but makes the fractures more obvious to generate and observe. The disadvantages of these materials and settings are that they are not fully representative of the high stiffness rocks and the single setting of 2cm total axial strain (30% axial strain) is not applicable to all the cases. Also, the deformation regime in the real case is not necessarily pure uniaxial compression which the more complex regimes could lead to more complex fracture networks. Future study can investigate further and test more layer thickness settings and more complex stress regimes in order to better represent the real case. Numerical simulation is also another good approach to make layer settings more standardized and variable.

CHAPTER IV REFERENCES

Amann, F., E. A. Button, K. F. Evans, V. S. Gischig, and M. Blümel, 2011, Experimental study of the brittle behavior of clay shale in rapid unconfined compression: *Rock Mechanics and Rock Engineering*, v. 44, p. 415-430.

- Bai, T., and D. D. Pollard, 2000, Fracture spacing in layered rocks: a new explanation based on the stress transition: *Journal of Structural Geology*, v. 22, p. 43-57.
- Becerra, D., 2017, Integrated geological characterization at the bed scale of the Woodford Shale at the I-35 outcrop: Southern Oklahoma: MS thesis, University of Oklahoma.
- Becerra, D., H. Galvis, and R. Slatt, 2018, Characterizing the two principal rock types comprising the Woodford Shale resource play: Application to shale geomechanics: *Interpretation*, v. 6, p. SC67-SC84.
- Beckham, W. E., 1996, Seismic anisotropy and natural fractures from VSP and borehole sonic tools—A field study: *Geophysics*, v. 61, p. 456-466.
- Bobet, A., and H. Einstein, 1998, Fracture coalescence in rock-type materials under uniaxial and biaxial compression: *International Journal of Rock Mechanics and Mining Sciences*, v. 35, p. 863-888.
- Cai, M., P. Kaiser, Y. Tasaka, T. Maejima, H. Morioka, and M. Minami, 2004, Generalized crack initiation and crack damage stress thresholds of brittle rock masses near underground excavations: *International Journal of Rock Mechanics and Mining Sciences*, v. 41, p. 833-847.
- Cant, D. J., 1980, Storm-dominated shallow marine sediments of the Arisaig Group (Silurian–Devonian) of Nova Scotia: *Canadian Journal of Earth Sciences*, v. 17, p. 120-131.
- Convers, C., 2017, Prediction of reservoir properties for geomechanical analysis using 3-D seismic data and rock physics modeling in the Vaca Muerta Formation, Neuquén Basin, Argentina: Ph.D. Dissertation thesis, Colorado School of Mines. Arthur Lakes Library.

- Courtillot, V., P. Tapponnier, and J. Varet, 1974, Surface features associated with transform faults: a comparison between observed examples and an experimental model: *Tectonophysics*, v. 24, p. 317-329.
- Dershowitz, W. S., and H. H. Herda, 1992, Interpretation of fracture spacing and intensity: The 33th US Symposium on Rock Mechanics (USRMS).
- Dewhurst, D. N., and A. F. Siggins, 2006, Impact of fabric, microcracks and stress field on shale anisotropy: *Geophysical Journal International*, v. 165, p. 135-148.
- Dooley, T. P., and G. Schreurs, 2012, Analogue modelling of intraplate strike-slip tectonics: A review and new experimental results: *Tectonophysics*, v. 574, p. 1-71.
- Esmersoy, C., K. Koster, M. Williams, A. Boyd, and M. Kane, 1994, Dipole shear anisotropy logging, SEG Technical Program Expanded Abstracts 1994, Society of Exploration Geophysicists, p. 1139-1142.
- Fakhimi, A., and B. Hemami, 2017, Rock uniaxial compression test and axial splitting: *Procedia engineering*, v. 191, p. 623-630.
- Gale, J. F., S. E. Laubach, J. E. Olson, P. Eichhubl, and A. Fall, 2014, Natural fractures in shale: A review and new observations *Natural Fractures in Shale: A Review and New Observations: AAPG bulletin*, v. 98, p. 2165-2216.
- Gross, M. R., M. P. Fischer, T. Engelder, and R. J. Greenfield, 1995, Factors controlling joint spacing in interbedded sedimentary rocks: integrating numerical models with field observations from the Monterey Formation, USA: Geological Society, London, Special Publications, v. 92, p. 215-233.
- Hatchell, P. J., G. S. De, D. F. Winterstein, and D. C. DeMartini, 1995, Quantitative comparison between a dipole log and VSP in anisotropic rocks from Cymric oil field, California, SEG

- Technical Program Expanded Abstracts 1995, Society of Exploration Geophysicists, p. 13-16.
- Helbig, K., and L. Thomsen, 2005, 75-plus years of anisotropy in exploration and reservoir seismics: A historical review of concepts and methods: *Geophysics*, v. 70, p. 9-23.
- Hempton, M. R., and K. Neher, 1986, Experimental fracture, strain and subsidence patterns over an echelon strike-slip faults: implications for the structural evolution of pull-apart basins: *Journal of Structural Geology*, v. 8, p. 597-605.
- Higgins, S. M., S. A. Goodwin, T. R. Bratton, and G. W. Tracy, 2008, Anisotropic stress models improve completion design in the Baxter Shale: SPE Annual Technical Conference and Exhibition.
- Ingall, E. D., R. Bustin, and P. Van Cappellen, 1993, Influence of water column anoxia on the burial and preservation of carbon and phosphorus in marine shales: *Geochimica et Cosmochimica Acta*, v. 57, p. 303-316.
- Jamison, W. R., 1991, Kinematics of compressional fold development in convergent wrench terranes: *Tectonophysics*, v. 190, p. 209-232.
- Johnston, J. E., and N. I. Christensen, 1995, Seismic anisotropy of shales: *Journal of Geophysical Research: Solid Earth*, v. 100, p. 5991-6003.
- Jones, L. E., and H. F. Wang, 1981, Ultrasonic velocities in Cretaceous shales from the Williston basin: *Geophysics*, v. 46, p. 288-297.
- Ladeira, F., and N. Price, 1981, Relationship between fracture spacing and bed thickness: *Journal of Structural Geology*, v. 3, p. 179-183.
- Lowell, J. D., 1972, Spitsbergen Tertiary orogenic belt and the Spitsbergen fracture zone: *Geological Society of America Bulletin*, v. 83, p. 3091-3102.

- McClay, K., and T. Dooley, 1995, Analogue models of pull-apart basins: *Geology*, v. 23, p. 711-714.
- Mitra, S., and Q. T. Islam, 1994, Experimental (clay) models of inversion structures: *Tectonophysics*, v. 230, p. 211-222.
- Narr, W., 1996, Estimating average fracture spacing in subsurface rock: *AAPG bulletin*, v. 80, p. 1565-1585.
- Pasley, M. A., W. A. Gregory, and G. F. Hart, 1991, Organic matter variations in transgressive and regressive shales: *Organic geochemistry*, v. 17, p. 483-509.
- Peacock, D., and D. Sanderson, 1992, Effects of layering and anisotropy on fault geometry: *Journal of the Geological Society*, v. 149, p. 793-802.
- Pratt, L. M., G. E. Claypool, and J. D. King, 1986, Geochemical imprint of depositional conditions on organic matter in laminated—Bioturbated interbeds from fine-grained marine sequences: *Marine Geology*, v. 70, p. 67-84.
- Reches, Z., 1988, Evolution of fault patterns in clay experiments: *Tectonophysics*, v. 145, p. 141-156.
- Reches, Z. e., 1987, Mechanical aspects of pull-apart basins and push-up swells with applications to the Dead Sea transform: *Tectonophysics*, v. 141, p. 75-88.
- Reches, Z. e., and A. Eidelman, 1995, Drag along faults: *Tectonophysics*, v. 247, p. 145-156.
- Sahouryeh, E., A. Dyskin, and L. Germanovich, 2002, Crack growth under biaxial compression: *Engineering Fracture Mechanics*, v. 69, p. 2187-2198.
- Sayers, C., 2005, Seismic anisotropy of shales: *Geophysical prospecting*, v. 53, p. 667-676.
- Sayers, C. M., 2013, The effect of kerogen on the elastic anisotropy of organic-rich shales: *Geophysics*, v. 78, p. D65-D74.

- Sierra, R., M. Tran, Y. Abousleiman, and R. Slatt, 2010, Woodford shale mechanical properties and the impacts of lithofacies: 44th US rock mechanics symposium and 5th US-Canada rock mechanics symposium.
- Slatt, R. M., and Y. Abousleiman, 2011, Merging sequence stratigraphy and geomechanics for unconventional gas shales: *The Leading Edge*, v. 30, p. 274-282.
- Sone, H., and M. D. Zoback, 2013, Mechanical properties of shale-gas reservoir rocks—Part 1: Static and dynamic elastic properties and anisotropy: *Geophysics*, v. 78, p. D381-D392.
- Sylvester, A. G., and R. R. Smith, 1976, Tectonic transpression and basement-controlled deformation in San Andreas fault zone, Salton Trough, California: *AAPG Bulletin*, v. 60, p. 2081-2102.
- Tariq, S. M., M. Ichara, and L. Ayestaran, 1989, Performance of perforated completions in the presence of anisotropy, laminations, or natural fractures: *SPE Production Engineering*, v. 4, p. 376-384.
- Varacchi, B. H., 2011, Rock physics and mechanical stratigraphy of the Woodford Shale, Anadarko Basin, Oklahoma: Master's thesis, Oklahoma State University, 36 p.
- Vernik, L., and X. Liu, 1997, Velocity anisotropy in shales: A petrophysical study: *Geophysics*, v. 62, p. 521-532.
- Wang, Z., 2002, Seismic anisotropy in sedimentary rocks, part 2: Laboratory data: *Geophysics*, v. 67, p. 1423-1440.
- Wheeler, D. M., A. J. Scott, V. J. Coringrato, and P. E. Devine, 1990, Stratigraphy and depositional history of the Morrow Formation, southeast Colorado and southwest Kansas.
- Withjack, M. O., Q. T. Islam, and P. R. La Pointe, 1995, Normal faults and their hanging-wall deformation: an experimental study: *AAPG bulletin*, v. 79, p. 1-17.

- Withjack, M. O., and R. W. Schlische, 2006, Geometric and experimental models of extensional fault-bend folds: Geological Society, London, Special Publications, v. 253, p. 285-305.
- Withjack, M. O., R. W. Schlische, and A. A. Henza, 2007, Scaled experimental models of extension: dry sand vs. wet clay.
- Zhang, J., B. Turner, and R. Slatt, 2017, XRF Chemostratigraphy for Characterizing Shale Reservoir along a Horizontal Well Track, AAPG 2016 Annual Convention and Exhibition,, Calgary, Alberta, Canada.
- Zhang, J., Y. Zeng, and R. Slatt, 2019, XRF (X-ray fluorescence) applied to characterization of unconventional Woodford Shale (Devonian, USA) lateral well heterogeneity: Fuel, v. 254, p. 115565.
- Zoback, M. D., 2010, Reservoir geomechanics, Cambridge University Press.

CHAPTER V

**AZIMUTHAL SEISMIC ANISOTROPY ANALYSIS APPLIED TO
NATURALLY FRACTURED UNCONVENTIONAL RESERVOIRS:
BARNETT SHALE EXAMPLE**

*This manuscript has been submitted to Interpretation

ABSTRACT

Studying seismic responses of velocity and amplitude on wide/full azimuth seismic data is now common for unconventional reservoir characterization. The velocity variation with azimuth (VVAz) and amplitude variation with azimuth (VAz) are two of the most popular tools to map not only the relative intensity and orientation of natural fractures but also the strength and orientation of the maximum horizontal stress S_H . We migrated a wide-azimuth Barnett Shale survey in north Texas into eight azimuths and reduced noise on the gathers using prestack structure-oriented filtering. We then computed the envelope, spectral peak frequency, and prestack P-wave impedance attributes for each azimuthally-limited seismic volume. We compensated VVAz effects by flattening each sector along the Barnett Shale key horizons, thereby registering the gathers for subsequent VAz analysis. The results indicate intensity, orientation, and confidence of azimuthal anisotropy effects on seismic velocity and amplitude which can be referred to smaller scale vertical cracks or natural fractures.

Our analysis reveals four zones of high anisotropy intensity that can be tied to either the regional structures or paleo stress field. Analysis of production data indicate that the anisotropy interpretation indicates that vertical, sealed fractures are the dominant cause of anisotropy and those specific fractures inhibit production. This observation and results indicate that horizon-based

azimuthal anisotropy analysis avoids the VVAz effect and can be applied to fractures and regional stress field prediction.

INTRODUCTION

The strike orientation of open microcracks, which represents the present-day stress field, plays a key role in allocating and developing shale resource plays. Our goal is to determine if the anisotropy obtained from AVAz analysis of a wide azimuth survey can be quantitatively correlated to natural fracture distribution. Residual moveout analysis indicates that the Barnett Shale reservoir exhibits moderate Horizontal Transverse Isotropy (HTI) and relatively weak layering induced Vertical Transverse Isotropy (VTI). The moderate intensity of azimuthal anisotropy allows us to use Thomsen (1986) anisotropy analysis. We assume that the main cause of azimuthal anisotropy in the survey is attributed to microcracks that are open perpendicular to the minimum horizontal stress.

The existence of natural fractures or discontinuities in the subsurface are known to influence both travel times and amplitudes of seismic waves (Anderson et al., 1974; Kuster and Toksöz, 1974; Boadu, 1995; Boadu and Long, 1996). When clustered fractures are near vertical and maintain a consistent strike direction, the medium will exhibit Horizontal Transverse Isotropy (HTI) (Wang, 2002; Helbig and Thomsen, 2005; Tsvankin and Grechka, 2011; Liu, 2013; Alali, 2018). Seismic P wave propagation will be affected when passing through the HTI medium with a corresponding azimuthal variation: 1) A slowed P-wave velocity with the maximum velocity attenuation orthogonal to the fracture plane (fracture strike orientation) and a faster P-wave velocity along the fracture plane (fracture strike orientation) (Anderson et al., 1974; Kuster and Toksöz, 1974; Boadu, 1995; Clifford et al., 2005). This variation results in different arrival times and reflection coefficients for source-receiver on different azimuths. 2) P-wave amplitude

attenuation due to scattering with maximum extent when perpendicular to the fracture strike direction which can be reflected as amplitude and other amplitude related seismic attributes attenuation (Maultzsch et al., 2007; Thompson et al., 2010). The amplitude attenuation can be observed from different azimuths and offsets (Samec and Blangy, 1992; Zhu et al., 2007) (Figure 5.1).

Amplitude variation with azimuth (AVAz) of azimuthally sectored migrated seismic data provides a means to map both the intensity and orientation of HTI medium anisotropy (Gray and Head, 2000; Rüger, 2002; Gray et al., 2003; Gray, 2008; Mahmoudian et al., 2013; Liu, 2014; Qi et al., 2015; Wang et al., 2015). AVAz analysis requires the acquisition of wide/ full azimuth seismic data with sufficient offsets (Rüger, 2002). Thompson et al. (2010) show how one can calculate the intensity (ϵ), azimuth (Ψ) and confidence (c) of these measures by fitting an ellipse to the different azimuth volumes in each gather for HTI media.

For this case study, we began with conducting seismic interpretation on eight azimuthal gathers from one wide azimuth survey and then we calculated the amplitude related seismic attributes for each azimuthal gather, next we flattened the attribute based on seismic key horizons from interpretation and input into AVAz workflow to obtain the key parameters of anisotropy. We conclude the relationship between natural fractures distribution and seismic azimuthal anisotropy by comparing with the gas production map in the study area.

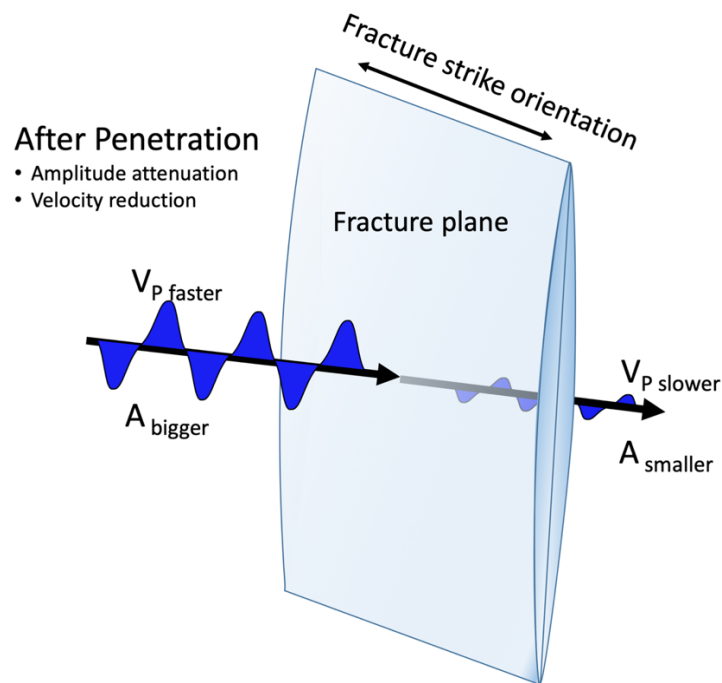


Figure 5.1: Seismic wave amplitude and velocity attenuation when penetrates perpendicular to the fracture strike direction.

GEOLOGIC BACKGROUND

This case study targets the Barnett Shale in the Fort Worth Basin, north Texas, USA (Figure 5.2). The Mississippian age Barnett Shale is an organic-rich shale gas reservoirs exploited in North America (Singh et al., 2008). The Fort Worth Basin is a foreland basin formed during the late Paleozoic due to the Ouachita orogeny (Walper, 1981; Thompson, 1988). The basin is bounded by the Red River Arch and Muenster Arch in the North, the Ouachita Thrust-Fold Belt in the east, the Llano Uplift paleo-high in the south and the Bend Arch in the west. Within the basin, the major Mineral Wells Fault is oriented in a northeast-southwest direction (Pollastro et al., 2007) (Figure 5.2).

Before deposition of the Barnett Shale, the Ellenburger Group carbonates formed a broad epicontinental platform and later underwent subaerial erosion and karsting, which formed an unconformity on the Ellenberger and Viola limestone surfaces (Kerans, 1988; Gasparrini et al.,

2014). The Barnett Shale was deposited on top of this unconformity during the transition from the uplifted area to a foreland basin (Henry, 1982; McBee Jr, 1999). The Barnett Shale formation is subdivided into the Upper and Lower members. The Forestburg Limestone occurs between the two members regionally in the northeast part of the basin where our survey lies and pinches out toward the south (Henry, 1982; Bowker, 2003; Montgomery et al., 2005; Gasparri et al., 2014). Generally, the thickness of the Barnett varies from 380 ft in the southern part of the basin (Bend Arch and Llano Uplift area) up to 4300 ft thick in the northern part (Muenster Arch area) (Montgomery et al., 2005). Ten lithofacies of the Barnett Shale were identified by Abouelresh and Slatt (2012) from a core in Johnson County based on composition and sedimentary structures to represent the general geological characteristics of the Barnett Shale.

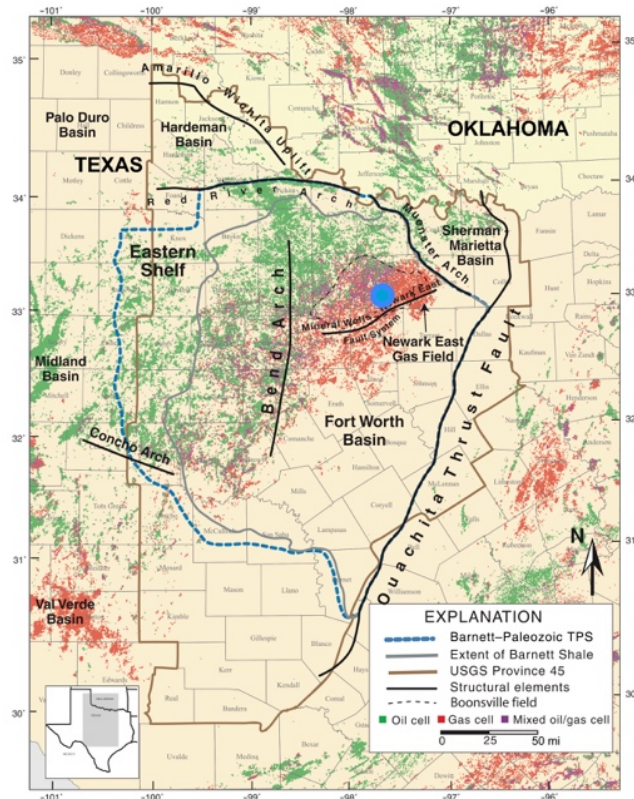


Figure 5.2: Major structural features of the Fort Worth Basin and production type distribution (Pollastro et al., 2007). The location of the case study area is highlighted with the blue dot.

BASIN STRUCTURAL SETTINGS AND FRACTURES

The natural fractures in the Barnett Shale have been documented in many studies especially in the Fort Worth Basin. Gasparrini et al. (2014) conducted petrographic analyses of sealed natural fractures from cores and outcrops and identified four episodes of fracture generation, representing different compaction conditions, thermal regimes and times. Bowker (2007) indicated that the overpressure within the Barnett Shale proves that open natural fractures are rare. Commercial oil and gas companies found that the natural fracture density increases adjacent to fault zones. However, most of the fractures are sealed with carbonate cement which reduces the reservoir porosity and provides little contribution to fluid flow during production (Bowker, 2003; Bowker, 2007; Gale et al., 2008). Gale et al. (2007) reported that most sealed natural fractures are likely clustered with at least two sets of orientation: the older north-south trending sets and the younger west-northwest-east-southeast trending set. The current day stress field near the study area has a maximum horizontal stress orientation of northeast-southwest (Lund Snee and Zoback, 2016) (Figure 5.3). Seismic attributes and karst collapse analysis have also been applied to the region for structural interpretation,. Trumbo (2014) analyzed seismic curvature volumes and found that microseismic events caused by hydraulic fracturing clustered in bowl shaped areas but avoided ridge shaped features suggesting that natural fractures in the ridges were more difficult to stimulate.

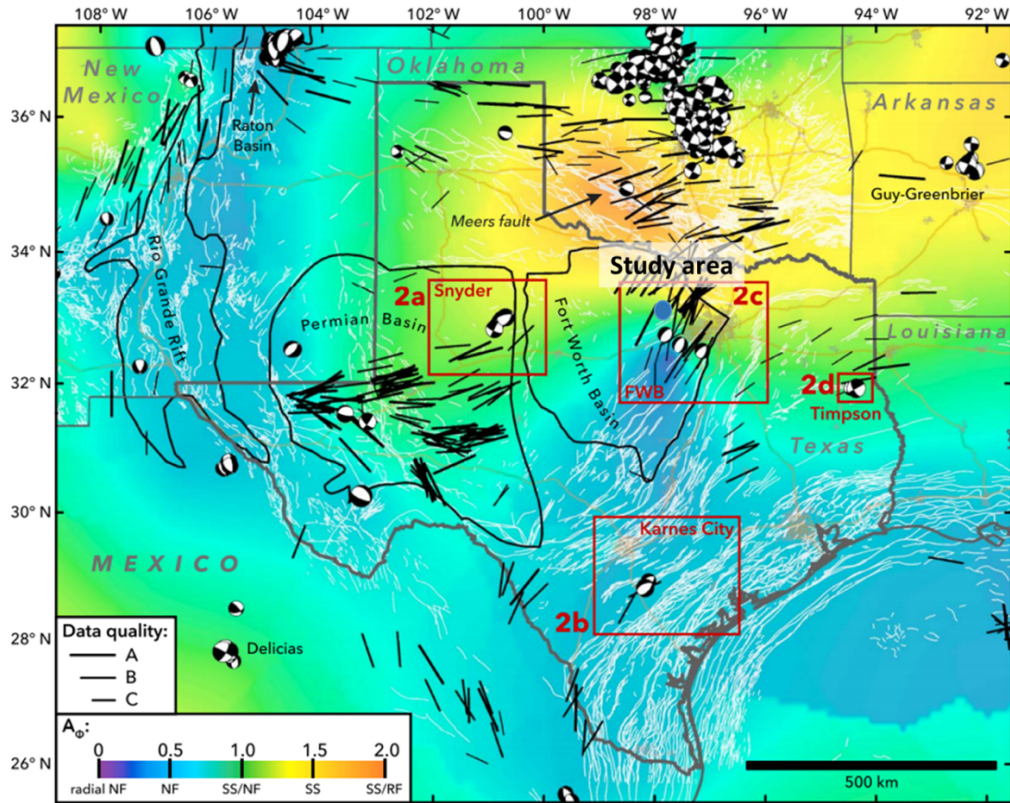


Figure 5.3: Stress map of Texas showing the maximum horizontal stress orientation (Lund Snee and Zoback, 2016). The study area is highlighted in the blue circle, the FWB represents the Fort Worth Basin and indicates that the current day maximum horizontal stress is trending northeast-southwest, the colors indicate that the study area locates within a strike slip fault and normal fault transition regime.

REGIONAL STRUCTURAL ANALYSIS

The 3D seismic survey falls within the Newark East Field, Wise County, TX. In this area the Barnett Shale is about 500 ft thick with about 100 ft thick Forestburg Lime contained in the middle of the formation. The average Barnett burial depth is around 5000 ft and mainly produces gas (Figure 5.2). Two major normal faults (named Fault A and Fault B in Figure 4) are striking northeast-southwest and dipping towards the northwest as can be visualized on stratal slices within the Barnett Shale using coherence and curvature seismic attributes (Figure 5.4). Although strike slip motion is difficult to capture on seismic, the regional stress map by Lund Snee and Zoback (2016) (Figure 5.3) indicates that strike slip deformations are involved with the normal fault

displacement. Fault A and Fault B are slightly curved in the northern end and fault planes are compartmentalized according to the coherence attribute. The compartmentalization can be interpreted due to the strike slip shear movement in a thrust fold transfer zone. According to the seismic interpretation and published literature (Adams, 2003; Montgomery et al., 2005; Pollastro et al., 2007), these two normal faults belong to the Mineral Wells Fault system and share the same deformation mechanism. The faults originate from the basement and stop growing at the top of the Barnett Shale indicating that the general deformation stopped by late Mississippian time (Baruch et al., 2009).

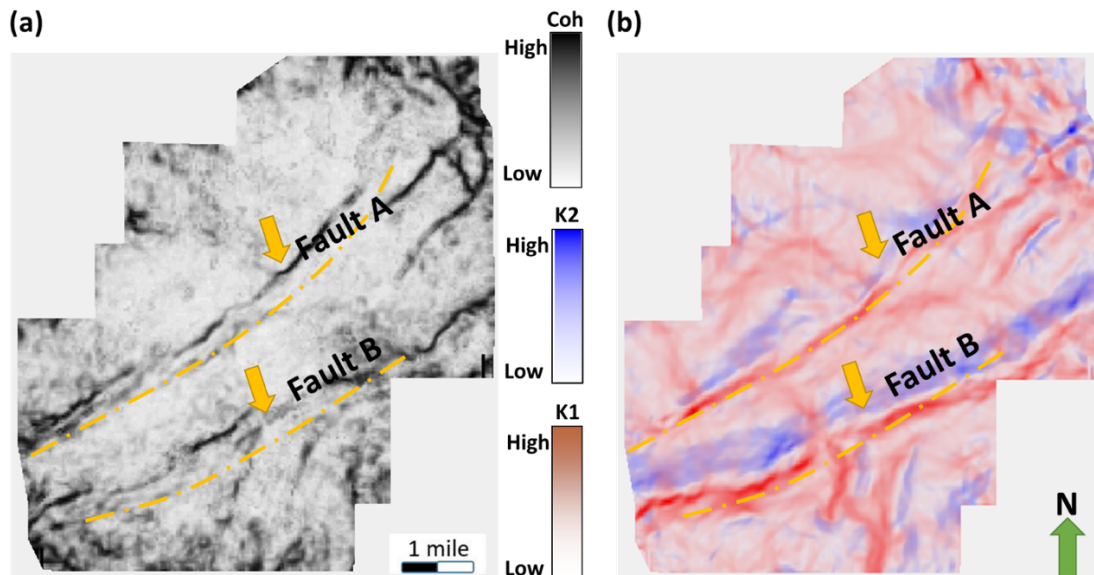


Figure 5.4: Strata slice (Base Barnett) through (a) coherence, and (b) most positive and negative curvature co-render maps. Two major normal faults (Fault A, Fault B) are delineated by the orange dashed lines, both of which are subparallel to the Mineral Wells Fault (not included in the survey).

The average strike of Faults A and B were measured along the fault line based on a stratal slice along the Base Barnett/ Top Viola in coherence and curvature attributes; generally, Fault A has an average strike orientation of 47° and Fault B has an average strike orientation of 62° (Table 5.1).

Table 3: Strike measurement on Fault A and B from the Base Barnett strata slice of coherence and most positive curvature attributes.

Measurement	1	2	3	4	5	6	7	8	9	10	11	Avg
Fault A	48	48	46	47	53	23	43	37	53	56	67	47
Fault B	63	70	62	49	65	63	52	57	71	64	69	62

Since Faults A and B are in a normal/ lateral strike slip regime, σ_1 is vertical, σ_2 (S_{Hmax}) was in a northeast-southwest trend parallel to Fault A and B's strike orientations. σ_3 (S_{hmin}) is perpendicular to the σ_2 (S_{Hmax}) (Figure 5). In such a combined fault regime σ_1 (S_v) = σ_2 (S_{Hmax}) > σ_3 (S_{hmin}), which indicates the magnitude of vertical stress could be slightly larger or similar to the maximum horizontal stress. As a result, vertical natural fractures formed together with deformation of the faults following the general orientation of strike along S_{Hmax} , and expected an increase in density adjacent to the fault plane. However, smaller scale fracture orientations could vary and be complex.

METHODOLOGY

In 2006, Devon Energy acquired a wide azimuth prestack seismic survey (before hydraulic fracturing), which we reprocessed into eight azimuthally-limited gather volumes (Figure 5.6). Our workflow is an expansion of the one used by Zhang et al. (2013) and Guo et al. (2016) (Figure 5.7). We first corrected for the velocity variation with azimuth (VVAz) effect by manually picking four key geologic horizons Top Barnett (TB), Base Upper Barnett (BUB), Top Lower Barnett (TLB) and Base Barnett (BB) on each azimuthally limited volume (Figure 5.8). Examining Figure 5.9, note that azimuths 6 and 7 have the weakest seismic amplitude whereas azimuths 3 and 4 have the strongest amplitude. Arrival time differences between the four key horizons provided the indication of the VVAz effect. In addition to amplitude variation with azimuth, we also examined

variation in seismic attributes including envelope, spectral peak frequency and prestack P-impedance. The final output is the ϵ (intensity of anisotropy), Ψ (azimuth of largest attribute value) and c (confidence of least square fit) along the interpreted horizons for each of these attributes on each azimuth. Among those outputs, Ψ (azimuth of minimum variation) can be used to represent fracture strike orientation in a HTI medium.

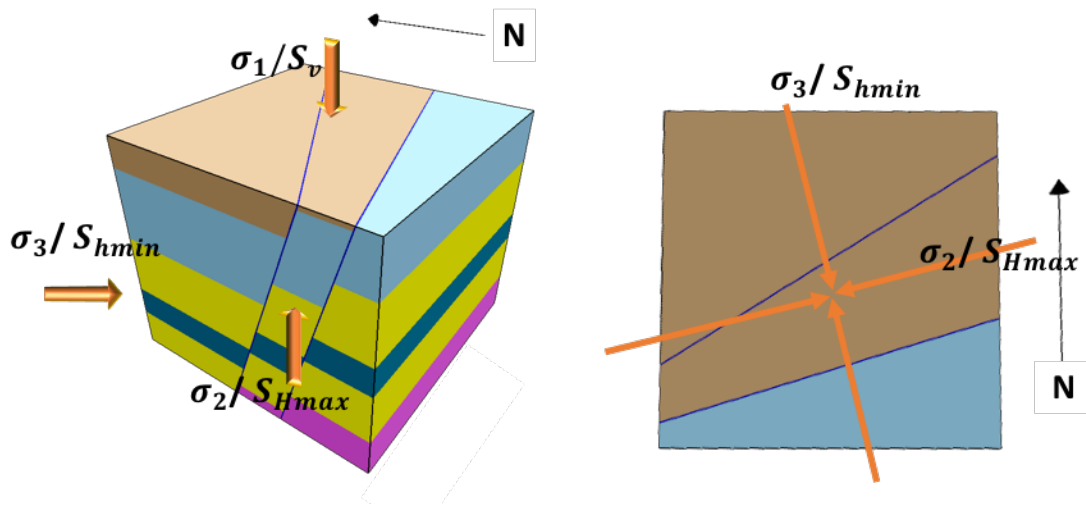


Figure 5.5: The regional stress field interpretation is based on observed structures and the regional fault. The maximum horizontal stress follows orientation parallel to the strike of Faults A and B. The local stress field and structure cannot be simply represented by the regional stress field.

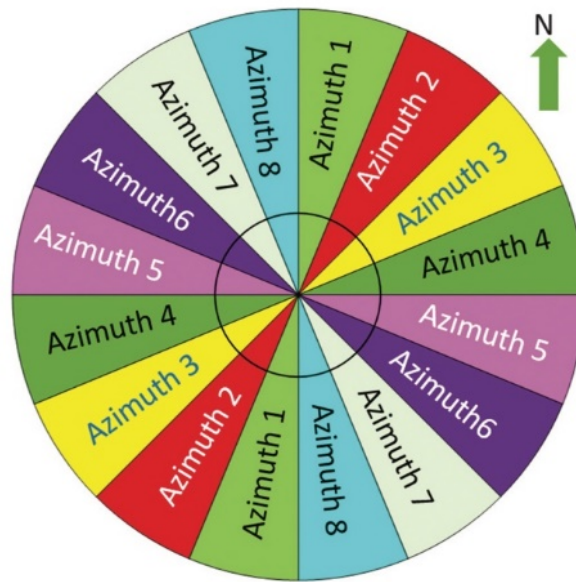


Figure 5.6: Eight different azimuthal bins covering the full azimuth range with 22.5° increment using the method proposed by (Perez and Marfurt, 2007)

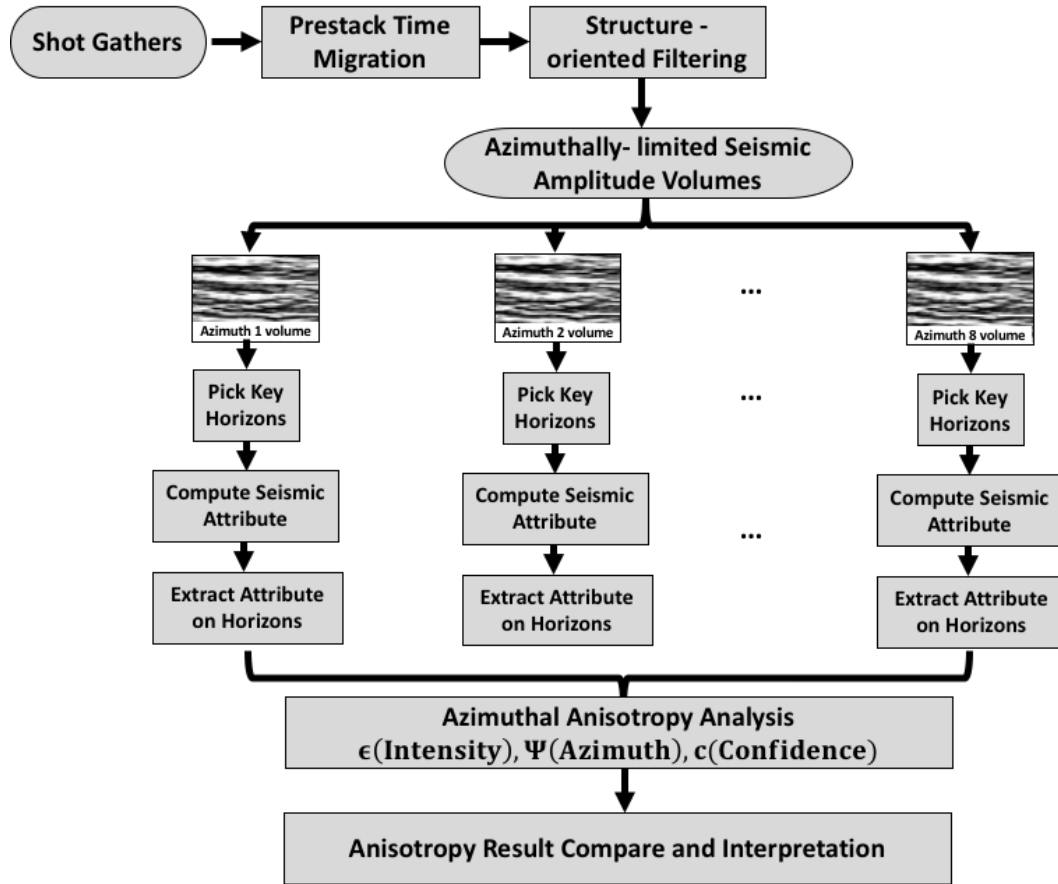


Figure 5.7: Workflow for azimuthal anisotropy analysis and interpretation. Data should be preprocessed and then the target horizons are interpreted manually for each azimuthal volume in order to compensate for the velocity anisotropy effect. Extracted attributes along key horizons were input for anisotropy analysis respectively. The output includes three key parameters of anisotropy: intensity, azimuth and confidence.

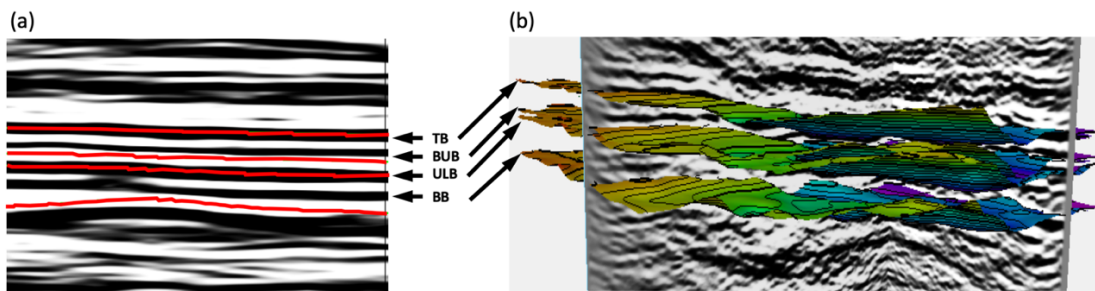


Figure 5.8: Four key formation top horizons picked in the seismic survey. (a) Inline view showing the thickness relationship of the Upper Barnett, Lower Barnett and Forestburg Lime. (b) Four interpreted horizons in 3D view. For each azimuthal volume, the horizons were picked separately.

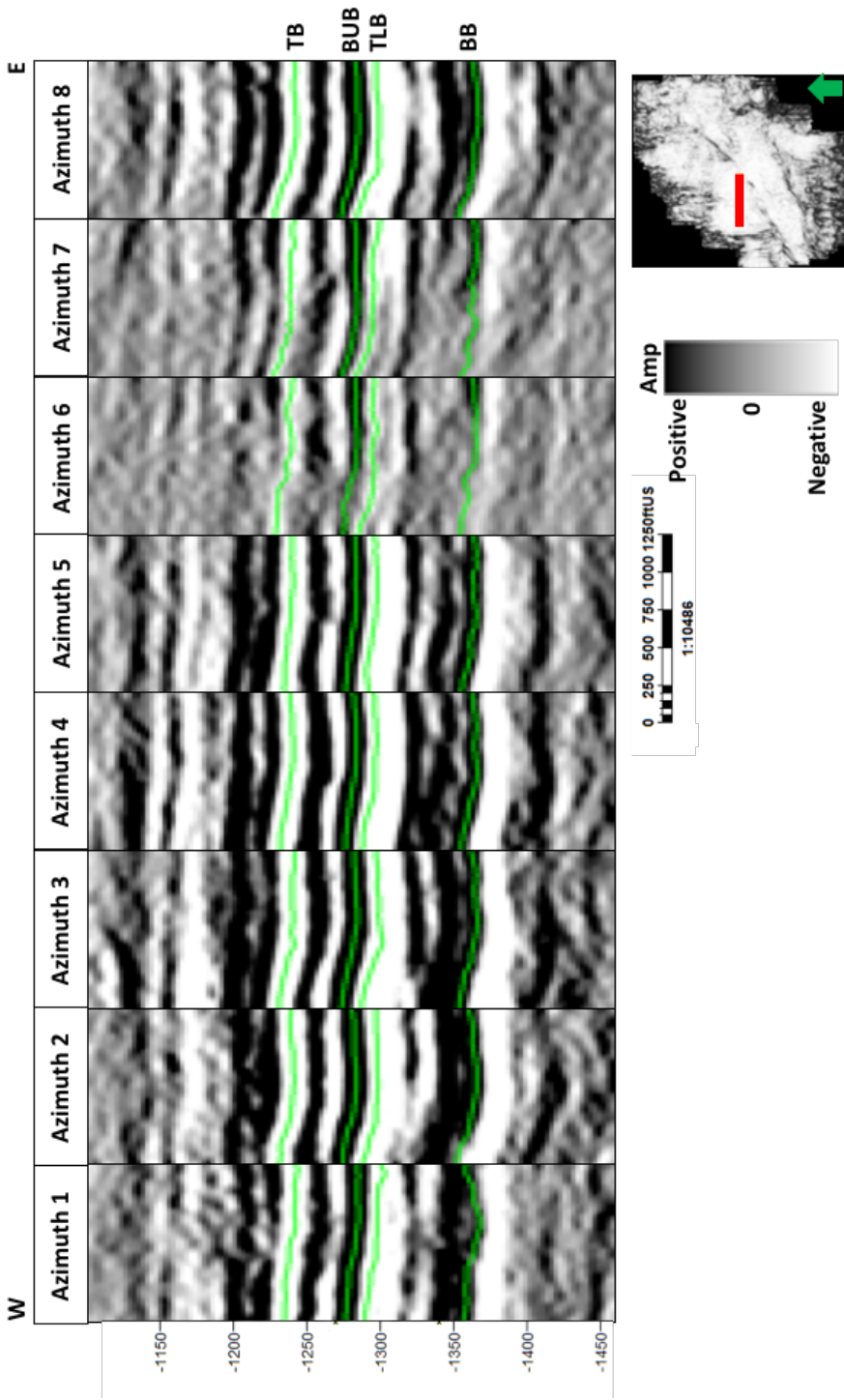


Figure 5.9: azimuthal seismic volumes comparison from the cross section obtained from the northwest part of the study area. The color code represents magnitude of amplitude. Note that amplitude varies by azimuthal volume and the arrival time of four key horizons that are highlighted in green are different after manually interpreting the horizons. The interpretation uses 2D seed picking for each volume and QC manually afterward to avoid any manually picking error.

ATTRIBUTES FOR ANISOTROPY ANALYSIS

We selected several amplitude- and velocity-related seismic attributes in addition to the amplitude itself to conduct anisotropy analysis. Attribute volumes on each azimuthal gather were calculated and then extracted along the key horizons interpreted from that corresponding azimuthal gather to input in anisotropy analysis. All the attributes are expected to reflect the anisotropy effect along the extracted horizons and compared to support the final conclusions.

Envelope (also called “reflection strength” or “amplitude envelope”) is often used to determine lateral variation in reservoirs. It calculates the absolute value of the complex trace magnitude (White, 1991; Chen and Sidney, 1997; Russell et al., 1997; Taner, 2001; Chopra and Marfurt, 2007) The magnitude of the trace envelope attribute is proportional to the acoustic impedance contrast (Russell et al., 1997; Taner, 2001) and is mathematically described as:

$$e(t) = [u^2(t) + u^{H^2}(t)]^{1/2} \quad (1)$$

where $e(t)$ is the amplitude envelope, $u(t)$ is the seismic trace, and $u^H(t)$ is its Hilbert transform trace (Taner and Sheriff, 1977; Russell et al., 1997). Envelope is directly related to the reflectivity and thus can be used as an input for anisotropy analysis.

Spectral peak frequency was calculated as one output of spectral decomposition analysis by least-squares fitting using a complex matching pursuit method (Liu and Marfurt, 2007). Peak frequency represents the spectral frequency that corresponds to the greatest spectra magnitude. Seismic waves amplitude become attenuated exponentially with time and depth when traveling in the subsurface; this amplitude attenuation effect especially affects the high frequency spectrum (Li et al., 2015; Li et al., 2016). Quantifying amplitude attenuation from seismic spectral frequency band is commonly applied to various subsurface characteristics such as rock properties, anisotropy and structures (Schoenberg and Douma, 1988; Lynn and Beckham, 1998; MacBeth, 1999; Carcione,

2000; Clark et al., 2009; Li et al., 2015). Maultzsch et al. (2007) and Wang et al. (2015) indicated that high frequency seismic components attenuated more rapidly than low frequency components and seismic amplitude attenuation increases with frequency. Higher frequency variation can be used to indicate higher extent of amplitude attenuation and then indirectly refers to higher anisotropy in the HTI medium. Thus, the AVAz outputs from spectral peak frequency attribute can be used to infer intensity of anisotropy, however azimuth outputs are in orthogonal relationship with amplitude related attributes since the azimuth of largest spectral peak frequency represents the highest amplitude attenuation orientation which is perpendicular to the fracture strike orientation and other amplitude AVAz azimuth output.

Pre stack P-wave impedance is obtained by integrating P wave, S wave velocity and bulk density logs from five wells located within the seismic survey. Impedance is an ideal property to represent azimuthal velocity and amplitude variation and attenuation for anisotropy analysis. Thompson (2010) applied prestack inversion analysis to detect induced fractures in the Barnett Shale. The prestack P-wave impedance is calculated from the far offset gathers since those gathers are more sensitive to minor anisotropy effects (Lynn and Beckham, 1998; Maultzsch et al., 2007). We limited our analysis to 25°-35° angle to represent far offset gathers. Well log time to depth correlation was conducted on all five wells based on the interpreted formation top and base from each azimuthal post stack seismic volume (Figure 5.10). A good correlation chart between the inverted P-wave impedance with the log P-wave impedance for each azimuth inversion result indicates a reliable input for anisotropy analysis (Figure 5.11). Phantom horizons were generated as close as possible to the original interpreted horizons (10ms below Top Barnett) and (15 ms below Top Lower Barnett) for each azimuth to guarantee the attribute flatten input maintain the

stable, representative interval inversion properties that are comparable with the other anisotropy analysis input attributes (Figure 5.12).

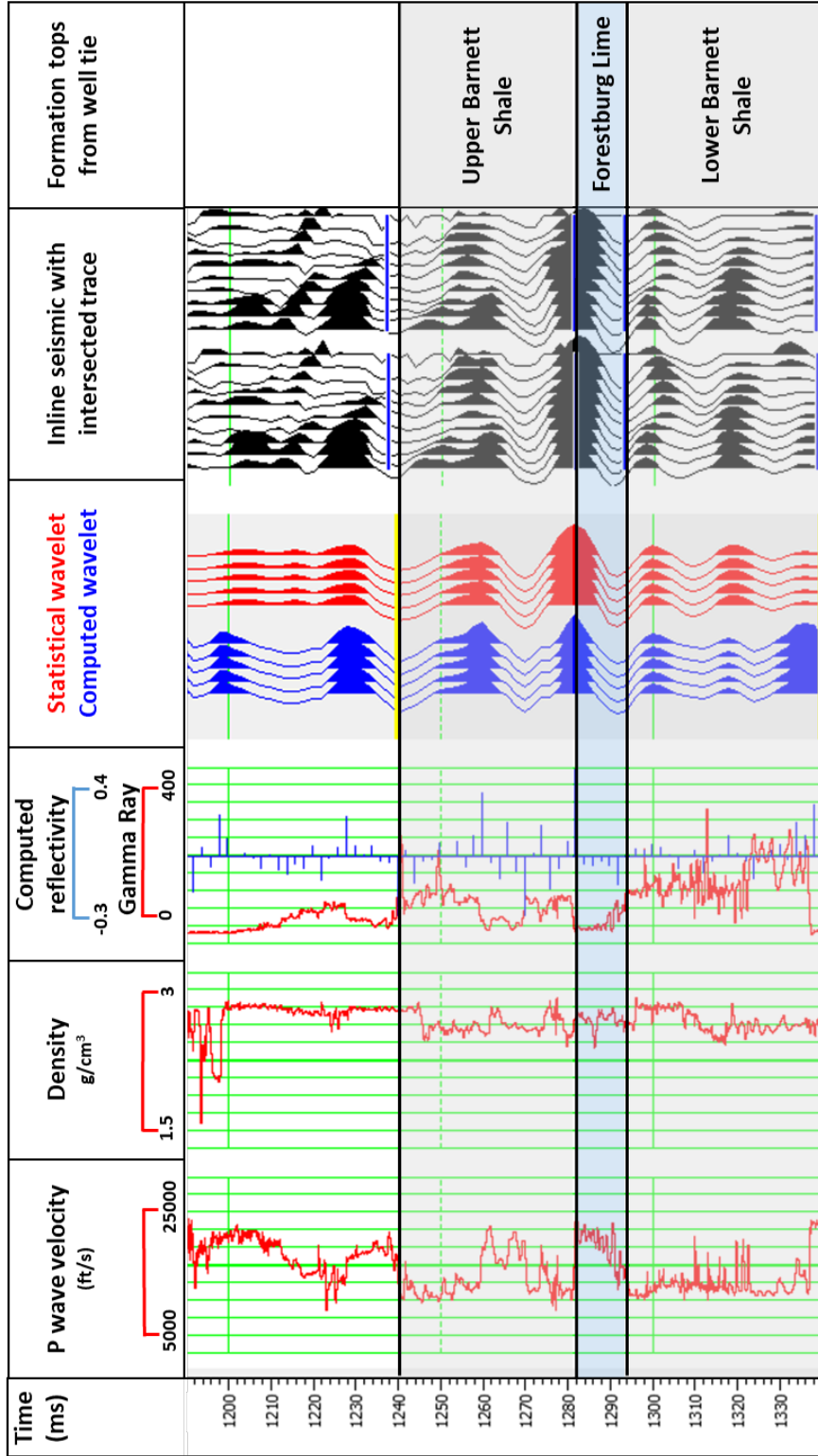


Figure 5.10: Seismic impedance calculation and well tie procedure. Because of anisotropy and acquisition parameters, the effective seismic wavelet for each azimuthal sector is slightly different. We therefore generated well ties for each volume. Note that the Forestburg Lime can be easily identified from the low gamma ray log as well as the density contrast which leads to an increase in impedance and velocity within the Forestburg. The seismic section is the well intersected inline and the gray filled trace is the specific intersected trace. The diagram shows the result after well tie and matched wells with velocity profile and interpreted seismic horizons.

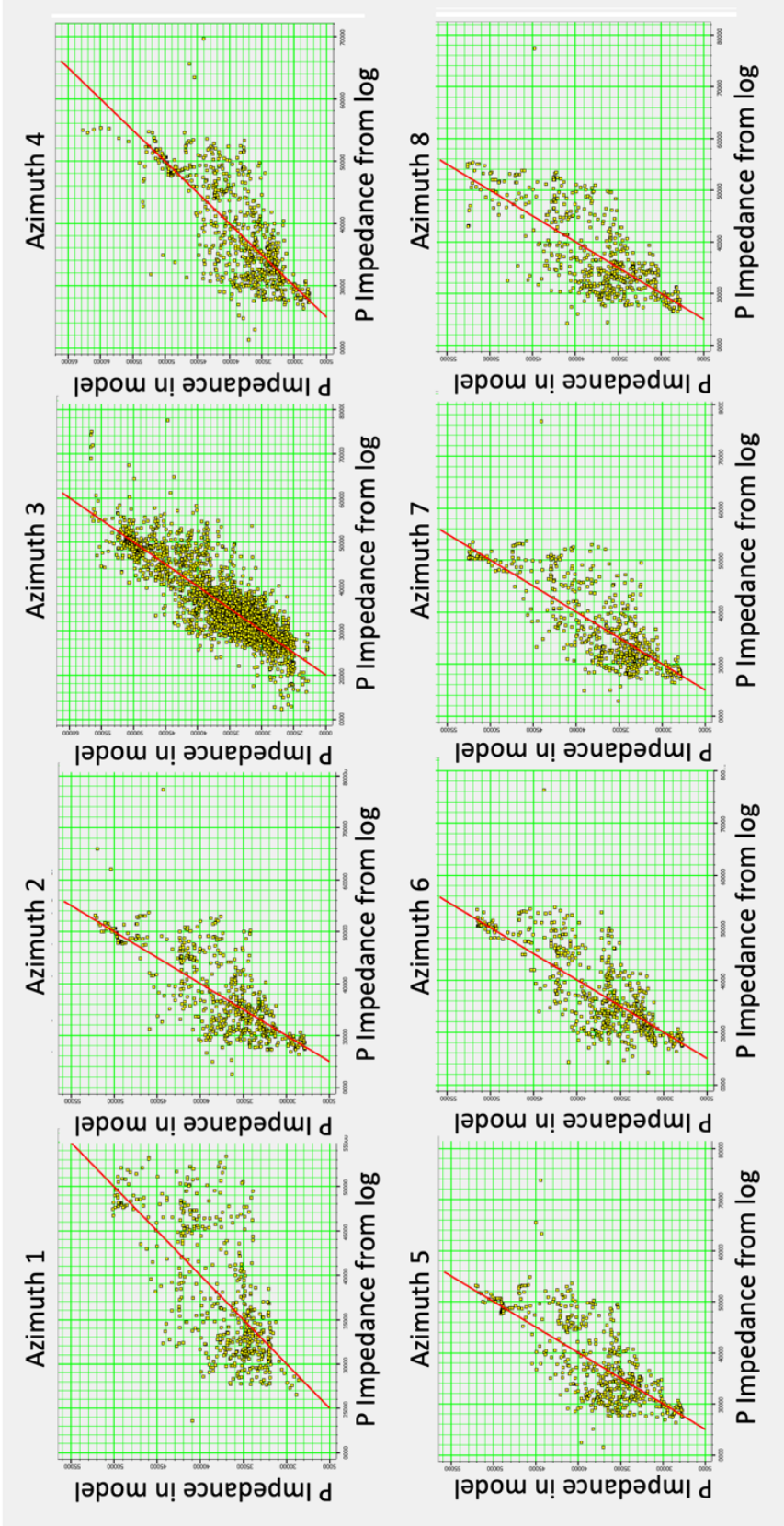


Figure 5.11: P wave impedance results from model and log cross plot shows a reliable correlation of the calculation result on each azimuth, confirming the reliability for further anisotropy calculations.

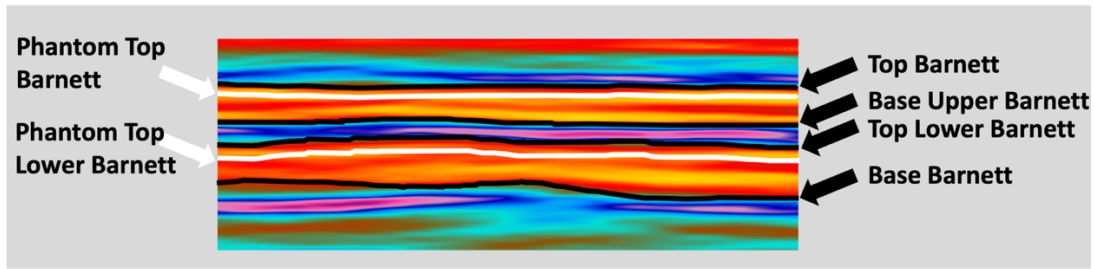


Figure 5.12: Azimuth 1 derived vertical slice through P-wave impedance with phantom horizons for the top upper Barnett and top lower Barnett that are highlighted on the left side of the impedance volume with the white arrows, regular horizons that are highlighted on the right with the black arrows. Note that the impedance value at the regular horizons have sharp changes and cannot be used to represent the interval property.

RESULTS

Anisotropy analysis was conducted on all seismic attributes and the results show a consistent location of high anisotropy intensity zones and interpreted fracture strike azimuth. The confidence of the highlighted anisotropy zone is high which excludes the possibility that the anisotropy is induced by noise and seismic processing. The results of each anisotropy attribute analysis are introduced below.

AMPLITUDE VARIATION WITH AZIMUTH

AVAz highlights four areas with high anisotropy intensity indicated as A, B, C and D respectively on Figure 5.13. These high anisotropy intensity zones are all located within the area with low coherence which indicates the topographic discontinuity is negligible for natural fractures and make it hard to be captured by regular seismic coherence attributes. The high anisotropy zones are close to fault areas which supports the assumption that smaller scale deformations are more intense adjacent to the large-scale deformation.

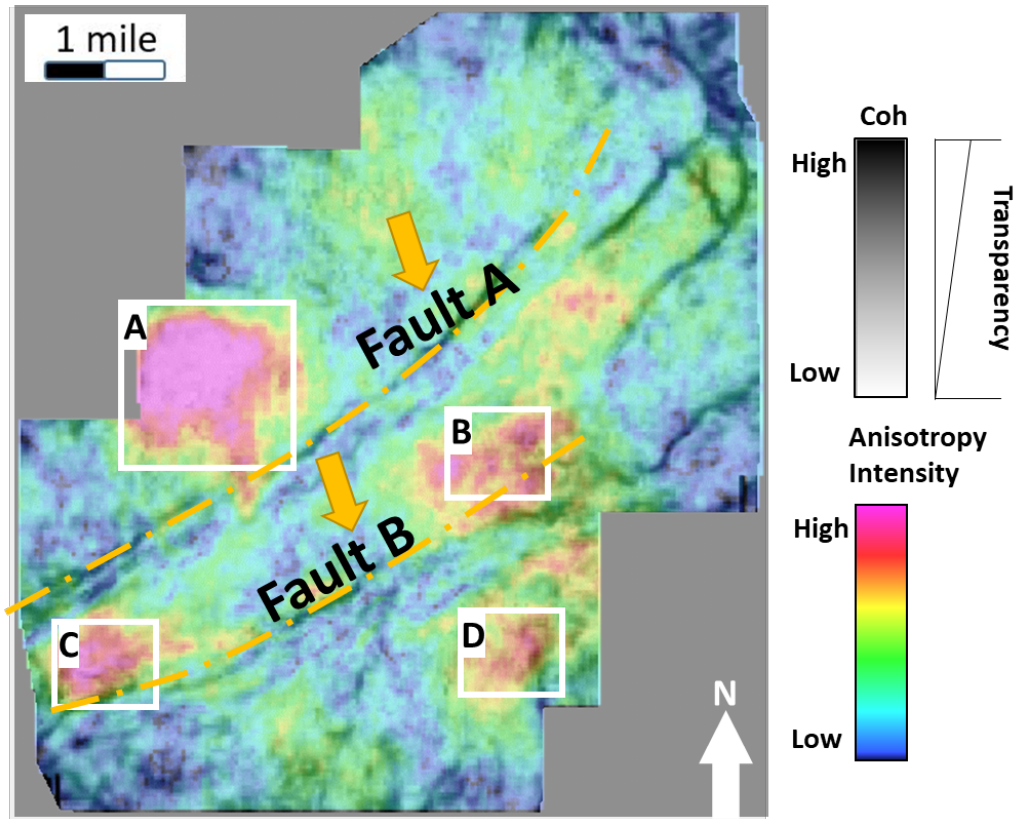


Figure 5.13: Co-rendered map of coherence attribute and anisotropy intensity, the coherence map located in the Base Barnett strata slice and set for transparent for the low coherence value area. The anisotropy intensity map is generated from the Top Barnett (TB) amplitude anisotropy analysis. Four high anisotropy intensity zones are identified as A, B, C, and D. High intensity zones correspond to low coherence areas (lighter transparent area) which indicates the discontinuity is below the resolution of a typical seismic attribute.

Four key geologic horizons showed consistent locations of the high anisotropy zones. The intensity and area of distribution increases from the Top Barnett (TB) to the Base Upper Barnett (BUB), then decreases downward and reaches the lowest intensity until the Base Barnett (BB) (Figure 5.14). This indicates that the base of the Barnett Shale could have fewer vertical natural fractures distributed than the Upper Barnett Shale. This phenomenon can be explained and supported by many field observations that most intense and uniformly oriented deformation was distributed at the tip of the fault plane during growth of the fault (Chinnery, 1966; Cowie and Scholz, 1992; Anders and Wiltschko, 1994; Reches and Lockner, 1994; Cowie and Shipton, 1998;

Vermilye and Scholz, 1998; Katz et al., 2003). The azimuth of the maximum anisotropy which is interpreted as the strike orientation of the vertical fractures shows an azimuth of 30 to 60 degrees throughout the entire formation for Zones A and D. Zones B and C have a slight change in fracture strike direction between the Upper Barnett and Lower Barnett. Zone B anisotropy is oriented west-east at the Top Barnett (TB) and Top Lower Barnett (TLB) surfaces and then changes orientation (northeast-southwest) for the Base Upper Barnett (BUB) and Base Barnett (BB) surfaces. Zone C has an orientation of north-northwest-south-southeast throughout the formation.

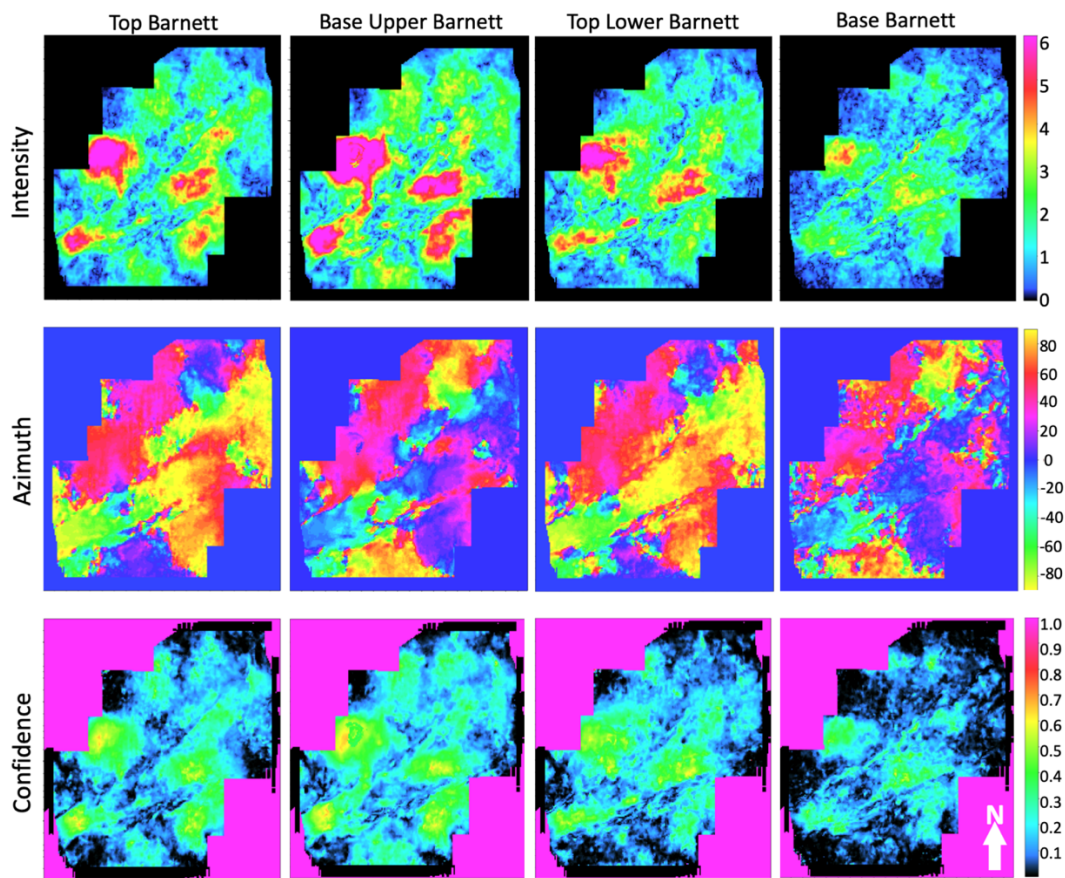


Figure 5.14: Amplitude anisotropy analysis results along the four key horizons shows intensity, azimuth and confidence of anisotropy. The anisotropy intensity decreases geologically downward, and the Upper Barnett generally has higher intensity at all four anisotropy zones than the Lower Barnett Shale. The azimuth of Zones A and D (location indicated in Figure 13) is generally consistent with a northeast-southwest trend. Zones B and C have slightly different azimuths, but locations are consistent throughout the formation.

ENVELOPE ATTRIBUTE ANISOTROPY ANALYSIS

The envelope attribute anisotropy analysis is expected to show better results than amplitude analysis since the envelope attribute has reduced the picking errors by calculating absolute values of seismic amplitude. The anisotropy analysis highlights the same location for the four high anisotropy zones. The intensity result is the same as the amplitude result: increasing from the Top Barnett (TB) towards the Base Upper Barnett (BUB) then decreasing towards the Base Barnett (BB). The azimuth of maximum anisotropy is more consistent among the four key horizons than the amplitude analysis result (Figure 5.15). Zone A, B and D maintain a similar northeast-southwest trend of about 50° strike throughout the formation; zone C has a similar azimuth with amplitude analysis which is different from the other high anisotropy zones: the north-south trend on all four horizons. The envelope results are less patchy and of higher consistency than the amplitude result which makes it more reliable than seismic amplitude anisotropy analysis.

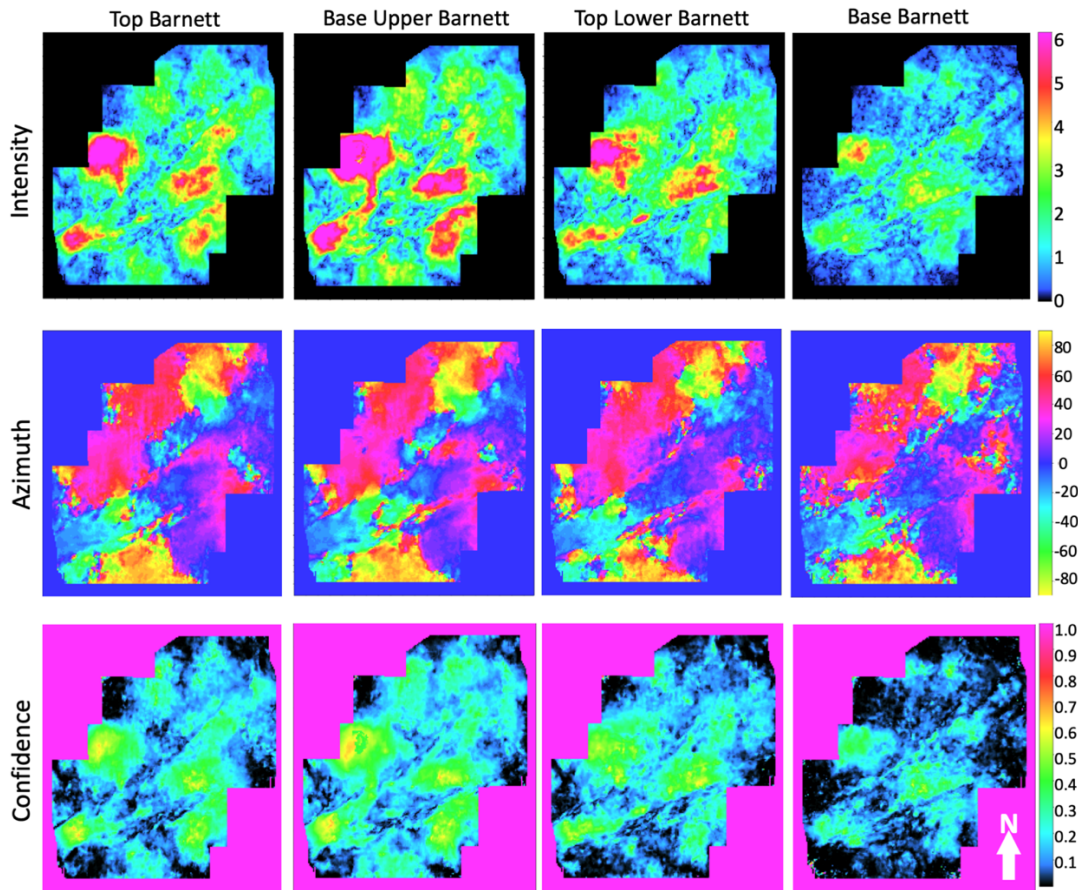


Figure 5.15: Envelope attribute anisotropy analysis result. The intensity result is similar to the amplitude result and azimuth shows a more consistent northeast-southwest trend for Zones A, B and D; zone C has a different north-south trending azimuth. Confidence at high intensity zones is high, making the result reliable for further interpretation.

SPECTRAL PEAK FREQUENCY ATTRIBUTE ANISOTROPY ANALYSIS

Spectral peak frequency seismic attribute anisotropy analysis highlighted the same four zones of high anisotropy as the amplitude and envelope anisotropy result (Figure 5.16). The original peak frequency data is very patchy with low pixel resolution which makes it difficult to reveal the similar anisotropy analysis result with the other attributes. Thus, the spectral peak frequency was calculated and then smoothed before anisotropy analysis. The intensity results show an increasing trend downward. The Zones A, B, and C can be identified from the top three horizons. The azimuth distribution result shows an orthogonal relationship with the other attributes outputs

as expected. Zones A, B and D have an azimuth of northwest southeast (N40W) throughout the formation and Zone C has a west-east orientation. These azimuth outputs indicate the maximum peak frequency orientation which corresponds with maximum amplitude attenuation that is perpendicular to the fracture strike. This azimuth output confirms the other attributes result in an indirect way.

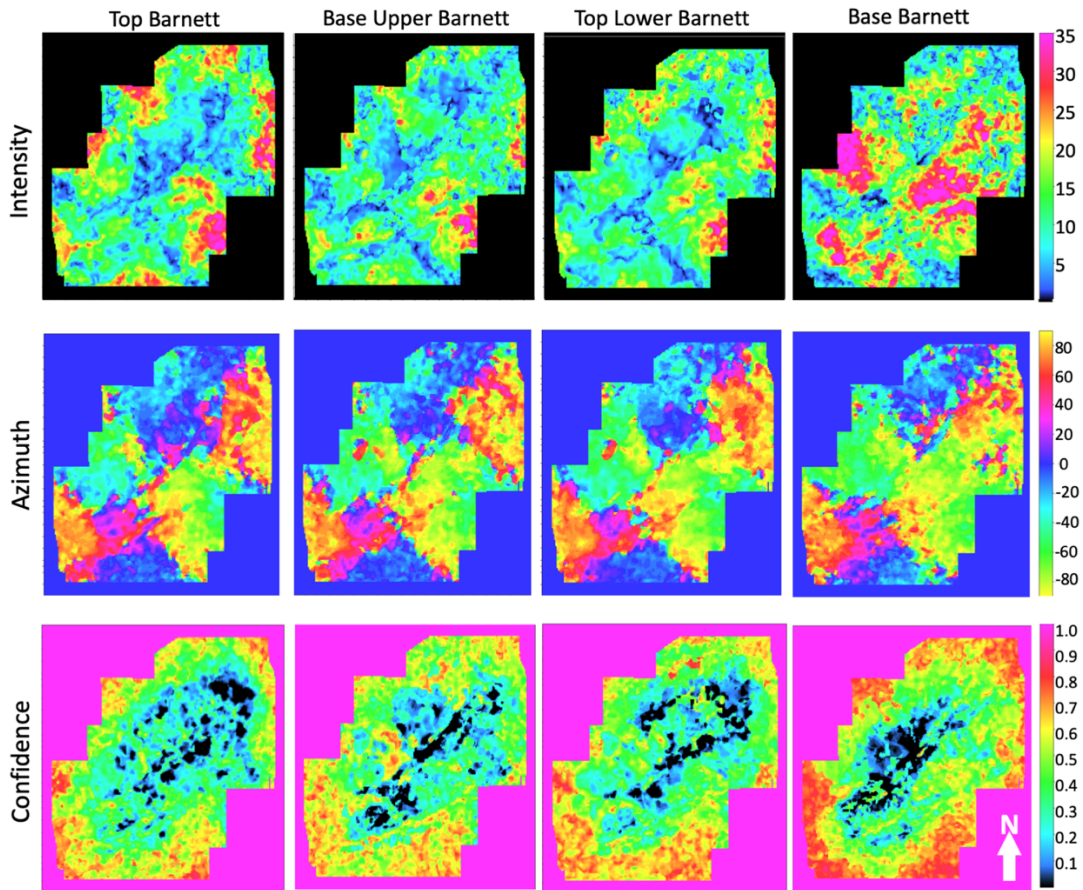


Figure 5.16: Spectral peak frequency attribute anisotropy analysis result, location of the high anisotropy zone is the same with previous results on the Base Barnett surface. The azimuth of the high anisotropy zones shows an orthogonal relationship with amplitude-based attributes.

PRESTACK P-IMPEDANCE ANISOTROPY ANALYSIS

P-impedance calculated from prestack inversion allows extracting the interval property of the Upper and Lower Barnett Shale respectively. Since extracting the inversion result along the

formation boundary is prone to collect the error from horizon picking, the reflection boundary is not an ideal representative of the interval property. As introduced earlier, in order to present the impedance value that is comparable to the other attributes, the 10ms and 15ms phantom horizons were generated below the Top Upper Barnett (TUB) and Top Lower Barnett (TLB) respectively for impedance result flattening on each volume as input for anisotropy analysis. As shown in Figure 5.17, the anisotropy analysis results on intensity and azimuth for the Upper and Lower Barnett reveal the same location of Zones A, B, C, and D. However, the distribution is patchy compared to the former results, which is interpreted as the phantom horizon bias. The azimuths of the maximum anisotropy zones are identical with previous results.

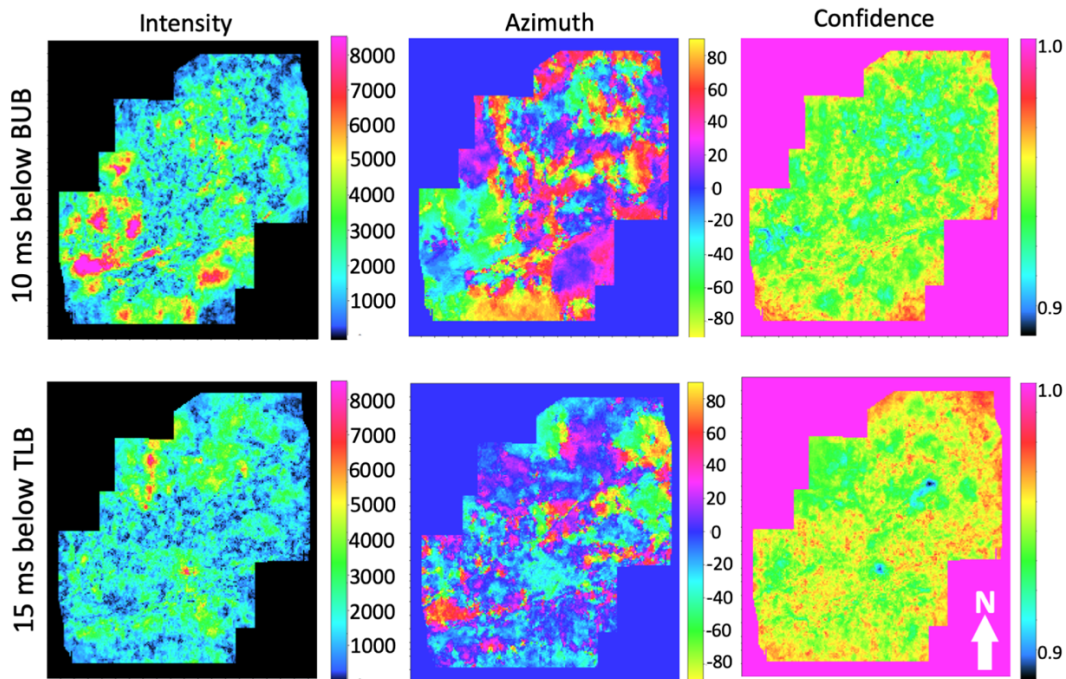


Figure 5.17: Prestack P impedance anisotropy analysis result from two phantom horizons. Zone A, B and C are obvious to locate, but zone D is hard to locate on both surfaces, which generally have lower intensity of anisotropy than the Upper Barnett Shale.

Generally speaking, four attributes' anisotropy analyses all indicate four zones of high anisotropy intensity: Zones, A, B, C and D as highlighted on Figure 5.13, and all four zones are

adjacent to the fault lines. The location of the high intensity zones corresponds with high confidence value for all analyses which confirms the high reliability of the results. Zone B is located in between Faults A and B which indicates that it is most likely affected by both faults. Zone D has a linear geometry that is subparallel to Fault B which indicates that the anisotropy is more likely induced by Fault B deformation. Among all the attributes, envelope is the attribute with higher quality output with consistent intensity and azimuth, non-patchy results throughout the formation.

The intensity of anisotropy from all of these analyses indicate a higher intensity of anisotropy in the Upper Barnett than the Lower Barnett, there is generally an increase from the Top Upper Barnett (TUB) to the Base Upper Barnett (BUB), then the intensity decreases towards the Base Barnett (BB). The highest intensity in the Base Upper Barnett (BUB) surface and bigger area of distribution indicates the fracture density is higher in the Upper Barnett Shale since it is close to the tip of the fault and experienced higher intensity of smaller scale deformation.

The azimuths of the high intensity zones are different, which implies potentially different deformational mechanisms and timing of the natural fractures. Zones A, B and D natural fractures generally share 50° northeast-southwest or north-northeast-south-southwest orientation, which is subparallel to Fault A and B's strike and interpreted paleo maximum horizontal stress orientation from regional structural analysis. This indicates that the natural fractures in Zones A, B and D were formed under the same stress field, mechanism and time with Fault A and B. Zone C fractures have a north-south strike orientation which indicates these fractures formed under the impact of the older stress field according to Gale (2007) and less impacted by Faults A and B. The location of Zone C is also relatively isolated from the fault lines which confirms the conclusion of a different stage of Zone C formation than Zones A, B and D.

RESULT VERIFICATION WITH PRODUCTION MAP

In order to verify that the anisotropy analysis results are associated with the natural fracture network, a first year lateral well gas production map from the Barnett Shale was generated based on public data source IHS and co-rendered with the amplitude anisotropy intensity map of the Base Upper Barnett (BUB) (Figure 5.18). Gas production was standardized based on well lateral length. Zones A, B, C and D barely have production wells located, which means the operators may avoided the anisotropy area due to low production prediction from the other interpretation. Where there is production in the high intensity zone, such as Zone D, the production is not optimistic compared to the other areas of production. On the contrary, where the low anisotropy zones are in blue color, the production is optimistic and performs generally better than in the high anisotropy intensity zones. The high production areas are located near the fault lines which indicates the operators tried to reach the faulted area with higher reservoir connectivity due to the larger scale deformation to enhance production. This observation corresponds with former studies that the natural fractures in the Barnett Shale in this area are mostly sealed and inhibit the fluid flow in the reservoir (Bowker, 2007; Gale et al., 2007; Gale and Holder, 2010; Gasparrini et al., 2014). The hydraulic fracturing triggers a more complex network which is not beneficial to unconventional production for this case (Bowker, 2003; Bowker, 2007; Gasparrini et al., 2014). The production map further supports the assumption that the high anisotropy zones are introduced by sub-seismic scale vertical natural fractures.

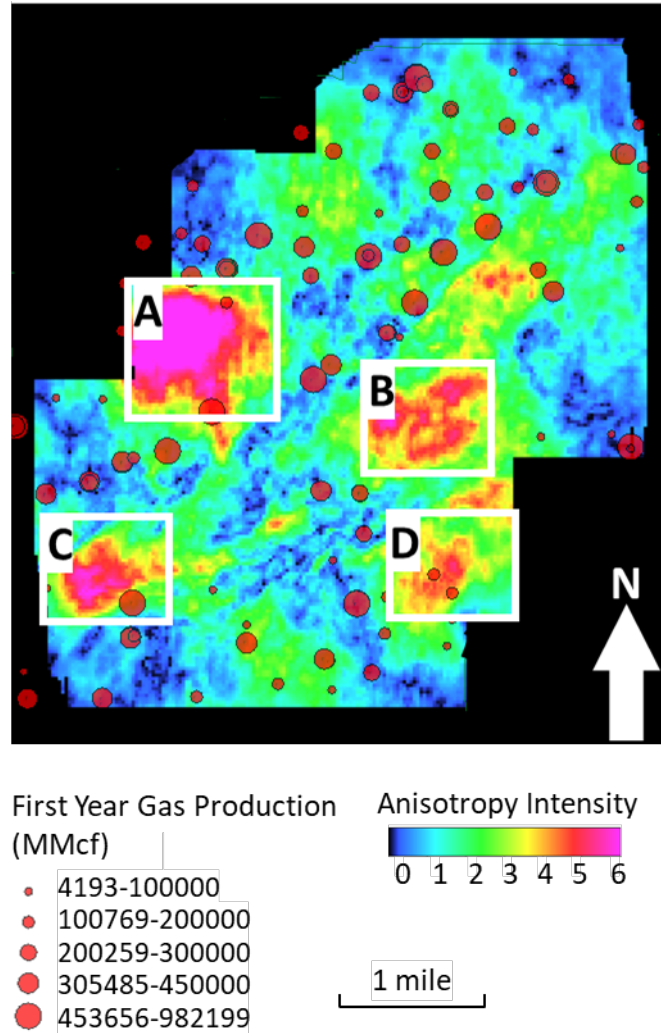


Figure 5.18: Attribute anisotropy intensity map of the Base Upper Barnett co-rendered with a regional gas production map. Note that the production distribution has an inverse relationship with high anisotropy distribution.

DISCUSSION

The fault zone, as larger scale deformations, can be highlighted not only in coherence and curvature seismic attributes but also in anisotropy analysis results (Figure 5.14-5.17). Presence of the fault is associated with low anisotropy intensity, which can be interpreted as fault lines having

uniform large scale discontinuity compared to the smaller scale discontinuity such as a fracture network. Fracture network has higher internal anisotropy since the strike and geometry vary and are impossible to keep uniformly throughout the formation either laterally or vertically. Thus, a fault in azimuthal anisotropy analysis displays a low anisotropy intensity with a linear geometry. Maximum anisotropy azimuth on each side of the fault plane might be altered as displayed (Figure 5.14-5.17).

According to Perez Altamar and Marfurt (2014), The Upper Barnett Shale in the study area is dominated by carbonate rich lithofacies and Lower Barnett Shale is dominated by quartz rich lithofacies, this lithology change can also contribute to a vertical variation in fracture density. When mineralogy plays a role in rock brittleness, calcite rich lithofacies might enhance the fracability of matrix and lead to higher fracture density in the Upper Barnett Shale under the same deformation scenario.

CONCLUSIONS

The azimuthal anisotropy analysis method turned out to be an efficient tool to visualize the natural fracture network below seismic resolution. High anisotropy can be used as an indicator for high occurrence (high density) of vertical, aligned fractures in HTI media.

Not only seismic amplitude, but also other seismic attributes can be used as input for anisotropy analysis such as envelope, spectral peak frequency, and prestack p wave impedance which deliver similar results with high confidence. Envelope attribute has a better result quality and less patchy pattern which can be considered as a more ideal candidate for anisotropy analysis in the future. Picking horizons on azimuthal seismic volumes separately and extracting the seismic attributes along these corresponding horizons can eliminate the VVAz effect which ultimately enhances the accuracy of azimuthal anisotropy analysis.

In this study area, there are four anisotropy zones identified as Zone A, B, C and D. There is a general decreasing trend of anisotropy intensity downward to the base of the Barnett Shale in all four zones. Zone A B and D's fractures are more associated with the deformation of the two nearby normal-strike slip faults. Zone C's fractures are more related to the paleo stress field that occurred even earlier than the other three fracture zones.

The anisotropy analysis workflow proposed in this research not only provides an aerial interpretation of natural fracture network but also a spatial variability of a fracture network throughout the formation. Vertical and aerial variability of anisotropy intensity and azimuth obtained from this workflow make it accessible to understand fracture development history and help determine the best landing zone for potential horizontal wells. Unlike the former natural fracture modeling at the reservoir scale, which assumes natural fractures follow a general azimuth, this workflow proves that the fracture density, azimuth could vary greatly locally due to different deformation ages in a small region which leads to high uncertainty for previous simplified models.

A regional production map verified the assumption that the natural fracture is the main source of anisotropy in the study area. Natural fracture occurrence shows an inverse relationship with gas production which means the natural fractures are sealed and inhibiting production by forming a more complex network with hydraulic fractures. Future production in this area should avoid high natural fracture intensity zones to obtain the best production performance. However, for those fracture networks that are open and promoting production, this workflow can also predict the fracturing sweet spot effectively.

CHAPTER V REFERENCES

Abouelresh, M. O., and R. M. Slatt, 2012, Lithofacies and sequence stratigraphy of the Barnett Shale in east-central Fort Worth Basin, Texas Geohorizon: AAPG bulletin, v. 96, p. 1-22.

- Adams, C., 2003, Barnett Shale: A significant gas resource in the Fort Worth Basin.
- Alali, A., 2018, Seismic Data Conditioning and analysis for fractured reservoirs: Ph.D. Dissertation thesis, University of Oklahoma, 168 p.
- Anders, M. H., and D. V. Wiltschko, 1994, Microfracturing, paleostress and the growth of faults: *Journal of Structural Geology*, v. 16, p. 795-815.
- Anderson, D. L., B. Minster, and D. Cole, 1974, The effect of oriented cracks on seismic velocities: *Journal of Geophysical Research*, v. 79, p. 4011-4015.
- Boadu, F. K., 1995, Fractal characterization of fractures: Effect of fractures on seismic wave velocity and attenuation.
- Boadu, F. K., and L. T. Long, 1996, Effects of fractures on seismic - wave velocity and attenuation: *Geophysical Journal International*, v. 127, p. 86-110.
- Bowker, K. A., 2003, Recent Development of the Barnett Shale Play, Forth Worth Basin: *West Texas Geological Society Bulletin*, v. 2, p. 6.
- Bowker, K. A., 2007, Barnett shale gas production, Fort Worth Basin: Issues and discussion: *AAPG bulletin*, v. 91, p. 523-533.
- Carcione, J. M., 2000, A model for seismic velocity and attenuation in petroleum source rocksAn Acoustic Model for Petroleum Source Rocks: *Geophysics*, v. 65, p. 1080-1092.
- Chen, Q., and S. Sidney, 1997, Seismic attribute technology for reservoir forecasting and monitoring: *The Leading Edge*, v. 16, p. 445-448.
- Chinnery, M. A., 1966, Secondary faulting: II. Geological aspects: *Canadian Journal of Earth Sciences*, v. 3, p. 175-190.
- Chopra, S., and K. J. Marfurt, 2007, Seismic attributes for prospect identification and reservoir characterization, v. 11, *Society of Exploration Geophysicists Tulsa, Oklahoma*.

- Clark, R. A., P. M. Benson, A. J. Carter, and C. A. G. Moreno, 2009, Anisotropic P-wave attenuation measured from a multi-azimuth surface seismic reflection survey: *Geophysical Prospecting*, v. 57, p. 835-845.
- Clifford, P. J., A. R. O'Donovan, K. E. Savory, G. S. Smith, and D. Barr, 2005, Clair Field-managing uncertainty in the development of a waterflooded fractured reservoir: *Offshore Europe*.
- Cowie, P. A., and C. H. Scholz, 1992, Physical explanation for the displacement-length relationship of faults using a post-yield fracture mechanics model: *Journal of Structural Geology*, v. 14, p. 1133-1148.
- Cowie, P. A., and Z. K. Shipton, 1998, Fault tip displacement gradients and process zone dimensions: *Journal of Structural Geology*, v. 20, p. 983-997.
- Gale, J. F., R. M. Reed, S. P. Becker, and W. Ali, 2008, Natural Fractures in the Barnett Shale in the Delaware Basin, Pecos Co. West Texas: Comparison with the Barnett Shale in the Fort Worth Basin.
- Gale, J. F., R. M. Reed, and J. Holder, 2007, Natural fractures in the Barnett Shale and their importance for hydraulic fracture treatments: *AAPG bulletin*, v. 91, p. 603-622.
- Gale, J. F. W., and J. Holder, 2010, Natural fractures in some US shales and their importance for gas production: *Geological Society, London, Petroleum Geology Conference Series*, p. 1131-1140.
- Gasparri, M., W. Sassi, and J. F. Gale, 2014, Natural sealed fractures in mudrocks: A case study tied to burial history from the Barnett Shale, Fort Worth Basin, Texas, USA: *Marine and Petroleum Geology*, v. 55, p. 122-141.

- Gray, D., 2008, Fracture detection using 3D seismic azimuthal AVO: CSEG Recorder, v. 33, p. 38-49.
- Gray, D., S. Boerner, and D. Marinic, 2003, Fractured reservoir characterization using avaz on the Pinedale anticline, Wyoming: Canadian Society of Exploration Geophysicists (CSEG) Recorder (June), p. 40-47.
- Gray, F. D., and K. J. Head, 2000, Using 3D seismic to identify spatially variant fracture orientation in the Manderson field: SPE Rocky Mountain Regional/Low-Permeability Reservoirs Symposium and Exhibition.
- Guo, S., S. Verma, Q. Wang, B. Zhang, and K. J. Marfurt, 2016, Vector correlation of amplitude variation with azimuth and curvature in a post-hydraulic-fracture Barnett Shale survey: Interpretation, v. 4, p. SB23-SB35.
- Helbig, K., and L. Thomsen, 2005, 75-plus years of anisotropy in exploration and reservoir seismics: A historical review of concepts and methods: Geophysics, v. 70, p. 9-23.
- Henry, J. D., 1982, Stratigraphy of the Barnett Shale (Mississippian) and associated reefs in the northern Fort Worth Basin.
- Katz, O., Z. e. Reches, and G. Baer, 2003, Faults and their associated host rock deformation: Part I. Structure of small faults in a quartz–syenite body, southern Israel: Journal of structural geology, v. 25, p. 1675-1689.
- Kerans, C., 1988, Karst-controlled reservoir heterogeneity in Ellenburger Group carbonates of west Texas: AAPG bulletin, v. 72, p. 1160-1183.
- Kuster, G. T., and M. N. Toksöz, 1974, Velocity and attenuation of seismic waves in two-phase media: Part I. Theoretical formulations: Geophysics, v. 39, p. 587-606.

- Li, F., B. Lyu, J. Qi, K. Marfurt, and H. Zhou, 2016, Seismic-attenuation anisotropy and corresponding frequency versus azimuth (FVAZ) attribute, SEG Technical Program Expanded Abstracts 2016, Society of Exploration Geophysicists, p. 352-356.
- Li, F., H. Zhou, N. Jiang, J. Bi, and K. J. Marfurt, 2015, Q estimation from reflection seismic data for hydrocarbon detection using a modified frequency shift method: *Journal of Geophysics and Engineering*, v. 12, p. 577-586.
- Liu, E., 2013, *Seismic fracture characterization: Concepts and practical applications*, Academic Press.
- Liu, J., and K. J. Marfurt, 2007, Instantaneous spectral attributes to detect channels: *Geophysics*, v. 72, p. P23-P31.
- Liu, Y., 2014, AVAZ and VVAZ practical analysis for estimating HTI anisotropic properties, Beijing 2014 International Geophysical Conference & Exposition, Beijing, China, 21-24 April 2014, p. 1132-1135.
- Lund Snee, J. E., and M. D. Zoback, 2016, State of stress in Texas: Implications for induced seismicity: *Geophysical Research Letters*, v. 43.
- Lynn, H., and W. Beckham, 1998, P-wave azimuthal variations in attenuation, amplitude, and velocity in 3D field data: Implications for mapping horizontal permeability anisotropy, SEG Technical Program Expanded Abstracts 1998, Society of Exploration Geophysicists, p. 193-196.
- MacBeth, C., 1999, Azimuthal variation in P-wave signatures due to fluid flow: *Geophysics*, v. 64, p. 1181-1192.

- Mahmoudian, F., G. F. Margrave, J. Wong, and D. C. Henley, 2013, Fracture orientation and intensity from AVAz inversion: A physical modeling study, SEG Technical Program Expanded Abstracts 2013, p. 483-487.
- Maultzsch, S., M. Chapman, E. Liu, and X. Y. Li, 2007, Modelling and analysis of attenuation anisotropy in multi - azimuth VSP data from the Clair field: Geophysical Prospecting, v. 55, p. 627-642.
- McBee Jr, W., 1999, Regional paleo-geography and geology of the southern midcontinent: The Permian Basin: Providing energy for the future: West Texas Geological Society Publication, p. 99-106.
- Montgomery, S. L., D. M. Jarvie, K. A. Bowker, and R. M. Pollastro, 2005, Mississippian Barnett Shale, Fort Worth basin, north-central Texas: Gas-shale play with multi-trillion cubic foot potential: AAPG bulletin, v. 89, p. 155-175.
- Perez Altamar, R., and K. Marfurt, 2014, Mineralogy-based brittleness prediction from surface seismic data: Application to the Barnett Shale: Interpretation, v. 2, p. T1-T17.
- Perez, G., and K. J. Marfurt, 2007, New azimuthal binning for improved delineation of faults and fractures: Geophysics, v. 73, p. S7-S15.
- Pollastro, R. M., D. M. Jarvie, R. J. Hill, and C. W. Adams, 2007, Geologic framework of the Mississippian Barnett shale, Barnett-paleozoic total petroleum system, Bend arch-Fort Worth basin, Texas: AAPG bulletin, v. 91, p. 405-436.
- Qi, J., F. Li, T. Zhao, T. Lin, and K. Marfurt, 2015, Correcting for VVAz prior to AVAz analysis, SEG Technical Program Expanded Abstracts 2015, Society of Exploration Geophysicists, p. 321-325.

- Reches, Z. e., and D. A. Lockner, 1994, Nucleation and growth of faults in brittle rocks: *Journal of Geophysical Research: Solid Earth*, v. 99, p. 18159-18173.
- Rüger, A., 2002, Reflection coefficients and azimuthal AVO analysis in anisotropic media, *Society of Exploration Geophysicists*.
- Russell, B., D. Hampson, J. Schuelke, and J. Quirein, 1997, Multiattribute seismic analysis: *The Leading Edge*, v. 16, p. 1439-1444.
- Samec, P., and J. P. Blangy, 1992, Viscoelastic attenuation, anisotropy, and AVO: *GEOPHYSICS*, v. 57, p. 441-450.
- Schoenberg, M., and J. Douma, 1988, Elastic wave propagation in media with parallel fractures and aligned cracks: *Geophysical prospecting*, v. 36, p. 571-590.
- Singh, P., R. Slatt, and W. Coffey, 2008, Barnett Shale—Unfolded: Sedimentology, sequence stratigraphy, and regional mapping.
- Taner, M., and R. E. Sheriff, 1977, Application of amplitude, frequency, and other attributes to stratigraphic and hydrocarbon determination: Section 2. Application of seismic reflection configuration to stratigraphic interpretation.
- Taner, M. T., 2001, Seismic attributes: *CSEG recorder*, v. 26, p. 49-56.
- Thompson, A., J. Rich, and M. Ammerman, 2010, Fracture characterization through the use of azimuthally sectored attribute volumes, *SEG Technical Program Expanded Abstracts 2010*, *Society of Exploration Geophysicists*, p. 1433-1437.
- Thompson, A. M., 2010, Induced fracture detection in the Barnett Shale, Ft. Worth Basin, Texas: Master's thesis thesis, University of Oklahoma.
- Thompson, D. M., 1988, Fort Worth Basin: The geology of North America: *Geological Society of America*, v. 2, p. 346-352.

- Thomsen, L., 1986, Weak elastic anisotropy: *Geophysics*, v. 51, p. 1954-1966.
- Trumbo, D. B., 2014, A production calibrated reservoir characterization of the Mississippi Lime in a mature field utilizing reprocessed legacy 3D seismic data, Kay County, Oklahoma, University of Oklahoma.
- Tsvankin, I., and V. Grechka, 2011, Seismology of azimuthally anisotropic media and seismic fracture characterization, Society of Exploration Geophysicists Tulsa, OK.
- Vermilye, J. M., and C. H. Scholz, 1998, The process zone: A microstructural view of fault growth: *Journal of Geophysical Research: Solid Earth*, v. 103, p. 12223-12237.
- Walper, J., 1981, Geological evolution of the Gulf of Mexico-Caribbean region.
- Wang, Y., S. Chen, and X.-Y. Li, 2015, Anisotropic characteristics of mesoscale fractures and applications to wide azimuth 3D P-wave seismic data: *Journal of Geophysics and Engineering*, v. 12, p. 448.
- Wang, Z., 2002, Seismic anisotropy in sedimentary rocks, part 1: A single-plug laboratory method: *Geophysics*, v. 67, p. 1415-1422.
- White, R. E., 1991, Properties of instantaneous seismic attributes: *The Leading Edge*, v. 10, p. 26-32.
- Zhang, K., Y. Guo, B. Zhang, A. M. Trumbo, and K. J. Marfurt, 2013, Seismic azimuthal anisotropy analysis after hydraulic fracturing: *Seismic azimuthal anisotropy analysis: Interpretation*, v. 1, p. SB27-SB36.
- Zhu, Y., I. Tsvankin, P. Dewangan, and K. v. Wijk, 2007, Physical modeling and analysis of P-wave attenuation anisotropy in transversely isotropic media: *GEOPHYSICS*, v. 72, p. D1-D7.

CHAPTER VI

DISCUSSION AND SUMMARY OF CHAPTERS

This dissertation includes natural fracture characterization that use multidisciplinary methods to study natural fractures in the unconventional Woodford and Barnett Shale at different scales. Based on the results obtained from the previous chapters, some of the key takeaway points and discussions on the natural fracture studies are summarized below.

1. Natural fracture characterization from the outcrop cannot be directly applied on the subsurface scenario. The shale formation exposed on the outcrop usually deformed under a higher structural deformation process and lower confining pressure than the subsurface scenario, thus always presents higher aperture and more intense failure structures. The same formation in the subsurface unlikely undergoes the same extent of deformation and the higher confining pressure makes the formation harder for natural fractures to occur in the subsurface.
2. For the blocky rock, rock elastic properties play an important role in failure occurrence in the matrix. For example, the higher the brittleness of the rock, the easier the rock forms natural fractures under the same stress field. However, for the unconventional shale, laminae and interbed depositional structures are well developed, and the rock elastic properties do not contribute to rock failures as much as do depositional structures. This interbed depositional structure greatly enhances the fracability of the reservoir rock and can be directly related to fracture density. Under the same stress regime and deformational mechanism, the bed frequency can contribute about three times more to fracture density than the rock mechanical properties. This effect needs

to be further emphasized when predicting fracture density in unconventional shale reservoirs. For example, quartz content alone does not predict fracability

3. The layering effect caused by the interbed depositional structure introduce anisotropy within the shale. More layers in a unit thickness interval, higher the anisotropy of the rock is, and the fracture density will be higher compared to a fewer layers scenario. For unconventional shale, anisotropy is a nonnegligible factor that controls distribution of natural fractures: the regional structure introduces strain that leads to rock failure, the intensity of the failure is then affected heavily by the layering anisotropy within the rock.
4. For larger field scale characterization, seismic anisotropy obtained from wide/full azimuth prestack seismic data can be used as an indicator of fractures when the vertical larger scale fractures are present in the reservoir. The anisotropy analysis workflow proposed in Chapter V can provide not only intensity but also deformational history out of the azimuth outcome. The seismic anisotropy has its advantage on larger aerial analysis that can be tied better with regional structures compared to cores and outcrop that have limited exposure.

A comprehensive study of natural fractures based on all the available types of data is necessary to enhance the efficiency of unconventional reservoirs economic development and can provide insight into locating the best production zone in the reservoir. Properly integrating all the available data types and incorporating the interpretation results into a bigger picture is the main purpose of this dissertation. The characterization methods for the natural fractures are well developed, but shale reservoirs need to be comprehended differently rather than using the typical characterization workflows. Thus, a new workflow designed just for unconventional shale

fractures is proposed in Figure 6.1. The benefit of this workflow includes: 1. It emphasizes the geologic impacts on natural fractures occurrence in unconventional reservoirs such as interbed deposition and regional structures; 2. It provides variable options for different types of data and incorporate multiscale characterizations; 3. It reasonably incorporates not just the occurrence of fractures but also a fracture density prediction function that can directly benefit reservoir evaluation and development strategy.

The first step is to start from direct observation of the reservoir rock from the core and outcrop to establish the basic geologic feature of the target shale reservoir for an analog. This step is a qualification process of the fracture type and reservoir rock so that the type of anisotropy and fracture can be categorized. The second step is to conduct a quantification characterization using all available rock and subsurface data such as core, well log and seismic to establish a mechanical model of the reservoir. The third step is integrating all the interpretation results from different scales to establish a natural fracture model which includes features such as fracture density, fracture orientation, regional structure model, and fractures 3D distribution pattern. Reservoir simulation can also be conducted in this stage to upgrade it into a dynamic model. Once the model is polished by multidisciplinary interpretation, the model can be verified by regional production data and additional cores/image logs. This workflow can provide a complete and comprehensive understanding of the shale reservoir fractures by integrating different scales and types of data.

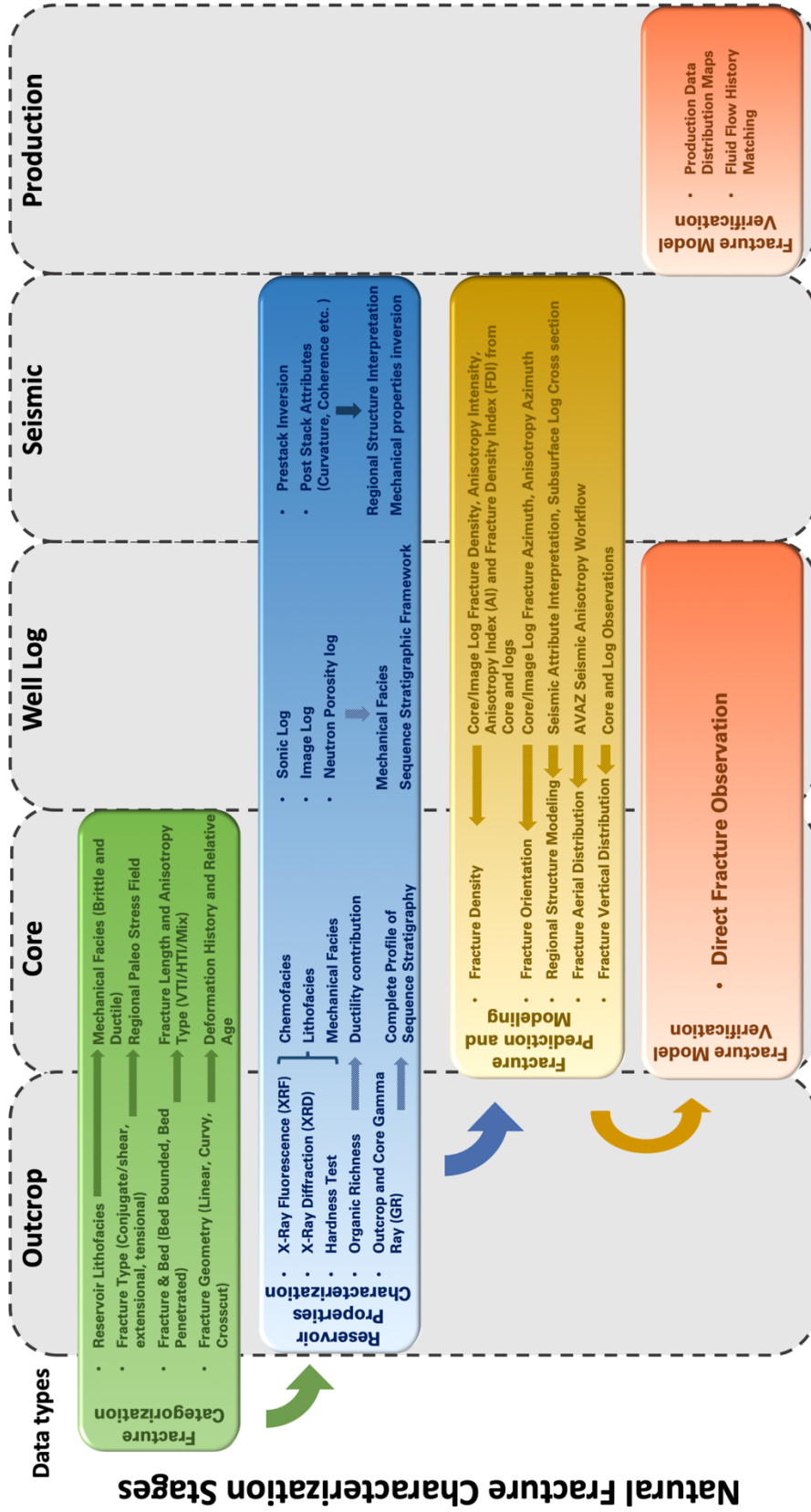












Figure 6.1: Comprehensive Natural Fracture Characterization Workflow for the unconventional shale reservoir.




APPENDIX A



Hall 2B Core Fracture Characterization


Core Depth	Core photo	Core/ Fracture description/ Detailed Characterization	Fracture density (#/ft ²)
6144-6145		<ul style="list-style-type: none"> • Bed dips 25 degrees • Laminated dark brown ductile shale interbedded with light gray organic lean shale 	Not available
6144-6145		<ul style="list-style-type: none"> • Highly laminated green shale broken into chips. The green shale section marks the formation boundary between upper Mississippian Limestone and Lower Woodford Shale 	Not available
6146-6146.5		<ul style="list-style-type: none"> • Diagenetic concretions 	Not available




Core Depth	Core photo	Core/ Fracture description/ Detailed Characterization	Fracture density (#/ft ²)
6146.8-6147		<ul style="list-style-type: none"> • Diagenetic concretions in light gray- green shale 	Not available
6147-6148		<ul style="list-style-type: none"> • Diagenetic concretions in light gray- green shale 	Not available
6148-6149		<ul style="list-style-type: none"> • Diagenetic concretions in light gray- green shale 	Not available
6149-6149.1			




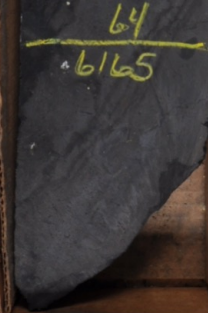
Core Depth	Core photo	Core/ Fracture description/ Detailed Characterization	Fracture density (#/ft ²)
6149.1-6150		<ul style="list-style-type: none"> • Diagenetic concretions in light gray shale 	Not available
6150-6151		<ul style="list-style-type: none"> • Diagenetic concretions in light gray shale 	Not available
6151-6151-4		<ul style="list-style-type: none"> • Light gray shale with missing cores 	Not available




Core Depth	Core photo	Core/ Fracture description/ Detailed Characterization	Fracture density (#/ft ²)
6151.4-6162		<ul style="list-style-type: none"> • Light gray shale with concretion at 6152 ft • Beds are horizontal 	Not available
6152-6153		<ul style="list-style-type: none"> • Light gray shale • Beds are slightly increasing in dipping angle 	Not available
6153-6153.7		<ul style="list-style-type: none"> • Light gray shale • Horizontal beds 	Not available




Core Depth	Core photo	Core/ Fracture description/ Detailed Characterization	Fracture density (#/ft ²)
6154-6155		<ul style="list-style-type: none"> • Diagenetic concretions in light gray shale • Diagenetic concretions in light gray shale • 45 degrees dipping beds • Mineral filled horizontal fracture • Missing core section 	Not available
6155-6155.6		<ul style="list-style-type: none"> • Slightly dipping fine laminated light gray to medium gray shale 	Not available




Core Depth	Core photo	Core/ Fracture description/ Detailed Characterization	Fracture density (#/ft ²)
6155.9-6156			Not available
6156-6157		<ul style="list-style-type: none"> Horizontal fine laminated light gray to medium gray shale with concretion at 6156 ft 	Not available
6157-6158		<ul style="list-style-type: none"> Highly deformed section with developed vertical and bed boundary failure Missing core about 5 inches Sharp change in dipping angle into about 80 degrees with bed boundary failure 	Not available
6158-6158.2			




Core Depth	Core photo	Core/ Fracture description/ Detailed Characterization	Fracture density (#/ft ²)
6158-6159		<ul style="list-style-type: none"> • Almost vertical bed with bed boundary in wavy form, could form as a slump and fault shearing at early stage of faulting 	Not available
6159-6160		<ul style="list-style-type: none"> • Highly deformed core 	Not available
6160-6160.4		<ul style="list-style-type: none"> • High angle bedding with breccia 	Not available


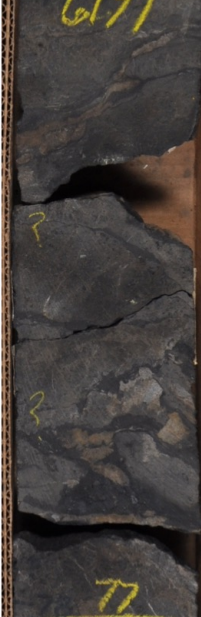
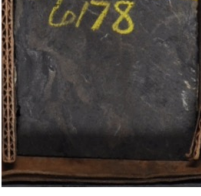
Core Depth	Core photo	Core/ Fracture description/ Detailed Characterization	Fracture density (#/ft ²)
6162.8-6163		<ul style="list-style-type: none"> highly deformed from 6160.4-6162 	Not available
6163-6164		<ul style="list-style-type: none"> Bed boundary hard to identify, curved beds at 6163.5 	Not available
6164-6165		<ul style="list-style-type: none"> Potential structural unconformity surface with bed boundary crosscut each other 	Not available
6165-6165.3		<ul style="list-style-type: none"> Highly dipping bed with wavy bed boundaries 	Not Available




Core Depth	Core photo	Core/ Fracture description/ Detailed Characterization	Fracture density (#/ft ²)
6165.3-6166		<ul style="list-style-type: none"> Highly dipping bed with wavy bed boundaries, which interpreted as shearing fault surface deformation 	Not available
6166-6167			Not available
6167-6168		<ul style="list-style-type: none"> Missing core pieces 	Not available

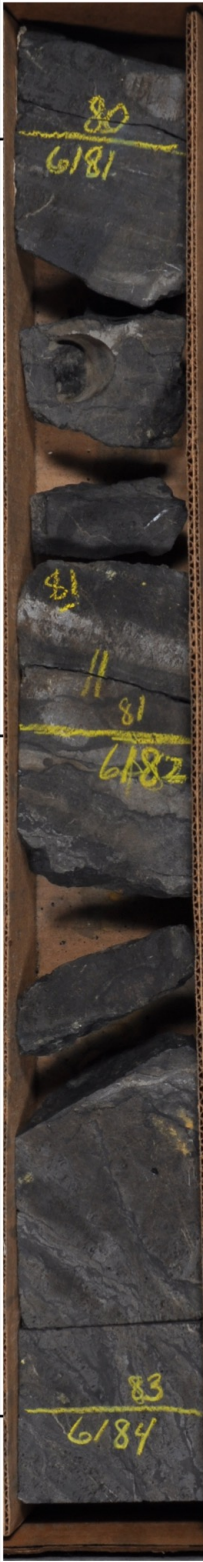
Core Depth	Core photo	Core/ Fracture description/ Detailed Characterization	Fracture density (#/ft ²)
6168.8-6169		<ul style="list-style-type: none"> Breccia found at 6168.8 ft Highly dipping bed with bed boundary hard to identify 	Not available
6169-6170		<ul style="list-style-type: none"> Highly dipping bed with bed boundary hard to identify Fault plane zone deformation with breccia found 7170 	Not available
6170-6171			Not available




Core Depth	Core photo	Core/ Fracture description/ Detailed Characterization	Fracture density (#/ft ²)
6171-6172		<ul style="list-style-type: none"> Highly dipping bed with bed boundary hard to identify, breccia found at 6171.5 ft 	Not available
6172-6173		<ul style="list-style-type: none"> Sharp change in dip angle could be caused by mini fold axis Breccia in round shape found at 6172.3 ft 	Not available
6173-6173.4		<ul style="list-style-type: none"> Reverse in bed dip angle again, bed boundary hard to identify 	Not available





Core Depth	Core photo	Core/ Fracture description/ Detailed Characterization	Fracture density (#/ft ²)
6173.4-6174		<ul style="list-style-type: none"> • Heavily deformed core section 	Not available
6174-6175		<ul style="list-style-type: none"> • Heavily deformed core section 	Not available
6175-6176		<ul style="list-style-type: none"> • Highly dipping bed with wavy bed boundary, breccia found at 6175.5 ft 	Not available




Core Depth	Core photo	Core/ Fracture description/ Detailed Characterization	Fracture density (#/ft ²)
6176-6177		<ul style="list-style-type: none"> • Dark gray in color • Highly dipping bed (45 degrees) with wavy bed boundary, breccia found at 6176.8 ft 	Not available
6177-6178		<ul style="list-style-type: none"> • Sharp change in dip angle could be caused by mini fold axis • Breccia zone at 6177.7 ft 	Not available
6178-6178-2			Not available




Core Depth	Core photo	Core/ Fracture description/ Detailed Characterization	Fracture density (#/ft ²)
6178.2-6179		<ul style="list-style-type: none"> Breccia zone at 6178.7 ft 	Not available
6179-6180		<ul style="list-style-type: none"> Gentle dipping bed with 20 degrees, bed boundary is wavy in shape and found shearing deformation at 6179.9 ft 	Not available
6180-6180.8		<ul style="list-style-type: none"> Single bed mini fault found at 6180.8 ft 	Not available




Core Depth	Core photo	Core/ Fracture description/ Detailed Characterization	Fracture density (#/ft ²)
6180.8-6181			Not available
6181-6182		<ul style="list-style-type: none"> Gentle dipping bed with <20 degrees, bed boundary is identifiable found elongated breccia at 6181.9 ft 	Not available
6182-6183		<ul style="list-style-type: none"> Reverse in dip direction, could be caused by small scale fold axis Reverse in dip direction, could be caused by small scale fold axis 	Not available
6184-6184.1			


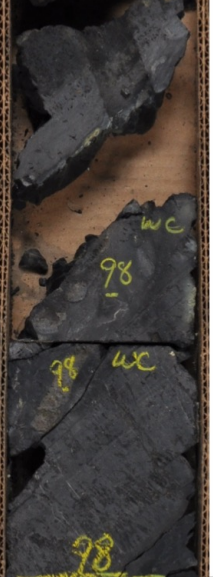

Core Depth	Core photo	Core/ Fracture description/ Detailed Characterization	Fracture density (#/ft ²)
6184.2-6185		<ul style="list-style-type: none"> • Beds are all wavy in shape which indicates high shearing deformation • Open fracture can be found in some of the beds and all bed bounded • Bed dip direction changes three times in this section and located at 6185, 6185.3, 6185.8 ft indicates high intensity folding procedure in this section 	Not available
6185-6186		<ul style="list-style-type: none"> • Pyrite nodulus found t 6185.8 ft, fold axis barely have core preserved 	Not available
6186-6186.6			Not available


Core Depth	Core photo	Core/ Fracture description/ Detailed Characterization	Fracture density (#/ft ²)
6186.6-6187			Not available
6187-6188		<ul style="list-style-type: none"> • Heavily disturbed section from 6186.6-6188, bed boundary can not be distinguished, opened fracture developed as bed bounded form. • Pyrite nodulus found at 6188 ft 	Not available
6188-6189		<ul style="list-style-type: none"> • Almost vertical beds indicates fault surface shearing zone 	Not available
6189-6189.5		<ul style="list-style-type: none"> • Gentle dipping beds with open fractures developed 	




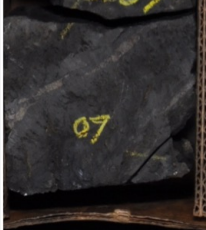
Core Depth	Core photo	Core/ Fracture description/ Detailed Characterization	Fracture density (#/ft ²)
6190.7-6191		<ul style="list-style-type: none"> Missing core from 6189.5-6190.7 ft 	Not available
6191-6192		<ul style="list-style-type: none"> Bed dip direction changes two times in this section and located at 6192, 6192.5ft indicates high intensity folding procedure in this section 	Not available
6192-6193			Not available




Core Depth	Core photo	Core/ Fracture description/ Detailed Characterization	Fracture density (#/ft ²)
6193-6194		<ul style="list-style-type: none"> Missing core from 6190.8-6193.5 ft 	Not available
6194-6195		<ul style="list-style-type: none"> Beds are hard to identify in this section, some previous flattened nodulus was found at 6196.5 ft. Open fracture developed within each brittle beds Breccia found at 6193.5 and 6195.5 ft. 	Not available
6195-6195.5			Not available


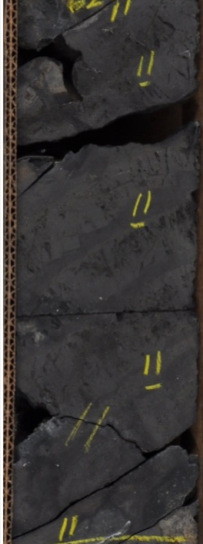


Core Depth	Core photo	Core/ Fracture description/ Detailed Characterization	Fracture density (#/ft ²)
6195.5-6196		<ul style="list-style-type: none"> • A complete fold axis is preserved in this section with axis located roughly at 6196 ft, • The bed dip direction was reversed gradually above and below 6196 ft, part of the bed boundary can be clearly identified. • Opened fracture can be found along the brittle beds 	Not available
6196-6197			Not available
6197-6197.8			Not available




Core Depth	Core photo	Core/ Fracture description/ Detailed Characterization	Fracture density (#/ft ²)
6197.8-6198		<ul style="list-style-type: none"> • Core section is heavily deformed and poorly preserved • Opened fracture can be captured commonly • Beds are generally dip 45 degrees with two distinguishable lithofacies. 	Not available
6198-6199			Not available
6199-6200			Not available



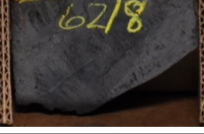
Core Depth	Core photo	Core/ Fracture description/ Detailed Characterization	Fracture density (#/ft ²)
6201-6202		<ul style="list-style-type: none"> Beds are highly dipping with open fractures in the brittle beds with medium gray in color, the ductile beds are much thinner in dark gray color and act like fracture barrier 	Not available
6202-6203		<ul style="list-style-type: none"> Flattened nodulus found at 6202.5 	Not available
6203-6203.3		<ul style="list-style-type: none"> Rounded nodulus found at 6203.2 	Not available




Core Depth	Core photo	Core/ Fracture description/ Detailed Characterization	Fracture density (#/ft ²)
6204-6205		<ul style="list-style-type: none"> • Bed dip in 45 angle • Fractures are open • Minor increase in ductile bed thickness 	Not available
6205-6206		<ul style="list-style-type: none"> • Reverse dipping direction at 6205.2, indicates a potential mini fold axis • Three flattened nodulus found at 6205.4 	Not available
6206-6207		<ul style="list-style-type: none"> • Beds are generally dip in 45 degrees • Bed boundaries are not linear • Fractures are open and vertical to the beds • Elliptical shape nodulus found at 6206.3 	Not available
6207-6207.3			Not available




Core Depth	Core photo	Core/ Fracture description/ Detailed Characterization	Fracture density (#/ft ²)
6207.3-6208		<ul style="list-style-type: none"> • Deformed core section • Core from 6208-6209 is mostly missing 	Not available
6208-6209			Not available
6209-6210		<ul style="list-style-type: none"> • Rounded phosphate nodulus in 6209.2 ft • Open fractures well developed in brittle beds 	Not available
6210-6210.5		<ul style="list-style-type: none"> • Bed boundary hard to identify due to the fault plane deformation and shearing 	Not available




Core Depth	Core photo	Core/ Fracture description/ Detailed Characterization	Fracture density (#/ft ²)
6210.5-6211		<ul style="list-style-type: none"> • Heavily deformed core section from 6210.5-6211 ft 	Not available
6211-6212		<ul style="list-style-type: none"> • Beds dip in 45 degrees • Open fracture are subvertical to the brittle beds 	Not available
6212-6213		<ul style="list-style-type: none"> • Heavily deformed core section 	Not available
6213-6213.3			Not available



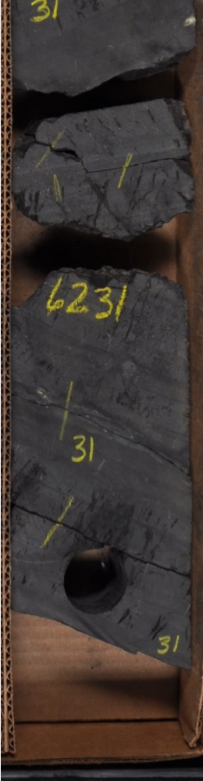
Core Depth	Core photo	Core/ Fracture description/ Detailed Characterization	Fracture density (#/ft ²)
6213.3-6214		<ul style="list-style-type: none"> • Heavily deformed core section from 6213-6214 • Open fractures are still observable 	Not available
6214-6215		<ul style="list-style-type: none"> • Flattened nodulus at 6214.2 ft, the open fractures are constrained within the nodulus • Open fractures are well developed in the brittle beds, ductile beds in dark gray color constrain the growth of the fractures 	Not available
6215-6215.3		<ul style="list-style-type: none"> • Pyrite nodulus identified at 6215.2 near the core plug 	Not available

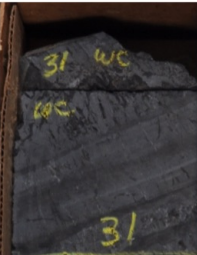

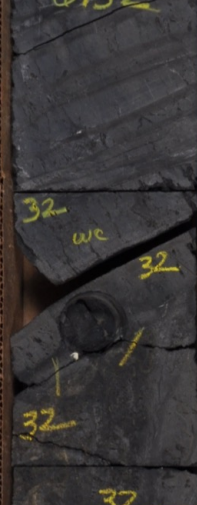



Core Depth	Core photo	Core/ Fracture description/ Detailed Characterization	Fracture density (#/ft ²)
6215.3-6216		<ul style="list-style-type: none"> • Bed boundaries are hard to identify • Flattened nodulus are distorted at 6215.4 • Flattened nodulus bed identified at 6216 ft 	Not available
6216-6217		<ul style="list-style-type: none"> • Reverse dipping direction twice at 6216.4, 6217.2 indicates a potential mini fold axis • Bed boundaries are hard to identify • Fracture Vein found at 6217.9 ft 	Not available
6218-6218.1			Not available




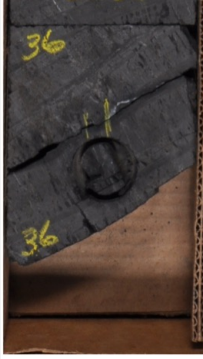
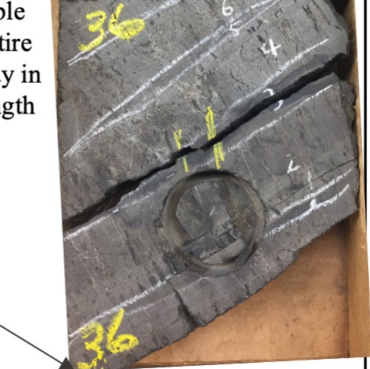
Core Depth	Core photo	Core/ Fracture description/ Detailed Characterization	Fracture density (#/ft ²)
6222.6-6223		<ul style="list-style-type: none"> • Flattened nodulus are identified at 6222.8 ft 	Not available
6223-6224		<ul style="list-style-type: none"> • Flattened nodulus are identified at 6223.2-6223.4 ft • Beds dip in 45 degrees angle with bed bounded open fractures 	Not available
6224-6224.7			Not available

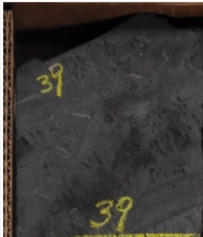


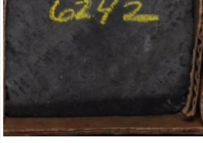
Core Depth	Core photo	Core/ Fracture description/ Detailed Characterization	Fracture density (#/ft ²)
6224.7-6225			Not available
6225-6226		<ul style="list-style-type: none"> • Almost vertical heavily deformed beds with small scale stepping faults identified at 6225 ft • Flattened nodulus are identified at 6225.9ft 	Not available
6226-6226.9		<ul style="list-style-type: none"> • Missing core section • Open fractures are bed bounded and observable 	Not available



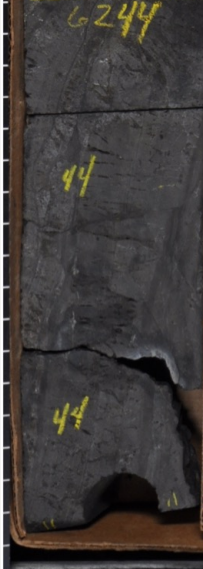
Core Depth	Core photo	Core/ Fracture description/ Detailed Characterization	Fracture density (#/ft ²)
6226.9 -6227			Not available
6228-6229		<ul style="list-style-type: none"> • Bed dip angle changed as a curved trend from 6227-6227.5 ft. Part of this foot is missing • Fractures are opened and bed bounded • Heavily deformed core section 	Not available
6229-6229.7		<ul style="list-style-type: none"> • Bed bounded open fractures are less developed 	Not available






Core Depth	Core photo	Core/ Fracture description/ Detailed Characterization	Fracture density (#/ft ²)
6229.7-6230			Not available
6230-6231		<ul style="list-style-type: none"> • Bed dips in a gentler angle • Open fracture are subvertical-vertical to brittle beds • Flattened nodulus identified at 6230.2-6230.5ft • Part of the 6230 ft section is missing 	Not available
6231-6231.7		<ul style="list-style-type: none"> • Reverse in bed dip direction indicates a potential mini fold axis 	Not available





Core Depth	Core photo	Core/ Fracture description/ Detailed Characterization	Fracture density (#/ft ²)
6131.7-6132			Window 33 Bed 15-20 Fracture density is 1053.951
6132-6233			Window 32 Bed 15-20 Fracture density is 672.056
6233-6234		<ul style="list-style-type: none"> • Bed dips 20-30 degrees • 14 beds at 6231-6232 ft with vertical opened fracture characterized, and separated into two windows with 1-6, and 7-14 layers • Ductile layers are thinner than brittle layers • Most of the vertical fractures are not able to penetrate the entire brittle beds and stay in a short fracture length <ul style="list-style-type: none"> • Beds are almost vertical • Bed boundaries are hard to identify, crosscut bed boundary, wave bed boundaries are common, which indicates this core section located within a fault plane shearing zone • High density of open fracture are identifiable 	
6234-6234.1			



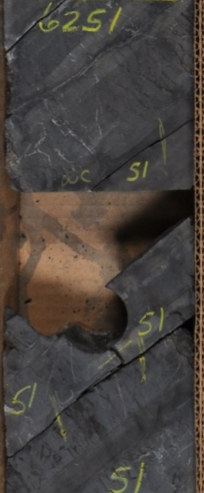
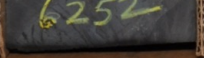

Core Depth	Core photo	Core/ Fracture description/ Detailed Characterization	Fracture density (#/ft ²)
6234.1-6235			<p>Window 31 Bed 15-20 Fracture density is 366.638</p>
6235-6236		<ul style="list-style-type: none"> • Bed dips 20-30 degrees • 20 beds at 6235-6236 ft with conjugate opened fracture characterized, and separated into two windows with 1-14, and 15-20 layers • Ductile layers are thinner than brittle layers • Most of the vertical fractures are not able to penetrate the entire brittle beds and stay in a short fracture length 	
6236-6236.5			<p>Window 30 Bed 1-14 Fracture density is 966.21</p>


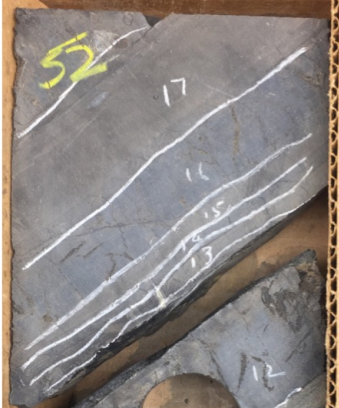

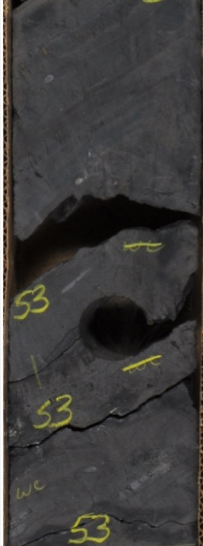

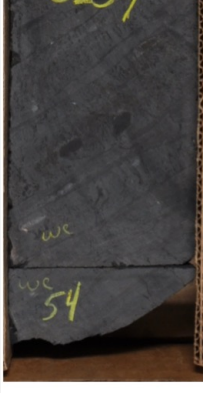

Core Depth	Core photo	Core/ Fracture description/ Detailed Characterization	Fracture density (#/ft ²)
6239.6-6240		<ul style="list-style-type: none"> • Beds are almost vertical • Bed boundaries are hard to identify, crosscut bed boundary, wave bed boundaries are common, which indicates this core section located within a fault plane shearing zone • High density of open fracture are identifiable 	Not available
6240-6241			Not available
6241-6242			Not available
6242-6242.2			

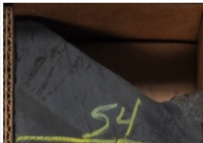
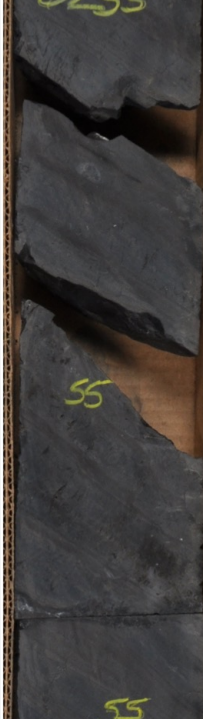
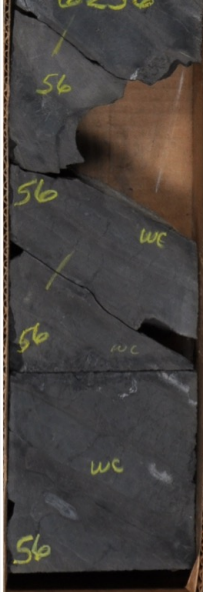
Core Depth	Core photo	Core/ Fracture description/ Detailed Characterization	Fracture density (#/ft ²)
6242.2-6243		<ul style="list-style-type: none"> • Beds are almost vertical • Bed boundaries are hard to identify, crosscut bed boundary, wave bed boundaries are common, which indicates this core section located within a fault plane shearing zone • High density of open fracture are identifiable 	Not available
6243-6244			Not available
6244-6244.9			Not available


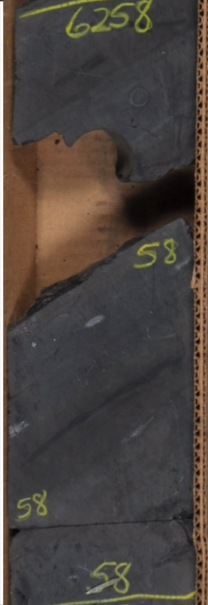


Core Depth	Core photo	Core/ Fracture description/ Detailed Characterization	Fracture density (#/ft ²)
6244.9-6245			Window 29 Bed 13-18 Fracture density is 503.475
6245-6246			Window 27 Bed 1-8 Fracture density is 762.867 Window 28 Bed 9-12 Fracture density is 507.679
6246-6247		<ul style="list-style-type: none"> • Bed dips 45 degrees • 11 beds at 6246 ft with vertical opened fracture characterized, and separated into three windows with 1-8, 9-12, 13-18 layers • Ductile layers are equally thick than brittle layers 	Window 26 Bed 7-11 Fracture density is 702.554
6247-6247.5		<ul style="list-style-type: none"> • Bed dips 45 degrees • 11 beds at 6247 ft with conjugate opened fracture characterized, and separated into two windows with base 5 layers and top 6 layers • Ductile layers are equally thick than brittle layers 	Window 25 Bed 1-6 Fracture density is 787.21


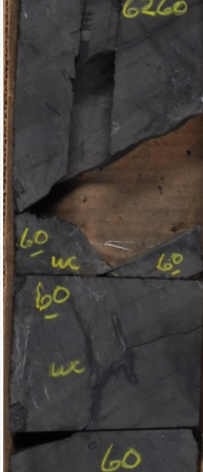

Core Depth	Core photo	Core/ Fracture description/ Detailed Characterization	Fracture density (#/ft ²)
6247.5-6248		<ul style="list-style-type: none"> • Bed dips 50 degrees • Ductile layers are thinner than brittle layers • Vertical Fractures are less observable in this section 	
6248-6249			Window 24 Bed 1-4 Fracture density is 490.684
6249-6249.4		<ul style="list-style-type: none"> • Bed dips 45 degrees • 9 beds with conjugate opened fracture characterized, and separated into two windows with base 4 layers and top 4 layers • Ductile layers are equally thick than brittle layers • A close up look of tensile fracture shows the conjugate form of fracture plane at 6249 ft. 	Window 23 Bed 1-4 Fracture density is 621.087

Core Depth	Core photo	Core/ Fracture description/ Detailed Characterization	Fracture density (#/ft ²)
6249.6-6250		<ul style="list-style-type: none"> • Bed dips 45 degrees • Ductile layers are thinner than brittle layers • Fractures are less developed in 6250 ft section 	
6250-6251		<ul style="list-style-type: none"> • Missing core section 	
6251-6252		<ul style="list-style-type: none"> • Bed dips 45 degrees • 5 beds with vertical opened fracture • Ductile layers are equally thick than brittle layers 	<p>Window 22 Bed 1-5 Fracture density is 853.69</p>
6252-6252.1			




Core Depth	Core photo	Core/ Fracture description/ Detailed Characterization	Fracture density (#/ft ²)
6252.2-6253		  <ul style="list-style-type: none"> • Bed dips 45 degrees • 17 beds with conjugate opened fracture was subdivided into 3 sub windows • First window is 1-7 layer with vertical opened fractures • Second window is 8-11 layers there is a flattened concretions above layer 11 • Third window is 12-17 layers • Ductile layers are thinner than brittle layers 	<p>Window 19 Bed 1-7 Fracture density is 809.626</p> <p>Window 20 Bed 8-11 Fracture density is 382.510</p> <p>Window 21 Bed 12-17 Fracture density is 663.086</p>
6253-6254		 <ul style="list-style-type: none"> • Bed dips 45 degrees • 6 beds with conjugate opened fracture characterized • Ductile layers are thinner than brittle layers 	
6254-6254.8			<p>Window 18 Bed 1-6 Fracture density is 809.297</p>




Core Depth	Core photo	Core/ Fracture description/ Detailed Characterization	Fracture density (#/ft ²)
6254.9-6255		<ul style="list-style-type: none"> Core piece are heavily deformed with no available fracture to characterize 	
6255-6256		<ul style="list-style-type: none"> Bed dips 44 degrees 9 beds with opened conjugate fracture characterized, Ductile layers are almost equal thickness than brittle layers 	<p>Window 17 Bed 1-9 Fracture density is 572.258</p>
6256-6257		<ul style="list-style-type: none"> Bed dips 40 degrees 10 beds with subvertical fracture characterized, and separated into two window with base 5 layers and top 5 layers Part of the core is missing at 6256.2 ft Ductile layers are thinner than brittle layers 	<p>Window 15 Bed 1-5 Fracture density is 775.909</p> <p>Window 16 Bed 6-10 Fracture density is 775.152</p>




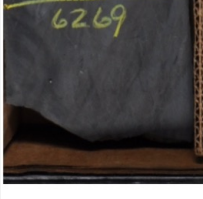
Core Depth	Core photo	Core/ Fracture description/ Detailed Characterization	Fracture density (#/ft ²)
6257-6258		<ul style="list-style-type: none"> • Sharp change in dipping direction with 90 degrees at 6257.5, interpreted as a lateral placed mini fold axis • Missing core at fold axis 	
6258-6259		<ul style="list-style-type: none"> • Bed dips 45 degrees • 9 beds with subvertical fracture characterized, and separated into two windows with base 3 layers and top 6 layers • Part of the core is missing at 6258.3 ft • Some of the beds such as bed 5 have opened fractures 	<p>Window 13 Bed 1-3 Fracture density is 392.032</p> <p>Window 14 Bed 4-9 Fracture density is 655.968</p>
6259-6259.5			




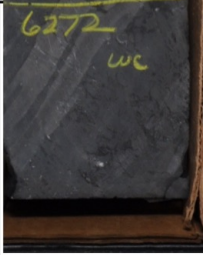
Core Depth	Core photo	Core/ Fracture description/ Detailed Characterization	Fracture density (#/ft ²)
6259.5-6260		<ul style="list-style-type: none"> • Small nodulus found at 6259.5 	
6260-6261		<ul style="list-style-type: none"> • Bed dips 45 degrees • Only one thick bed with intense open fracture characterized, at 6261 	Window 12 Bed 1 Fracture density is 389.833
6261-6262		<ul style="list-style-type: none"> • There is one vein filled fracture with bigger aperture on the left side of the core • Bed dips 45 degrees • 2 bed with subvertical mineral filled fractures are characterized at 6261.8-6262 ft • Fracture density is super saturated and shown as clusters 	Window 11: Bed 1-2 Fracture density is 343.168

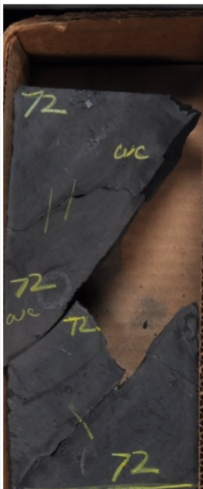





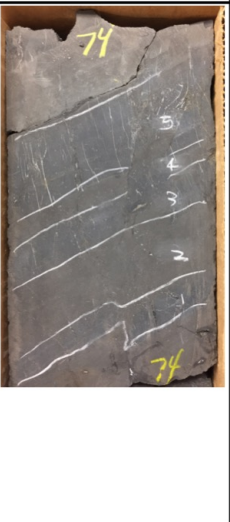

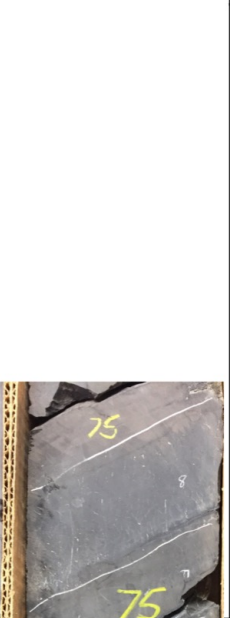


Core Depth	Core photo	Core/ Fracture description/ Detailed Characterization	Fracture density (#/ft ²)
6262-6263		<ul style="list-style-type: none"> • Bed dips 40 degrees • 10 beds with fractures characterized from 6262.5-6263 and 4 beds at 6262-6262.5 Fractures are barely mineral filled and start to show dilate form • Ductile beds are thinner than brittle fracture beds 	<p>Window 9: Bed 1-10 Fracture density is 737.56</p> <p>Window 10: Bed 1-4 Fracture density is 1575.604</p>
6263-6264		<ul style="list-style-type: none"> • Bed dips 40-45 degrees • Light color flattened concretion found at 6263.8 • Fractures are mainly Mineral filled in conjugate forms relative to the beds • 6263.5-6263.7 is partially not available for measurement 	
6264-6264.5			




Core Depth	Core photo	Core/ Fracture description/ Detailed Characterization	Fracture density (#/ft ²)
6264-6265		<ul style="list-style-type: none"> • Missing core at 6264-6264.9 • Brittle and ductile couplets are not obvious 	
6265-6266		<ul style="list-style-type: none"> • Missing core at 6265.5 • Beds are highly curved 	
6266-6266.5			

Core Depth	Core photo	Core/ Fracture description/ Detailed Characterization	Fracture density (#/ft ²)
6266.5-6267		<ul style="list-style-type: none"> • Beds curved indicates intense folding 	
626706268		<ul style="list-style-type: none"> • Sharp change in dipping direction with 90 degrees at 6267, interpreted as a lateral placed mini fold axis • Fractures are partially opened (dilated) • Fractures are compressed • Missing core at 6267.2 	
6268-6269		<ul style="list-style-type: none"> • Beds curved indicates intense folding • Beds dipping 70 degrees with open fracture observed, bed is not easy to trace due to intense deformation 	
6269-6269.2			

Core Depth	Core photo	Core/ Fracture description/ Detailed Characterization	Fracture density (#/ft ²)
6269.5-6270		<ul style="list-style-type: none"> • Beds curved indicates intense folding • Sharp change in dipping direction with 90 degrees at 6270, interpreted as a lateral placed mini fold axis • Fractures are partially opened (dilated) 	
6270--6271		<ul style="list-style-type: none"> • Sharp change in dipping direction with 90 degrees at 6270.9, interpreted as a lateral placed mini fold axis • Fractures are partially opened (dilated) 	
6271-6272		<ul style="list-style-type: none"> • Bed dips 50 degrees • Flattened light gray nodulus at 6272 ft • Fracture sets are not complete • Fractures are mineral filled, cutting through the nodulus 	
6272-6272.3			

Core Depth	Core photo	Core/ Fracture description/ Detailed Characterization	Fracture density (#/ft ²)
6272.4-6273		<ul style="list-style-type: none"> Obvious interbed observed, fracture not available for measurement 	
6273-6274		<ul style="list-style-type: none"> Bed dips 45 degrees Minor normal fault observed at 6273.2 5 beds with fractures outlined and characterized Fractures are mainly non-filled in conjugate forms relative to the beds 6273.5-6274 is partially not available for measurement 	<p>Window 8: Bed 1-5 Fracture density is 339.213</p>
6274-6274.5		<ul style="list-style-type: none"> Bed dips 50 degrees Light color flattened nodulus bed is shown in 6274 ft Minor fracture observed not measured 	

Core Depth	Core photo	Core/ Fracture description/ Detailed Characterization		Fracture density (#/ft ²)
6274.5-6275		<ul style="list-style-type: none"> • Bed dips 35 degrees • 5 beds with fractures outlined and characterized • Main Fracture zone is in layer 5 high density vertical to subvertical form • Fractures are partially mineral filled • Ductile layers are thinner than brittle layers 		Window 7: Bed 1-5 Fracture density is 309.183
6275-6276		<ul style="list-style-type: none"> • No clear fracture sets available for characterization • 3 beds with fractures outlined and characterized • Main Fracture zone is in layer 6 and 8 with high density conjugate set • Fractures are partially mineral filled 		Window 6: Bed 6-8 Fracture density is 609.333
6276-6276.5		<ul style="list-style-type: none"> • Bed dips 30 degrees • 6 beds with fractures outlined and characterized • Main Fracture zone is in layer 3 and 6 with high density conjugate set • Fractures are partially mineral filled • Vertical fractures straight • Ductile layers are thinner than brittle layers 		Window 5: Bed 1-5 Fracture density is 486.698

Core Depth	Core photo	Core/ Fracture description/ Detailed Characterization	Fracture density (#/ft ²)
6276.5-6277		<p>Not available for fracture measurement</p>	<p>Window 3: Bed 14-20 Fracture density is 583.418</p>
6277-6278		<ul style="list-style-type: none"> • Bed dips 45 degrees • Brittle bed and ductile bed are generally even in thickness • 12 beds with fractures outlined and characterized • Fractures are partially mineral filled in vertical-subvertical and conjugate forms relative to the beds • Vertical fractures are straight in thin bed but compressed in thicker beds 	<p>Window 4: Bed 21-26 Fracture density is 282.720</p>
6278-6279		<ul style="list-style-type: none"> • Bed dips 45 degrees • Minor normal fault observed at 6278.3 ft • 11 beds with fractures outlined and characterized • Fractures are mainly mineral filled in vertical-subvertical forms relative to the beds • Vertical fractures are compressed 	<p>Window 1: Bed 1-6 Fracture density is 698.248</p> <p>Window 2: Bed 7-13 (Missing in this foot): Fracture density is 749.892</p>